Inference of Constitutive Relations and Uncertainty Quantification in Electrochemistry

INFERENCE OF CONSTITUTIVE RELATIONS AND UNCERTAINTY QUANTIFICATION IN ELECTROCHEMISTRY

BY

ATHINTHRA KRISHNASWAMY SETHURAJAN, M.Sc.

A THESIS
SUBMITTED TO THE SCHOOL OF COMPUTATIONAL SCIENCE & ENGINEERING
AND THE SCHOOL OF GRADUATE STUDIES
OF McMASTER UNIVERSITY
IN PARTIAL FULFILMENT OF THE REQUIREMENTS
FOR THE DEGREE OF
DOCTOR OF PHILOSOPHY

Doctor of Philosophy (2018) McMaster University
(Computational Science & Engineering) Hamilton, Ontario, Canada

TITLE:	Inference of Constitutive Relations and Uncertainty Quantification in Electrochemistry
AUTHOR:	Athinthra Krishnaswamy Sethurajan M.Sc., (CSE) McMaster University, Hamilton Canada
SUPERVISOR:	Dr. Bartosz Protas
NUMBER OF PAGES:	xxi, 137

Abstract

This study has two parts. In the first part we develop a computational approach to the solution of an inverse modelling problem concerning the material properties of electrolytes used in Lithium-ion batteries. The dependence of the diffusion coefficient and the transference number on the concentration of Lithium ions is reconstructed based on the concentration data obtained from an in-situ NMR imaging experiment. This experiment is modelled by a system of 1D time-dependent Partial Differential Equations (PDE) describing the evolution of the concentration of Lithium ions with prescribed initial concentration and fluxes at the boundary. The material properties that appear in this model are reconstructed by solving a variational optimization problem in which the least-square error between the experimental and simulated concentration values is minimized. The uncertainty of the reconstruction is characterized by assuming that the material properties are random variables and their probability distribution estimated using a novel combination of Monte-Carlo approach and Bayesian statistics. In the second part of this study, we carefully analyze a number of secondary effects such as ion pairing and dendrite growth that may influence the estimation of the material properties and develop mathematical models to include these effects. We then use reconstructions of material properties based on inverse modelling along with their uncertainty estimates as a framework to validate or invalidate the models. The significance of certain secondary effects is assessed based on the influence they have on the reconstructed material properties.

Acknowledgements

I owe my very sincere thanks to my supervisor Dr. Bartosz Protas for his patience and support. His encouragement and close guidance helped me tremendously in my research work and completion of this thesis.

I would like to acknowledge and thank My Ph.D. committee members Dr. Ben Bolker and Dr. Li Xi who have been very encouraging throughout my studies. Their useful insights have tremendously helped me in shaping my research work. I would also like to thank Dr. Sergey Krachkovskiy and Dr. Gillian Goward for providing the experimental data necessary for this research work. Countless discussions with them have given me a great insight about various aspects of this research and helped me in understanding the experimental setup and the electrochemical processes.

It was an absolute delight to work closely with Dr. Jamie Foster, Dr. Giles Richardson, Dr. Ion Halalay and David Bazak in a research team. They have been very courteous and encouraging during our discussions. They were also instrumental for the success of this work.

I would also like to thank all staff, faculty members and students of the School of Computational Science and Engineering and the Department of Mathematics for their warm support and making my stay pleasant.

I am thankful to Dr. Steen Schougaard, Dr. Andy Sun, Dr. Janine Mauzeroll, Dr. Gianluigi Botton and all other members of APC-LIB group for sharing their knowledge in the field of electrochemistry. I would also like to acknowledge the funding provided by Natural Sciences and Engineering Research Council of Canada in various streams such as Automotive Partnership of Canada, Auto-21 and Strategic Partnership Grant (STPGP 479258-15). I would also like to thank General Motors Canada for their funding and support.

Finally, many thanks to my family and friends for their love and I am very fortunate that they have always been there when I needed their support.

Symbols

D^+	Diffusion coefficient of positive ions
D^-	Diffusion coefficient of negative ions
t^+	Transference number of positive ions
$[c_\alpha, c_\beta]$	Identifiability interval
$\mathcal{F}_+$	Flux of positive ions
$\mathcal{F}_-$	Flux of negative ions
κ_+	Mobility of positive ions
κ_-	Mobility of negative ions
$\mathbb{R}^n$	n-dimensional real space
$\mathcal{J}$	Cost functional
$\mathcal{U}$	Functional space with Hilbert structure
ϕ	Electric potential
$\tilde{c}$	In-situ experimental concentration

ξ	Step length in gradient direction
c^{**}	Solution of adjoint system obtained by perturbing t^{+}
c_{+}	Concentration of positive ions
c_{-}	Concentration of negative ions
D	Diffusion coefficient
k_B	Boltzman Constant
$t^{+'}$	Perturbation direction for t^{+}
z_i	Charge carried by species i
c	Salt concentration
j	Molar current density

Contents

4 Uncertainty Quantification 39

5 Ion-Pairing Effects 65

List of Figures

Chapter 1

Introduction

Lithium (Li) ion batteries are a popular electrochemical energy storage device and are used in a wide range of electronic devices around the world. Significant research efforts are being invested into Li-ion batteries right now, because of their potential applications in next-generation automobiles [65] and green technology [20]. A complete understanding of the physics and electrochemistry behind the workings of Li-ion batteries is necessary to further improve their efficiency and performance.

Many researchers across the world have derived mathematical models for Li-ion batteries for analyzing and optimizing their performance. Two main types of models that are widely used are equivalent circuit models [15] and physics-based models [88]. Equivalent circuit model is a mathematical model based on a theoretical circuit that retains average electrical characteristics of the battery [44]. Such models are used to describe both electrical and mass transport phenomena in the battery [75]. On the other hand, the underlying physics is captured to describe the working of battery in the physics-based model [56]. Both types of models have their own advantages and disadvantages, but to understand the complex behavior of the batteries at various

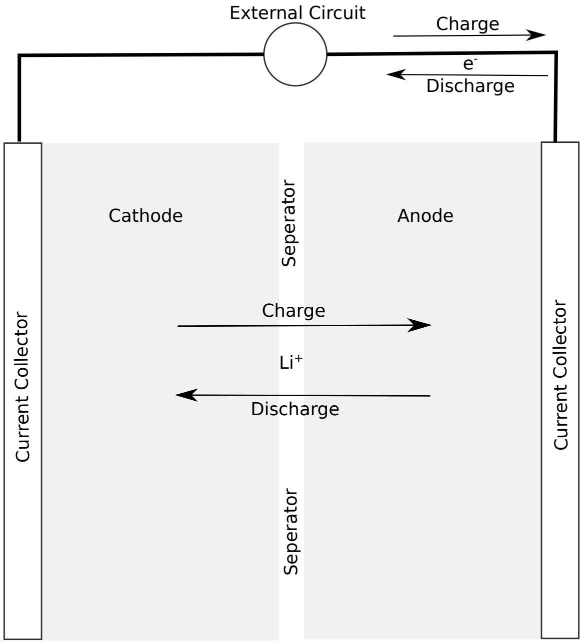

Figure 1.1: Functional overview of a Li-ion battery.

scales [94], physics-based models are preferred.

In physics-based models, different physical processes are modeled separately and put together as a closed system of governing equations in which individual components are allowed to interact with each other. A typical Li-ion battery is made up of solid and liquid components. The solid components are the anode and the cathode which store Lithium atoms and also help conduct negatively charged electrons to the external circuit as shown in Fig. 1.1. The cathode of a Li-ion battery is typically a Lithium-rich substrate such as Lithium-Nickel-Manganese-Cobalt Oxide (NMC) or Lithium-Manganese Oxide (LMO). On the other hand, the anode of Li-ion battery is often made from materials such as graphite or silicon which can absorb Lithium through the intercalation process to store electrochemical energy [6]. The Li-ion battery is charged by transporting Li-ions from the cathode and intercalating them onto the anode and thus increasing the free energy of the system. This system then provides electric energy by spontaneously discharging in a closed circuit. The liquid component of the battery is an electrolyte that is made up of a Lithium based salt and a suitable solvent. This is a crucial component which helps in moving positively charged Li ions across the electrodes to complete the circuit (cf. Fig. 1.1). The interaction of solid and liquid components takes place at the solid-liquid interface inside the battery [58]. The transport of Lithium as atoms in the electrode and as ions in the electrolyte is assumed to be a diffusion-based process in most physics-based models [5, 23, 38, 56]. The transport of Lithium ions in the electrolyte is of particular interest in this study because those transport properties determine the efficiency and performance of the battery [63]. Lithium is transported as positively charged ions. They are driven by the existing electric potential inside the battery. Lithium transport in the electrolyte can be modeled based on the Planck-Nernst equation. Flux of species i in the electrolyte can be described based on Planck-Nernst model as [56]

$$\mathcal{F}_i = -D_i \nabla c_i - \frac{D_i z_i}{k_B T} c(\nabla \phi). \tag{1.1}$$

This model works well in dilute conditions or the Planck-Nernst equation with concentration-dependent material properties which works well for the concentrated electrolytes [23]. The main material properties that are involved in both types of transport models of Li ions are the electrical conductivity, the diffusion coefficient and the transference number. Knowledge of these properties for different electrolytes not only helps us to use them in transport models but also tells us about the intrinsic nature of the material under consideration. Estimation of the diffusion coefficient and transference number is the primary focus of this research.

The diffusion coefficient is typically measured as a constant property using Stokes-Einstein's relation [28], NMR spectroscopy [66], and by inverse calculations using potentiostatic and galvanostatic measurements [96]. The transference number of Lithium ion, which is defined as the fraction of the applied current carried by the Lithium ion in the electrolyte, is another important material property. It is usually approximated as the ratio of diffusion coefficients of two ions as shown below [31]:

$$t^{+} = \frac{D^{+}}{D^{+} + D^{-}}. \tag{1.2}$$

Inverse calculations using galvanostatic and potentiostatic experiments are also used to estimate the transference number in electrolytic solutions [34]. In all the above mentioned methods, the diffusion coefficient and the transference number are measured as constant properties or measured at selected points of salt concentration [41, 92]. However, modeling studies also provide evidence that models with concentration-dependent material properties more accurately predict the behavior of battery systems [42]. Motivated by these results, this study attempts to develop and validate a framework that estimates the concentration-dependent diffusion coefficient and transference number of the electrolyte by solving an inverse problem using experimental data.

Inverse modelling is a framework that combines measurement data and mathematical models into information about the properties of the system. For example, a galvanostatic experiment measures the variation in potential with time for a constant current applied through the electrolyte. With this measurement and a suitable transport model, an inverse calculation can estimate the material properties of the electrolyte such as diffusion coefficient, transference number and conductivity. Inverse problems are also an area of study that receives significant attention in many research fields such as medicine [46], earth sciences [27], image processing [9], astronomical sciences [54], etc.. Specifically, inverse problems in which one estimates material properties as a function of space are well researched and understood. They serve as an important tool in modern non-invasive imaging techniques [22] and in medical and geological applications. In most of these applications, an inverse problem is posed as an optimization problem constrained by partial differential equations (PDEs). The use of adjoint analysis [67] to solve PDE-constrained optimization problems for finding control parameters dependent on space and time is also well understood and effectively used in advanced optimization algorithms.

Inverse problems also find their application in estimating material properties of Li-ion battery electrolytes. The seminal study by M. Klett et al. [38] used concentration data collected using NMR imaging technique to estimate the diffusion coefficient and transference number as constant properties. That study used the COMSOL software package to solve the PDE models and MATLAB to solve the optimization problem. The main novelty of our research is that we develop and validate a method to estimate material properties such as the diffusion coefficient (D) and transference number (t^+) as a function of concentration using data from similar experiments to those outlined by M. Klett et al. [38].

Solving an inverse problem to estimate the state-dependent material properties has been documented for a purely diffusive model by V. Bukshtynov et al. [14]. In that study, a solution to the inverse problem is obtained by solving an optimization problem using adjoint analysis and the diffusion coefficient is estimated for manufactured data. That work also addresses the various computational challenges related to the accurate and efficient evaluation of cost functional gradients for optimization. Taking it as a point of departure for the computational setup, the current study was carried out to estimate two material properties, the diffusion coefficient and the transference number, that appear in the model for the Lithium transport in the electrolyte, as a function of concentration. Although the reference study [14] uses a model simpler than the ones used here, the general guidelines that it provides are very relevant for our present research.

Inverse problems by their nature are ill-posed and the solution of an inverse problem is typically uncertain [7]. The presence of noise in the measurements may significantly affect the reconstructed solution. Uncertainty in the problem can arise from noise in the experimental data, systematic error in the experiment, and inaccuracy of the model. Thus, uncertainty estimation is crucial to assess the quality of the inverse modelling estimates. It can be carried out using deterministic approaches such as stationary distribution models [4] or by sampling approaches such as Monte-Carlo analysis [53]. This issue of uncertainty quantification was partially resolved in our previous research by using a Monte-Carlo approach [79]. The problem with the stationary distribution models and Monte-Carlo approach is that they only considers uncertainty that arises due to noise in the data, while other sources are ignored. Bayesian methods have been proposed to solve inverse problems for a number of applications in image processing [82], impedance tomography [60], etc.. In a Bayesian approach, the material properties are considered random variables and their randomness (standard deviation) depends on the quality of the experimental data and the mathematical model [87]. Because of this important property of the Bayesian approach, it is used in the present research to estimate uncertainty in the reconstructions of both constant and concentration-dependent diffusion coefficient and transference number.

Inverse modelling and uncertainty quantification with experimental data and the Planck-Nernst model can sometime fail to provide valid results consistent with the fundamental principles of thermodynamics [21]. In our research, we encountered this problem when the inverse modelling framework estimated negative values of the transference number. As we use a binary electrolyte, negative transference number is impossible under the laws of thermodynamics [52], and therefore this signals the loss of validity of the simple Plank-Nernst model. There are a number of possible additional effects present in the system which may cause such nonphysical results. Thus, an important property of inverse modelling with uncertainty quantification is that it can provide insights about the accuracy of the model. We can utilize this property to justify or invalidate the incorporation of certain physical effects in the model.

The highlights of this research are the following:

- An inverse modelling framework to estimate both constant and concentration-dependent material properties in the electrochemical system is developed and validated [79]. This is a refinement of the approach from my Masters thesis [76].
- An uncertainty quantification method for inverse modelling based on Bayesian statistics is developed and validated [78].
- The framework consisting of these two constituents is then used to:
  - demonstrate the loss of validity of Planck-Nernst model at higher salt concentrations,

- show that accounting for ion-pairing effects occurring at such conditions does not resolve the problem with the validity of the model [69] and
- demonstrate that the presence of dendrite growth in the electrolyte must be accounted for in the model in order to obtain physically consistent predictions [77].

The plan of this thesis is as follows: the electrochemical theory and the mathematical model to describe the transport of Lithium in a battery are discussed in Chapter 2; then the problem of estimating material properties is defined and the methodology is outlined in Chapter 3; then in Chapter 4, the tools for uncertainty quantification are introduced and validated; in Chapter 5 and 6 inverse modelling is used to validate the models for ion transport in the presence of ion-pairing effects and in the presence of dendritic growth, respectively. We outline important conclusions from this study in chapter 7.

Chapter 2

Material Transport in Electrochemical Systems

2.1 Experimental Setup

The aim of the experiment is to capture the profile of the salt concentration of the electrolyte in a simplified working model of a battery. Li-ion battery electrolyte is typically made by dissolving a Lithium-based salt in an organic solvent resulting in the dissociation of salt into positive ions (typically Li^+) and negative ions. If a differential electric potential is applied to this electrolyte, these ions migrate causing an electric current. This ion migration is characterized by material properties associated with the electrolyte. As our goal is to infer the material properties from their transport, a simple experiment was set up by our collaborator Dr. Sergey Krachkovisky under the supervision of Dr. Gillian Goward from the Department of Chemistry at McMaster University. With his expertise in Nuclear Magnetic Resonance (NMR) imaging [41], our collaborator designed and developed the experimental techniques described in

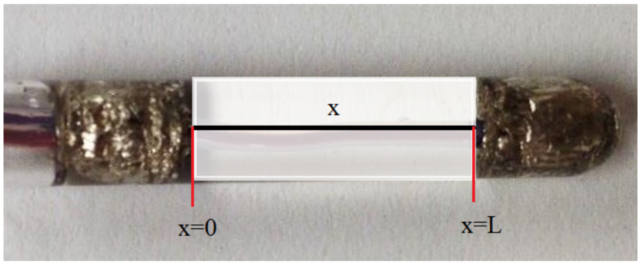

Figure 2.1: NMR tube cell with Lithium electrodes.

this section. In our research, we use data from two different experimental setups involving two different types of electrolytes and different experimental conditions.

2.1.1 Experiment I

The experimental setup shown in Fig. 2.1 is a simplified setup of a Li-ion battery in which the space between the electrodes is increased to facilitate the experiment to capture concentration profiles. Lab-manufactured electrolyte used in this setup is Lithium bis(trifluoro-methanesulfonyl)imide (LiTFSI) dissolved in propylene carbonate. The setup consists of a cylindrical cell with a length 20 mm. The cell is filled with electrolyte of 1000 mol/m^3 salt concentration and sealed with metallic Lithium electrodes. An In-Situ NMR (Nuclear Magnetic Resonance) imaging technique [66] was used to estimate the concentration of ions present in the electrolyte when the current was passed through the cell. This experiment is hereafter referred to as an "in-situ experiment". In this experiment, an NMR probe was allowed to scan through the region of the cell filled with electrolyte and measure the intensity of electromagnetic radiation emitted by Fluorine atoms present in the TFSI$^-$ ion due to the presence of a magnetic field. As it is assumed that the concentration of ions is directly proportional to the intensity of electromagnetic wave emitted by them, the intensity measurement is an indirect measure of the concentration of $TFSI^-$ ions present in the electrolyte. As the NMR probe scans through the length of the cell, it measures the intensity of the emitted electromagnetic wave across the cell and thus gives us the intensity profile of the entire cell as output.

Reference data were collected at the beginning of the experiment when no current was flowing, as the concentration of the salt in the electrolyte was homogeneous throughout the cell. Then, a constant current of 50μA was allowed to flow through the cell and the intensity profile was collected at equal time intervals. The intensity measurements obtained by our collaborators are shown in Fig. 2.2.

The measurement denoted '0 hours' in Fig.2.2 will serve as the reference corresponding to the homogeneous 1000 mol/m^3 concentration. With this measurement and the assumption that the intensity is proportional to the concentration [41], the concentration profiles at all subsequent time levels can be obtained. Fig. 2.3 shows the corresponding concentration profiles obtained from electromagnetic wave intensity measurements at various time points. In this figure, we can see that the concentration values become polarized as time progresses, which is what we would expect to happen when negative ions move towards the positively charged electrode.

2.1.2 Experiment II

The second experiment is very similar to the one described in section 2.1.1, except that a higher current is passed through a commercial electrolyte to probe a larger range of salt concentrations. The study is carried out under galvanostatic conditions in a symmetric Li-Li electrochemical cell constructed from a 5 mm diameter NMR tube, shown in Fig. 2.4, filled with a 1M $LiPF_6$ solution in a binary mixture of

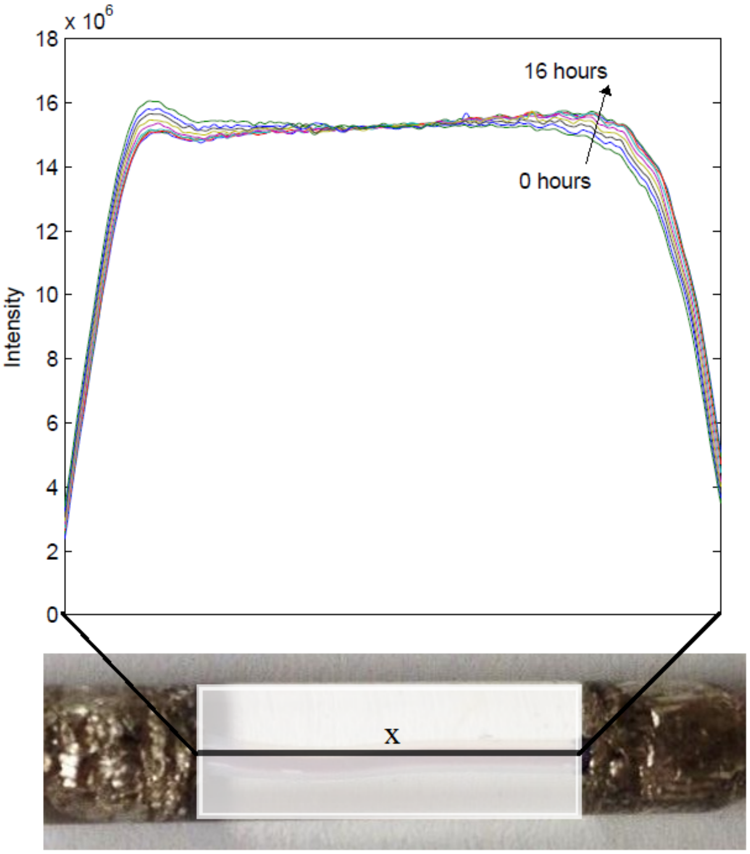

Figure 2.2: Experiment I: Intensity distribution across the cell with different color denoting measurement acquired at different time levels

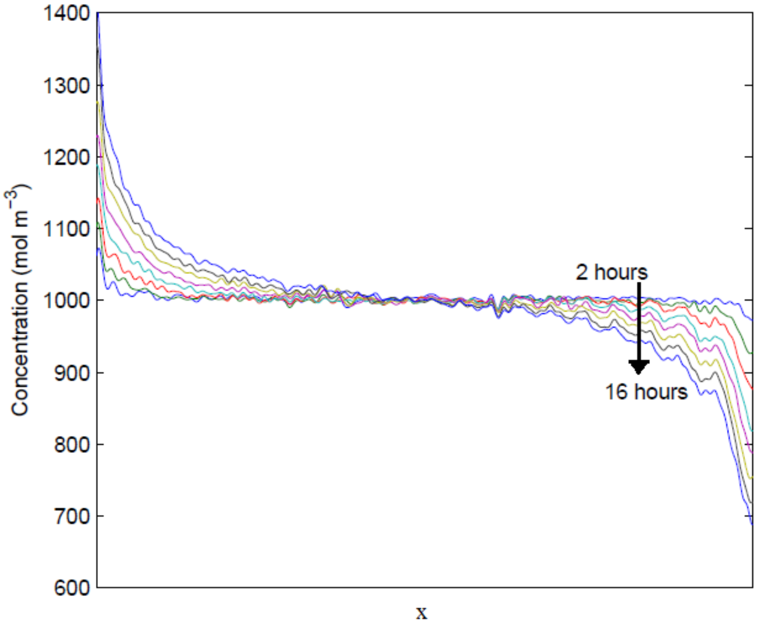

Figure 2.3: Experiment I: Concentration profiles across the cell corresponding to the intensity profiles shown in Fig. 2.2 with different colors denoting measurement acquired at different time levels

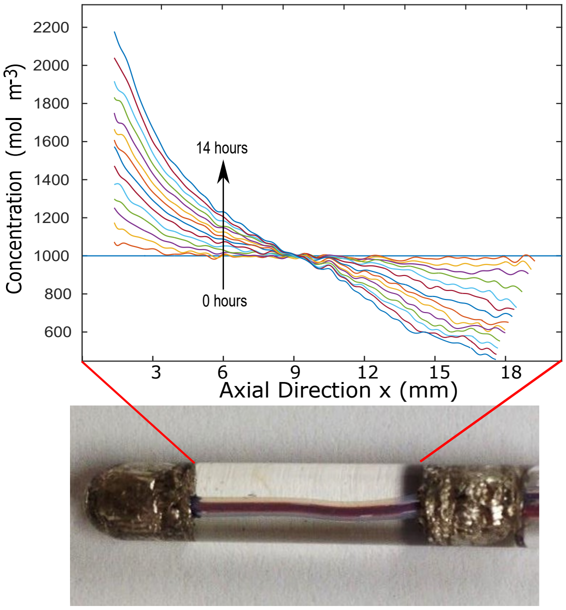

Figure 2.4: Experiment II: Concentration profiles obtained via in-situ magnetic resonance imaging during a galvanostatic polarization experiment.

ethylene carbonate (EC) and dimethyl carbonate (DMC) with 1:1 volume ratios. A constant current of 75 μA (corresponding to the current density of 382 μA cm^{-2}) was applied to the cell for 16 hours. Concentration profiles were acquired using magnetic resonance imaging (MRI). For this experiment, we chose to monitor the ^{19}F nuclei, which significantly reduces the data acquisition time, since the relative NMR sensitivity to a ^{19}F nucleus is approximately 3 times higher than to a ^{7}Li nucleus. One-dimensional ^{19}F NMR images were obtained using a gradient spin-echo pulse sequence with the magnetic field gradient applied along the x-direction (i.e., along the axis of the cell), with a 3 ms echo time and a 20 G/cm reading gradient[17]. In the course of experiment 256 frequency-domain points were collected over the spectral width of 200 kHz. The combination of the magnetic field gradient and spectral resolution yielded a spatial resolution of 40 μm. A total of 64 scans with a relaxation delay

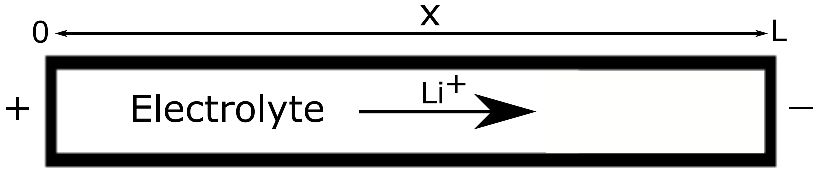

Figure 2.5: Schematic figure illustrating the domain in which Planck-Nernst model is defined.

of 3.5 s were collected for each image, resulting in an acquisition time of 4 minutes per image. The imaging measurement sequence was repeated at 2-hour intervals uniformly spread over the 16 hours duration of the galvanostatic experiment. The experimentally obtained concentration profiles, hereafter denoted $\tilde{c}(x,t)$, are shown in Fig. 2.4 at different times $t \in [0, 14 \text{ hours}]$ as functions of the space coordinate x.

2.2 Planck-Nernst Model

In this section, we formulate the Planck-Nernst model. We make the following modelling assumptions based on the experimental setup described in the previous section in order to obtain the mathematical description of mass transport during the galvanostatic experiment [79]:

A1: isothermal conditions;

A2: the lack of thermodynamic ideality (i.e., activity coefficient different from one) and the effect of the solution viscosity accounted for by an a priori undetermined dependence of the material properties on the salt concentration;

A3: ion transport occurs only in the axial direction x and transport in the radial direction of the cell is negligible;

A4: the electrolyte solution is homogeneous at the beginning of the experiment;

A5: the system satisfies local electrical neutrality at every location in the bulk, which implies that $c_+ = c_- = c$, where c_+ is concentration of positive ions, c_- is concentration of negative ions and c is the salt concentration;

A6: mass transport occurs only by diffusion and migration in the applied electric field (i.e., convective transport is neglected);

A7: the cation flux at the two boundaries ($x = 0$ and $x = L$) corresponds to the applied electric current and results in lithium deposition and stripping, respectively [59, 55].

We begin by postulating the following constitutive equations for the fluxes of positive ions $\mathcal{F}_+$ and negative ions $\mathcal{F}_-$ in the spatial domain shown in Fig. 2.5:

$$\mathcal{F}_+ = -D_+ \frac{\partial c_+}{\partial x} - \kappa_+ c_+ \frac{\partial \phi}{\partial x}, \tag{2.1a}$$

$$\mathcal{F}_- = -D_- \frac{\partial c_-}{\partial x} + \kappa_- c_- \frac{\partial \phi}{\partial x}, \tag{2.1b}$$

where κ_+ is the mobility of positive ion, κ_- is the mobility of negative ion and ϕ is electric potential. Based on the electrical neutrality condition A5, one can write the charge conservation equation as

$$\frac{\partial \left(\mathcal{F}_+ - \mathcal{F}_-\right)}{\partial x} = 0. \tag{2.2}$$

The molar mass conservation equations for each of the two species in the system then can be written as

$$\frac{\partial c_+}{\partial t} + \frac{\partial \mathcal{F}_+}{\partial x} = 0, \tag{2.3a}$$

$$\frac{\partial c_-}{\partial t} + \frac{\partial \mathcal{F}_-}{\partial x} = 0. \tag{2.3b}$$

The above equations (2.2) and (2.3) can be supplemented with the suitable boundary condition at electrode-electrolyte interface. In electrochemical cells with lithium metal electrodes, lithium ions are stripped from one electrode and deposited onto the other. At the same time, anions cannot originate from a Li electrode or deposit onto one. Therefore the appropriate boundary conditions for the ionic fluxes are

$$\mathcal{F}_+|_{x=0,L} = j, \tag{2.4a}$$

$$\mathcal{F}_-|_{x=0,L} = 0. \tag{2.4b}$$

The above governing equations, (2.3a)–(2.3b), together with the equation for charge conservation (2.2), prescribed flux equation at the boundary (2.4), suitable boundary conditions for the potential and initial conditions for the charged species and the potential comprise a closed system of equations that could in principle be solved, to determine the evolution of the species' concentrations of $c_+(x,t)$ and $c_-(x,t)$. However, in the following subsection we reformulate the system to eliminate the potential and thus avoid solving the elliptic Poisson equation.

2.2.1 Reformulation of the Transport Model

The equation for the molar current density j is given in terms of the fluxes of the different charged species by

$$j = \mathcal{F}_+ - \mathcal{F}_-, \tag{2.5}$$

where j can be calculated from applied current I using the following expression.

$$j = \frac{I}{FA}, \tag{2.6}$$

where F is Faraday's constant and A is the cross sectional area of the cell. Because of the galvanostatic nature of the experiment the applied current I is constant. On using (2.1a)–(2.1b) and the electroneutrality condition $c_+ = c_- = c$, the following expression is derived for the gradient in the electric potential:

$$\frac{\partial \phi}{\partial x} = -\frac{(D_+ - D_-)}{(\kappa_+ + \kappa_-)\, c}\frac{\partial c}{\partial x} - \frac{j}{(\kappa_+ + \kappa_-)\, c}. \tag{2.7}$$

Taking the sum of equations (2.3a) and (2.3b), and once again using the electroneutrality condition leads to

$$\frac{\partial c}{\partial t} + \frac{\partial}{\partial x}\left(\frac{\mathcal{F}_+ + \mathcal{F}_-}{2}\right) = 0. \tag{2.8a}$$

On substituting the respective flux equations, (2.1a) and (2.1b), for $\mathcal{F}_+$ and $\mathcal{F}_-$ and using (2.7) to eliminate $\partial\phi/\partial x$ we obtain the conservation equation for c, namely

$$\frac{\partial c}{\partial t} = \frac{\partial}{\partial x}\left[\left(\frac{D_+ + D_-}{2} + \frac{(D_+ - D_-)(\kappa_- - \kappa_+)}{2(\kappa_+ + \kappa_-)}\right)\frac{\partial c}{\partial x} + \frac{\kappa_- - \kappa_+}{2(\kappa_+ + \kappa_-)} j\right], \tag{2.9}$$

Adding up the boundary conditions (2.4a) and (2.4b), substituting $\mathcal{F}_+$ and $\mathcal{F}_-$ from the respective flux equations, (2.1a) and (2.1b), and then using (2.7) to eliminate $\partial\phi/\partial x$, we arrive at the following conditions for the gradient of c at the domain boundaries

$$\left.\frac{\partial c}{\partial x}\right|_{x=0,L} = -\frac{\frac{\kappa_- - \kappa_+}{\kappa_+ + \kappa_-} j}{\frac{D_+ + D_-}{2} + \frac{(D_+ - D_-)(\kappa_- - \kappa_+)}{2(\kappa_+ + \kappa_-)}}. \tag{2.10}$$

When combined with appropriate initial conditions for the concentrations of positive/negative ions, the two boundary conditions (2.10) are sufficient to close the model equations (2.9).

Finally, to simplify the expression (2.9) and (2.10) we define an effective diffusion coefficient D, and the transference number t^+ by

$$D = \frac{D_+ + D_-}{2} + \frac{(D_+ - D_-)(\kappa_- - \kappa_+)}{2(\kappa_+ + \kappa_-)}, \tag{2.11a}$$

$$t^+ = \frac{\kappa_+}{\kappa_+ + \kappa_-}. \tag{2.11b}$$

By using the above definitions in the governing equations (2.9), and in the boundary conditions (2.10), and by specifying the initial conditions c^{init} we arrive at the following closed system to be solved for c:

$$\frac{\partial c}{\partial t} = \frac{\partial}{\partial x}\left[D\frac{\partial c}{\partial x}\right] - \frac{\partial t^+}{\partial x} j \qquad \text{in } (0,L)\times(0,T], \tag{2.12a}$$

$$\left.\frac{\partial c}{\partial x}\right|_{x=0,L} = -\frac{(1-t^+)j}{D} \qquad \text{in } (0,T], \tag{2.12b}$$

$$c\big|_{t=0} = c^{\text{init}} \qquad \text{in } [0,L], \tag{2.12c}$$

We note that the effective diffusion coefficient D in (2.11a) does not correspond to any particular species in the system but the resulting concentration c does represent the concentration of both positive and negative ions because of the electroneutrality condition ($c = c_+ = c_-$). In the next chapter, we formulate the inverse problem to reconstruct D and t^+ using the model (2.12) and experimental data described in Section 2.1.

Chapter 3

Inverse Problem for Reconstruction of Transport Coefficients

In this chapter, we formulate our inverse modelling technique by posing it as an optimization problem. Then, we develop a gradient-based approach to the solution of this optimization problem in which the gradients of the objective (error) functional are obtained with adjoint analysis. In the later part of this chapter we validate the inverse modelling technique using the method of manufactured solution.

3.1 Reconstruction as an Optimization Problem

A common approach to reconstruct material properties is to use some strategy to minimize the least-square error between the experimental ($\tilde{c}$) and simulated concentration values (c). Thus, an optimization problem is posed where such a least-square error is the cost functional that has to be minimized with respect to the material properties, namely, the diffusion coefficient D and the transference number t^+, as the control parameters:

$$\mathcal{J}(D,t^+) = \frac{1}{2}\int_0^T \int_0^L \big(c(x,t;D,t^+) - \tilde{c}(x,t)\big)^2\, dxdt, \tag{3.1}$$

where the dependence of the concentration c($.$;D,t^+) on the material properties D and t^+ is given by the mathematical model (2.12). Depending on the allowed form of material properties, the optimization problem can be stated in the following two distinct ways:

$$P1: \qquad [\hat{D},\hat{t}^+] = \underset{[t^+,D]\in\mathbb{R}^2}{\operatorname{argmin}}\, \mathcal{J}(D,t^+) \qquad \text{and}$$

$$P2: \qquad [D(c),t^+(c)] = \underset{[t^+(c),D(c)]\in\mathcal{U}}{\operatorname{argmin}}\, \mathcal{J}(D,t^+),$$

The problem posed in P1 is simpler as the solution is obtained as a constant vector in space $\mathbb{R}^2$. This type of inverse problem is rather straight-forward to deal with and the solution methodology involves solving an unconstrained optimization problem in a 2-dimensional vector space [38]. On the other hand, problem P2 is not trivial as we need to identify $D(c)$ and $t^+(c)$ as function of the concentration c. This chapter is devoted to the development of a solution strategy for problem P2.

Problem P2 is an unconstrained optimization problem and hence the first-order optimality condition requires the gradients of cost functional $\mathcal{J}$ with respect to control parameters to vanish. The symbols $\nabla_D \mathcal{J}$ and $\nabla_{t^+} \mathcal{J}$ will denote gradients of the cost functional (3.1) with respect to $D(c)$ and $t^+(c)$, respectively. With the help of these gradients, local minimizers $\widehat{D}(c)$ and $\widehat{t^+}(c)$ can be found using a simple gradient-descent algorithm

$$D^{(n+1)}(c) = D^{(n)}(c) - \xi_D^{(n)} \nabla_D \mathcal{J}\left(D^{(n)}(c), t^{+(n)}(c)\right) \qquad n = 1, 2, \dots, \tag{3.2a}$$

$$t^{+(n+1)}(c) = t^{+(n)}(c) - \xi_{t^+}^{(n)} \nabla_{t^+} \mathcal{J}\left(D^{(n+1)}(c), t^{+(n)}(c)\right) \qquad n = 1, 2, \dots, \tag{3.2b}$$

$$[D^{(\infty)}(c), t^{+(\infty)}(c)] = [\widehat{D}, \widehat{t^+}], \tag{3.2c}$$

where $\xi_D^{(n)}$ and $\xi_{t^+}^{(n)}$ are the lengths of the descent steps at iteration n and $D^{(1)}$ and $t^{+(1)}$ are the initial guesses. We emphasize that, apart from smoothness and the behavior at the endpoints (i.e., for $c \to c_\alpha, c_\beta$), no other a priori assumptions will be made about the functional forms of $D(c)$ and $t^+(c)$. Smoothness and continuity at the endpoints of the material properties $D(c)$ and $t^+(c)$ is ensured by choosing to reconstruct them using the gradient of cost functional defined in a Sobolev space, which is discussed in detail in Chapter 3.2.1.

There are many ways of formulating a gradient-descent algorithm for problem P2 and Eqn. (3.2) is just one possibility. In this approach the values for $D(c)$ and $t^+(c)$ are updated one after the other based on the Gauss-Seidel iteration for solving linear systems.

In our study, the initial guess for the solution of problem P2 via iterations (3.2) is taken as the solution of problem P1, which will help us to avoid sub-optimal local minima, i.e.,

$$[D(c)^{(1)}, t^+(c)^{(1)}] = [\widehat{D}, \widehat{t^+}]. \tag{3.3}$$

3.2 Gradients of Cost Functional

Gradients of the cost functional in an appropriate functional space are the key ingredient for solving problem P2. The gradients of the error functional (3.1) with respect to concentration-dependent properties $D(c)$ and $t^+(c)$ can be calculated starting from the directional derivatives defined as follows (to simplify the notation, we will not indicate the dependence on c in this section, for example $D(c)$ and $t^+(c)$ will be denoted as D and t^+, respectively.)

$$\mathcal{J}'([D, t^+]; D') = \lim_{\epsilon \to 0} \epsilon^{-1} \left[\mathcal{J}([D + \epsilon D', t^+]) - \mathcal{J}([D, t^+]) \right], \tag{3.4a}$$

$$\mathcal{J}'([D, t^+]; t^{+'}) = \lim_{\epsilon \to 0} \epsilon^{-1} \left[\mathcal{J}([D, t^+ + \epsilon t^{+'}]) - \mathcal{J}([D, t^+]) \right], \tag{3.4b}$$

where D' and $t^{+'}$ are the perturbations of the control variables D and t^+, respectively. In order to identify expressions for the gradients of the error functional as elements of a functional (Hilbert) space, we use the Riesz representation theorem [47]

$$\mathcal{J}'([D, t^+]; D') = \left\langle \nabla_D \mathcal{J}, D' \right\rangle_{\mathcal{X}}, \tag{3.5a}$$

$$\mathcal{J}'([D, t^+]; t^{+'}) = \left\langle \nabla_{t^+} \mathcal{J}, t^{+'} \right\rangle_{\mathcal{X}}, \tag{3.5b}$$

where $\langle \cdot, \cdot \rangle_{\mathcal{X}}$ denotes the inner product in the functional space $\mathcal{X}$ (to be specified below). To fix attention, we begin with the directional derivative (3.4a) with respect to the diffusion coefficient D which can be evaluated as follows

$$\mathcal{J}'([D,t^+];D') = \sum_{i=1}^{N_T} \int_0^T \int_0^L \big[c(x,t;[D,t^+]) - \tilde{c}(x,t)\big]\, \delta(t-t_i) c'(x,t;D,D')\, dx\, dt, \tag{3.6}$$

where $\delta(\cdot)$ is the Dirac delta distribution and c' is the solution of the PDE system obtained as a perturbation of the governing system (2.12), see (3.9) below. Now the following transformation is invoked

$$V(x,t) = \int_{c_\alpha}^{c(x,t)} D(s)\, ds, \quad x \in [0,L] \text{ and } t \in [0,T], \tag{3.7}$$

where $c_\alpha = \min_{t\in[0,T],\, x\in[0,L]} c(x,t)$. We will define the identifiability interval $\mathcal{I} = [c_\alpha, c_\beta]$, where $c_\beta = \max_{t\in[0,T],\, x\in[0,L]} c(x,t)$, as the range of concentration values spanned by solutions of (2.12). To simplify the notation, we also denote

$$Q(x,t) = \frac{(1-t^+)I}{FA}. \tag{3.8}$$

Using these definitions, the perturbation system takes the form

$$\begin{aligned} \frac{\partial c'}{\partial t} &= \frac{\partial}{\partial x}\left(\frac{\partial V'}{\partial x} + Q'\right) && \text{in } (0,L)\times(0,T], && (3.9a)\\ \left.\left(\frac{\partial V'}{\partial x} + Q'\right)\right|_{x=0,L} &= 0 && \text{in } [0,T], && (3.9b)\\ c'\big|_{t=0} &= 0 && \text{in } [0,L], && (3.9c) \end{aligned}$$

where the perturbation variables V' and Q' are expressed as

$$V'(x,t) = \int_{c_\alpha}^{c(x,t)} D'(s)ds + D(c)c'(x,t;D'), \tag{3.10}$$

$$Q'(x,t) = -\left[\frac{dt^+}{dc}c'(x,t;D')\right]\frac{I}{FA}. \tag{3.11}$$

We now observe that directional derivative (3.6) is not in a form consistent with Riesz representation (3.5a), because the perturbation variable D' does not appear explicitly in it, but is instead hidden (as V', cf. (3.10)) in the perturbation system (3.9). In order to transform the directional derivative (3.6) into the Riesz form (3.5a) we will employ adjoint analysis.

Multiplying Eqn. (3.9a) by *adjoint* variable c^* and integrating over the time and space domain, we get

$$\int_0^L \int_0^T \frac{\partial c'}{\partial t} c^* \, dt\, dx = \int_0^T \int_0^L \left[\frac{\partial^2 V'}{\partial x^2}c^* + \frac{\partial Q'}{\partial x}c^*\right] dx\, dt. \tag{3.12}$$

By re-organizing Eqn. (3.12) and integrating it by parts with respect to both space and time we obtain

$$\begin{aligned}\int_0^L & \left\{ [c'c^*]_0^T - \int_0^T \frac{\partial c^*}{\partial t}c' dt \right\} dx \\ &= \int_0^T \left\{ \left[\frac{\partial V'}{\partial x}c^*\right]_0^L - \int_0^L \frac{\partial V'}{\partial x}\frac{\partial c^*}{\partial x}dx + [Q'c^*]_0^L - \int_0^L Q'\frac{\partial c^*}{\partial x}dx \right\} dt. \end{aligned} \tag{3.13}$$

Using Eqn. (3.9a)–(3.9c) we can eliminate a number of boundary terms after which we integrate the term with $\frac{\partial V'}{\partial x}$ by parts one more time, so that we arrive at

$$\int_0^L \left\{ [c'c^*]_{t=T} - \int_0^T \frac{\partial c^*}{\partial t} c' dt \right\} dx \\ = \int_0^T \left\{ - \left[\frac{\partial c^*}{\partial x} V' \right]_0^L + \int_0^L V' \frac{\partial^2 c^*}{\partial x^2} dx - \int_0^L Q' \frac{\partial c^*}{\partial x} dx \right\} dt. \tag{3.14}$$

Now we assume that the adjoint system (defined on the same domain as the governing system (2.12)) is in the form

$$-\frac{\partial c^*}{\partial t} = D \frac{\partial^2 c^*}{\partial x^2} + \frac{dt^+}{dc} \frac{I}{FA} \frac{\partial c^*}{\partial x} + \sum_{i=1}^{N_T} (c - \tilde{c})\, \delta(t - t_i), \tag{3.15a}$$

$$\left. \frac{\partial c^*}{\partial x} \right|_{x=0,L} = 0, \tag{3.15b}$$

$$\left. c^* \right|_{t=T} = 0 \tag{3.15c}$$

which reduces identity (3.14) to the following expression for the directional derivative of the error functional (see (3.6))

$$\mathcal{J}'([D, t^+]; D') = \int_0^T \int_0^L \left[\int_{c_\alpha}^{c(x,t)} D'(s) ds \right] \frac{\partial^2 c^*}{\partial x^2} \, dx \, dt. \tag{3.16}$$

We remark that adjoint system (3.15) is in fact a *terminal* value problem, cf. (3.15c), which means that it needs to be integrated backwards in time (however, since the term with the time derivative has a negative sign, the problem is well-posed). Although this is not the function space we will ultimately use in the computations, for now we set $\mathcal{X} = L^2(\mathcal{I})$ meaning that our function space consists of square-integrable functions of the concentration c. The corresponding inner product, needed in (3.5a), is

$$\left\langle \nabla_D^{L^2} \mathcal{J}, D' \right\rangle_{L^2(\mathcal{I})} = \int_{c_\alpha}^{c_\beta} \nabla_D \mathcal{J}(c) D'(c)\, dc. \tag{3.17}$$

Changing the order of integration in (3.16) and employing (3.17) we arrive at the following expression for the L^2 gradient of the error functional

$$\nabla_D^{L^2} \mathcal{J}(s) = \int_0^T \int_0^L \chi_{[c_\alpha, c(x,t)]}(s) \frac{\partial^2 c^*}{\partial x^2}\, dx\, dt, \qquad s \in [c_\alpha, c_\beta], \tag{3.18}$$

where $\chi_{[a,b]} = \begin{cases} 1, & s \in [a,b] \\ 0, & s \notin [a,b] \end{cases}$ is the characteristic function.

Similarly, we can derive the gradient of cost functional with respect to transference number (for simplicity of notation, the dependence on the concentration is dropped) by starting with introducing variables V and Q as defined in Eqn. (3.7) and (3.8). The perturbation system for c' is the same as Eqn. (3.9), but with the following definitions

$$V'(x,t) = D(c) c'(x,t;t^{+'}), \tag{3.19}$$

$$Q'(x,t) = -\left[\frac{dt^+}{dc} c'(x,t;t^{+'})\right] \frac{i}{FA} + \left[t^{+'}\right] \frac{i}{FA}. \tag{3.20}$$

As the next step, we multiply the perturbation equation on both sides with the second adjoint variable c^{**} and integrate over space and time. Then, we perform integration by parts and use boundary and initial conditions to eliminate the boundary terms.

The resulting identity is given below

$$\int_0^L \left[[c' c^{**}]_{t=T} - \int_0^T \frac{\partial c^{**}}{\partial t} c' dt \right] dx$$
$$= \int_0^T \left[- \left[\frac{\partial c^{**}}{\partial x} V' \right]_0^L + \int_0^L V' \frac{\partial^2 c^{**}}{\partial x^2} dx - \int_0^L Q' \frac{\partial c^{**}}{\partial x} dx \right] dt. \quad (3.21)$$

Using, V' and Q' from (3.19), we can finally obtain the second adjoint system as

$$-\frac{\partial c^{**}}{\partial t} = D \frac{\partial^2 c^{**}}{\partial x^2} + \left(\frac{dt^+}{dc} \right) \frac{i}{FA} \frac{\partial c^{**}}{\partial x} + (c - \tilde{c}), \quad (3.22a)$$

$$\left. \frac{\partial c^{**}}{\partial x} \right|_{x=0,L} = 0, \quad (3.22b)$$

$$c^{**}|_{t=T} = 0. \quad (3.22c)$$

With this assumed form of the adjoint system, we can express the directional derivative of cost functional (3.1) with respect to $t^+(c)$ as follows

$$\mathcal{J}'(D, t^+; t^{+'}) = \int_0^T \int_0^L \frac{\partial c^{**}}{\partial x} t^{+'} dx dt. \quad (3.23)$$

Using the Riesz representation theorem, the gradient of the cost functional in the L^2 space can be expressed as

$$\nabla_{t^+}^{L^2} \mathcal{J}(s) = \int_0^T \int_0^L \delta(s - c(x,t)) \frac{\partial c^{**}}{\partial x} dx dt, \quad (3.24)$$

where $\delta(s - c)$ is the Dirac delta distribution. Eqn. (3.18) and (3.24) are the expressions for the gradient of cost functional in L^2 space. However, before they can be used in iterations (3.2), their smoothed versions must be obtained.

3.2.1 Gradient in Sobolev Space

In the previous section, we derived gradient expressions in the L^2 space. However, as pointed out in earlier studies [14, 13], such gradients are not suitable for the reconstruction of material properties, because they are undefined outside the identifiability region $\mathcal{I}$ and they can potentially be discontinuous. Therefore, in order to ensure suitable smoothness and domain of definition of the gradients, we will define them in the Sobolev space $H^1(\mathcal{I})$ of functions of the concentration c with square-integrable derivatives, i.e., in problem P2 we set $\mathcal{X} = H^1(\mathcal{I})$. This space is endowed with the following inner product, cf. (3.5a)–(3.5b) (as we did above, we focus here on $\nabla_D \mathcal{J}$ with the transformation for $\nabla_{t^+}\mathcal{J}$ being analogous)

$$\left\langle \nabla_D^{H^1}\mathcal{J}, D' \right\rangle_{H^1(\mathcal{I})} = \int_{c_\alpha}^{c_\beta} \left(\nabla_D^{H^1}\mathcal{J}\, D' + \ell^2 \frac{d\nabla_D^{H^1}\mathcal{J}}{ds}\frac{dD'}{ds} \right) ds, \tag{3.25}$$

where ℓ is a parameter with the meaning of a "length-scale". Invoking again Riesz' representation theorem [47], now for the inner product (3.25) in the Sobolev space H^1, we obtain from (3.4a)

$$\mathcal{J}'([D, t^+]; D') = \left\langle \nabla_D^{L^2}\mathcal{J}, D' \right\rangle_{L^2} = \left\langle \nabla_D^{H^1}\mathcal{J}, D' \right\rangle_{H^1}. \tag{3.26}$$

Using integration by parts we deduce from (3.25)–(3.26)

$$\int_{c_\alpha}^{c_\beta} \nabla_D^{L^2}\mathcal{J}\, D'(s)\, ds = \int_{c_\alpha}^{c_\beta} \left(\nabla_D^{H^1}\mathcal{J}\, D' - \ell^2 \frac{d^2\nabla_D^{H^1}\mathcal{J}}{ds^2} D' \right) ds + \left[\frac{d\nabla_D^{H^1}\mathcal{J}}{ds} D' \right]_{s=c_\alpha}^{s=c_\beta} \tag{3.27}$$

and then, recognizing that the perturbation $D' \in H^1(\mathcal{I})$ is arbitrary except for the assumption that it satisfies the homogeneous Neumann boundary conditions at the endpoints $c = c_\alpha, c_\beta$, we arrive at the following second-order boundary value problem defining the new smooth gradient $\nabla_D^{H^1}\mathcal{J}$ in terms of the L^2 gradient obtained in (3.18):

$$\nabla_D^{H^1}\mathcal{J} - \ell^2 \frac{d^2 \nabla_D^{H^1}\mathcal{J}}{ds^2} = \nabla_D^{L^2}\mathcal{J} \qquad \text{on } (c_\alpha, c_\beta), \tag{3.28a}$$

$$\frac{d}{ds}\nabla_D^{H^1}\mathcal{J} = 0 \qquad c = c_\alpha, c_\beta. \tag{3.28b}$$

Transformation of the L^2 gradient into H^1 Sobolev gradient can be interpreted as a low-pass filtering which suppresses high-frequency noise and this property is necessary to eliminate the discontinuities which may potentially arise in the L^2 gradients [68]. The degree of noise filtration is determined by the Sobolev parameter ℓ with higher values of ℓ resulting in smoother Sobolev gradients. The Sobolev parameter ℓ is chosen by trial and error and it is usually the lowest possible value for which the reconstructed material properties are monotonic as a function of c. The boundary conditions (3.28b) imply a certain behavior of the reconstructed material properties $\widehat{D}(c)$ and $\widehat{t^+}(c)$ at the endpoints of the interval $[c_\alpha, c_\beta]$, namely, that their derivatives with respect to c are unchanged as compared to the initial guesses $D^{(1)}$ and $t^{+\,(1)}$, cf. (3.2c).

3.3 Solution of Optimization Problem P1

Obtaining optimal $\widehat{D}$ and $\widehat{t^+}$ as constants (problem P1) is the first step in the reconstruction of $D(c)$ and $t^+(c)$ as functions of the concentration and they serve as the initial guess for the problem P2. This first step in itself can give us insights about the material used and can also provide a credible validation of the model and experimental technique [59]. This constant parameter optimization is carried out using the in-built MATLAB function `fminsearch`, which uses a simplex search method. Initial guess for D is given in the order of 10^{-10} and for t^+ in the range between 0 and 1. The surface plot of the dependence of the cost functional $\mathcal{J}(D, t^+)$ on D and t^+ is also shown in Fig. 3.1 to demonstrate the presence of unique minima.

3.4 Solution of Optimization Problem P2

Reconstructing the concentration dependent material properties is $D(c)$ and $t^+(c)$ is a task that involves various steps. They are described in following sections.

3.4.1 Gradient Validation

As we are using an optimization approach to reconstruct material properties, the gradient of the cost functional with respect to material properties plays a key role in this study. So, it is very important to make sure that the gradients which are derived from the adjoint analysis in Section 3.2 (cf. (3.18) and (3.24)) are accurate. To obtain the gradient of the cost functional with respect to the control variable, we need to solve the governing PDE (2.12) and the adjoint PDEs (3.15) and (3.22), and then evaluate the expressions for gradient (3.18) and (3.24)) .

To validate the gradients derived using adjoint analysis, we use a technique called the "κ-test". In the κ-test an arbitrary perturbation of the control variable is assumed

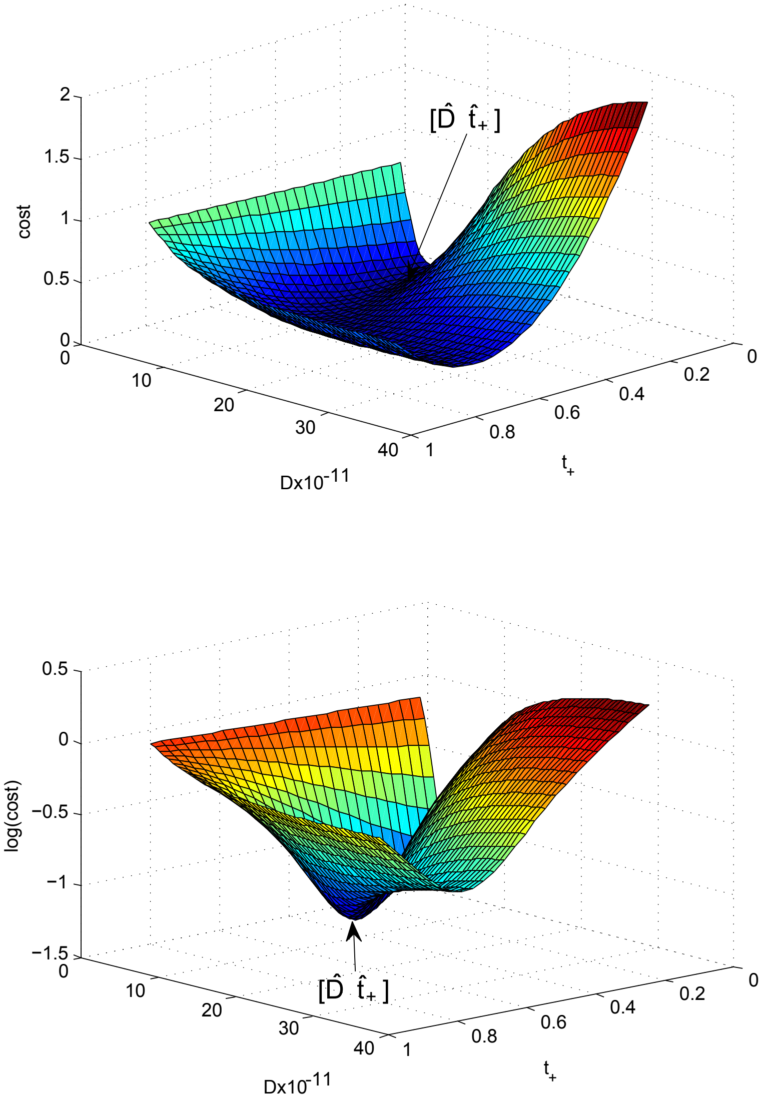

Figure 3.1: Surface plot of cost functional (3.1) value plotted against D and t^+ for P1 problem

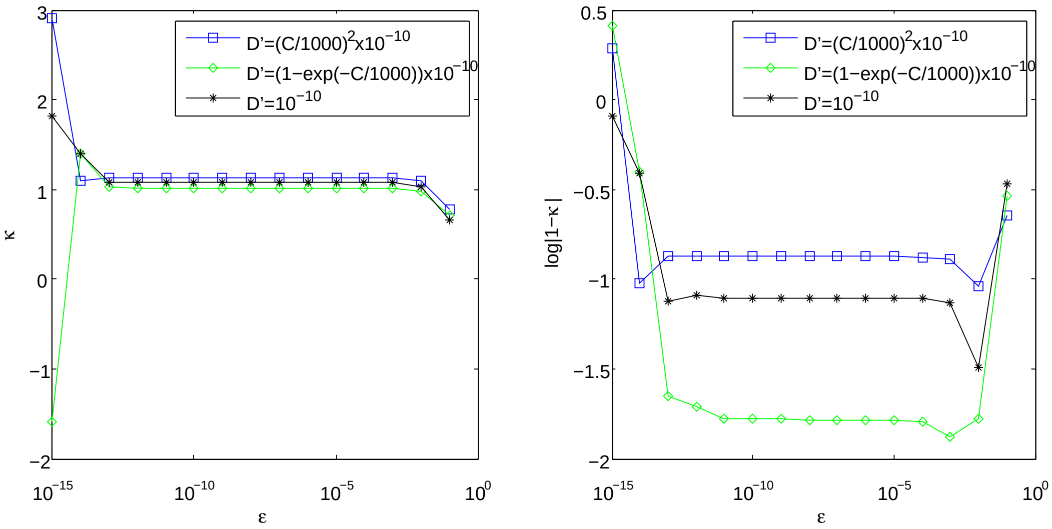

Figure 3.2: κ test to validate $\nabla_D^{L_2}\mathcal{J}$ using three different perturbation function D' represented in a) linear and b) log scale

and the corresponding directional derivative approximated using finite differences is compared with its Riesz representation that involves the gradient with respect to the control variable in the L^2 space. The ratio of these two quantities is defined as $\kappa(\epsilon)$, where ϵ is the size of the perturbation. For the control variable $D(c)$ we can define $\kappa(\epsilon)$ as

$$\kappa(\epsilon) = \frac{\epsilon^{-1}\left[\mathcal{J}(D+\epsilon D') - \mathcal{J}(D)\right]}{\int_{c_\alpha}^{c_\beta} \nabla \mathcal{J}_D^{L_2}(s) D'(s) ds}, \tag{3.29}$$

where D' is the perturbation. If the gradients are perfectly accurate, the parameter $\kappa(\epsilon)$ should be equal to one for all ϵ, but as we use approximations while solving PDEs and while evaluating the expression for gradient, we expect the values of $\kappa(\epsilon)$ to be only close to one. Fig. 3.2 shows the κ-test result that validates the gradient $\nabla_D^{L_2}\mathcal{J}$. Since the validation of $\nabla_D^{L_2}\mathcal{J}$ is to make sure that the adjoint analysis and its implementation are correct, the κ test was carried out for a test problem with "manufactured experimental" data. For κ test, three different D' functions are used

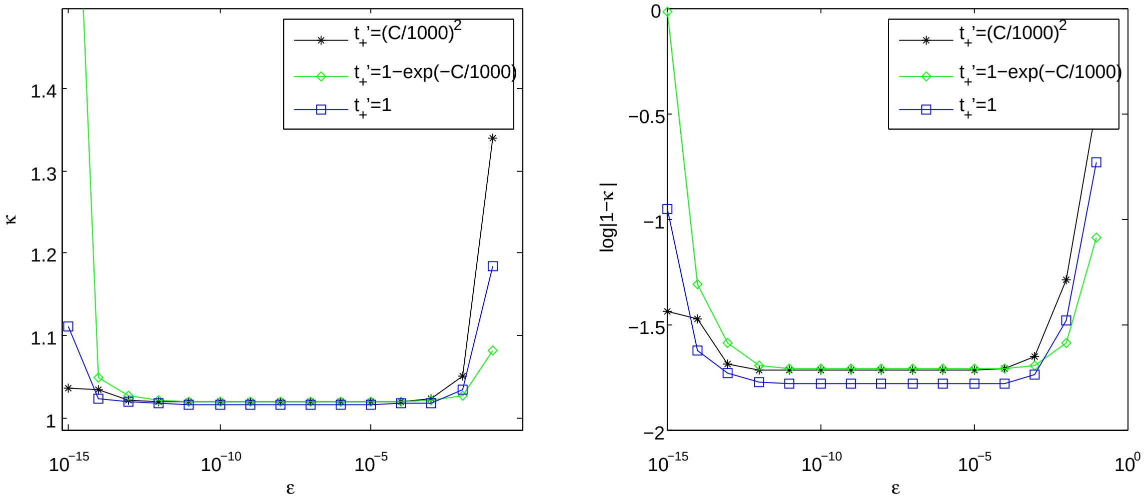

Figure 3.3: κ test to validate $\nabla^{L_2}_{t^+}\mathcal{J}$ using three different perturbation function represented in linear and log scale

(exponential, quadratic and constant) and are plotted as three distinct curves in Fig. 3.2. As we expect, the κ values are close to one for fairly large range of ϵ. The accuracy drops rapidly due to round-off errors for small values of ϵ and due to truncation errors for large values of ϵ. The same test for the gradient $\nabla^{L_2}_{t^+}\mathcal{J}$ is conducted and the results are presented in Fig. 3.3. These tests are carried out for the governing system (2.12) described in chapter 2 and during various stages of code development. Satisfactory results of the κ-test indicate that the cost functional gradients are sufficiently accurate to be used for the optimization algorithm.

3.4.2 Reconstruction Algorithm

As discussed extensively, the cost functional (3.1) and its gradients play a central role in the reconstruction of material properties (diffusion coefficient and transference number) via the solution of problem P2. The reconstruction algorithm is built based on a gradient descent method (3.2) using the gradients derived by solving the governing Eqn. (2.12) along with adjoint Eqn. (3.15) and (3.22). The conjugate gradient method is used as an accelerated optimization approach for its simplicity and its proven ability to reduce computational time [80]. The Fletcher-Reeves conjugate direction $\mathbf{g}[\nabla\mathcal{J}]$ is given by,

$$\begin{cases} \mathbf{g}_0\left[\nabla\mathcal{J}\right] = \nabla\mathcal{J}_0 \\ \mathbf{g}_n\left[\nabla\mathcal{J}\right] = \nabla\mathcal{J}_n + \frac{\nabla\mathcal{J}_n^T\nabla\mathcal{J}_n}{\nabla\mathcal{J}_{n-1}^T\nabla\mathcal{J}_{n-1}}\mathbf{g}_{n-1}\left[\nabla\mathcal{J}\right] \qquad n = 1, 2, 3, .., \end{cases} \tag{3.30}$$

where n is iteration number. Along with the conjugate gradient method, Brent's line-minimization technique is used to determine the optimal step length ξ_n in each iteration [13]. With consideration of all above mentioned components, the following algorithm is employed for the reconstruction of material properties by solving the sequence of problem P1 and P2.

Algorithm 1 : Iterative minimization algorithm for finding material properties as a function of concentration.
Input: $\varepsilon_{\mathcal{J}}$ - adjustable tolerance, $l^{(n)}$ - Sobolev parameter as function of iteration number, $\tilde{c}(x,t)$ - Experimental concentration values, $\tilde{D}, \tilde{t}^{+}$ - constant initial guesses for diffusion coefficient and transference number
Output: $D(c)$ and $t^{+}(c)$

```
Solution of problem P1, $[\hat{t}^{+}\ \hat{D}] \leftarrow \underset{t^{+},D\in\mathbb{R}^2}{\operatorname{argmin}} \mathcal{J}$ using MATLAB function fminsearch
$D^{(0)} \leftarrow$ ones(c)$\times\hat{D}$. Initial guess.
$t^{+(0)} \leftarrow$ ones(c)$\times\hat{t}^{+}$. Initial guess.
$n \leftarrow 1$
repeat
    solve governing Eqn. (2.12) and adjoint Eqn. (3.15)
    evaluate $\nabla_D^{L_2}\mathcal{J}$ and solve (3.28) to determine the Sobolev gradient $\nabla_D^{H^1}\mathcal{J}$
    compute the conjugate direction $\mathbf{g}\left[\nabla_D^{H^1}\mathcal{J}\right]$ using (3.30)
    perform line minimization $\hat{\tau} \leftarrow \underset{\tau}{\operatorname{argmin}} \left\{\mathcal{J}\left(D^{(n-1)} - \tau\,\mathbf{g}\left[\nabla_D^{H^1}\mathcal{J}\right], t^{+(n-1)}\right)\right\}$
    $D^{(n)} \leftarrow D^{(n-1)} - \hat{\tau}\,\mathbf{g}\left[\nabla_D^{H^1}\mathcal{J}\right]$
    solve governing Eqn. (2.12) and adjoint Eqn. (3.22)
    evaluate $\nabla_{t^+}^{L_2}\mathcal{J}$ and solve (3.28) to determine the Sobolev gradient $\nabla_{t^+}^{H^1}\mathcal{J}$
    compute the conjugate direction $\mathbf{g}\left[\nabla_{t^+}^{H^1}\mathcal{J}\right]$ using (3.30)
    perform line minimization $\hat{\tau} \leftarrow \underset{\tau}{\operatorname{argmin}} \left\{\mathcal{J}\left(D^{(n)}, t^{+(n-1)} - \tau\,\mathbf{g}\left[\nabla_{t^+}^{H^1}\mathcal{J}\right]\right)\right\}$
    $t^{+(n)} \leftarrow t^{+(n-1)} - \hat{\tau}\,\mathbf{g}\left[\nabla_{t^+}^{H^1}\mathcal{J}\right]$
    $n \leftarrow n+1$
until $|\mathcal{J}(D^{(n)}, t^{+(n)}) - \mathcal{J}(D^{(n-1)}, t^{+(n-1)})| < \varepsilon_{\mathcal{J}}|\mathcal{J}(D^{(n)}, t^{+(n)}|$
```

To gain insight about the performance of Algorithm 1, a validation problem is set up and the target concentration values are "manufactured" using an arbitrarily assumed concentration dependent diffusion coefficient function and transference

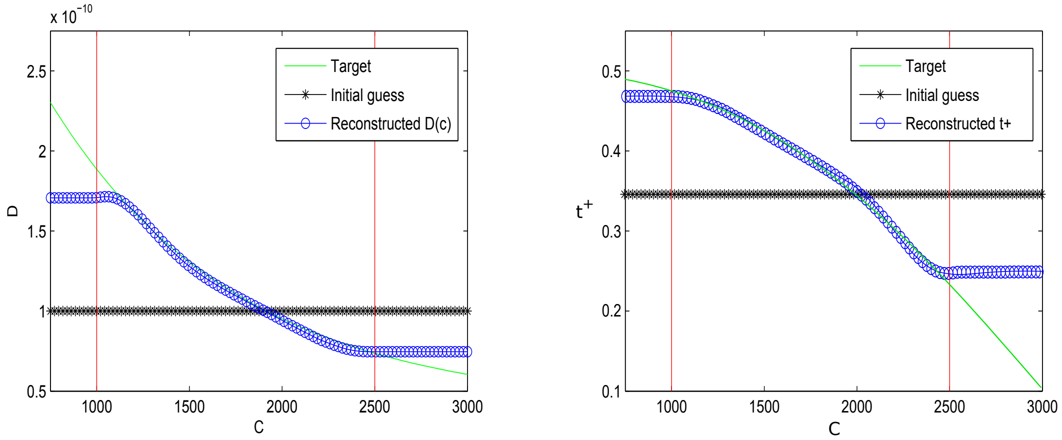

Figure 3.4: Solution of problem P2 with only (a) concentration-dependent diffusivity $D(c)$ and (b) concentration dependent transference number $t^{+}(c)$ as unknowns. For validation purposes manufactured concentration measurements are used. The vertical lines indicate the boundaries of identifiability region.

number (resembling the actual dependence of D and t^{+} on c). The optimization to reconstruct the diffusion coefficient is carried out with manufactured concentration values using Sobolev gradients. The results are shown in Fig. 3.4. It is clear form the figure that the reconstructions are sufficiently accurate and closely match the target values of $D(c)$ and $t^{+}(c)$. In the next chapter we will discuss how to quantify uncertainty of these reconstructed material properties.

Chapter 4

Uncertainty Quantification

This Chapter is derived from the results published in the article which appeared in the Journal of Computational Chemistry [78]. My role in this effort was to develop and validate the computational framework for uncertainty quantification. Our collaborators Dr. Sergey Krachkovskiy and Dr. Gillian Goward from the Department of Chemistry, McMaster University, provided us with the experimental data. This chapter concerns an important aspect of this research as it addresses the question of how uncertainty quantification can be incorporated into the reconstruction of unknown material properties via inverse modelling.

4.1 Introduction

In this study, we develop and validate a probabilistic framework for quantifying uncertainty in the reconstruction of unknown material properties of the electrochemical system from experimental data using inverse modelling. In our research, the experimental measurements are usually contaminated with noise. An important question is how this affects the accuracy of the reconstructed material properties. The reason is that inverse problem often tend to be "ill-posed" [30], meaning that small modifications of the input data (measurements) may result in significant changes in the obtained solution (here, the reconstructed material properties). Therefore, in order to have confidence in the obtained results, it is necessary to quantify how the measurement uncertainty translates into the uncertainty of the reconstructed material properties and, if more than one quantity is reconstructed (as was the case in [79]), whether the uncertainties of the reconstructed quantities are mutually correlated. An emerging approach which casts the problem of uncertainty quantification in probabilistic terms is Bayesian inference. In this framework, which blends prior hypotheses on unknown parameters with information from measurements in a systematic manner, the reconstructions of parameters are given in terms of suitable probability densities. General references to Bayesian inference include [81, 91], whereas a more general perspective which also involves continuous problems described by differential equations was developed in [86]. Recently, there has been a growing interest in Bayesian approaches to the solution of inverse problems with applications in electrical impedance tomography [37], atmospheric science [10, 12], contaminant source identification [50], ground water modelling [72], etc.. However, in the field of electrochemistry such techniques are uncommon, although they have been applied to quantify uncertainty in diagnostics and prognostics of batteries [73], and state estimation in battery management systems [74]. The proposed approach is quite general and as such may be applicable to a broad range of similar problems in chemistry governed by macroscopic models. The main novelty, and at the same time the largest difficulty which had to be overcome, is that the uncertainty needs to be quantified for material properties reconstructed in a *continuous* setting.

The structure of this chapter is as follows: in the next section we describe the class of electrochemical systems of interest to us, review their models and the inverse-modelling approach, and then introduce the Bayesian formulation of uncertainty quantification; the proposed approach is validated using synthetic data in Section 4.3.1, whereas an application involving actual experimental data is presented in Section 4.3.2; conclusions and final remarks are deferred to Section 4.5.

4.2 Methodology

In this section we describe different constituents of our methodology: we start with the measurement data, then introduce the Planck-Nernst system as a mathematical model for the problem, after that we review the inverse-modelling approach which is followed by the presentation of a Bayesian strategy for uncertainty quantification.

4.2.1 Experimental Measurements

Here we recall the setup of 'Experiment I' from Chapter 2, Section 2.1.1, where the imaging measurement sequence was repeated at 2-hour intervals uniformly spread over 16 hours duration of the galvanostatic experiment. The experimentally obtained concentration profiles, hereafter denoted $\tilde{c}(x,t)$ in this chapter, are shown in Fig. 4.1 at different times $t \in [0, 16 \text{ hours}]$ as functions of the space coordinate x. Further details concerning this experiment can also be found in [79].

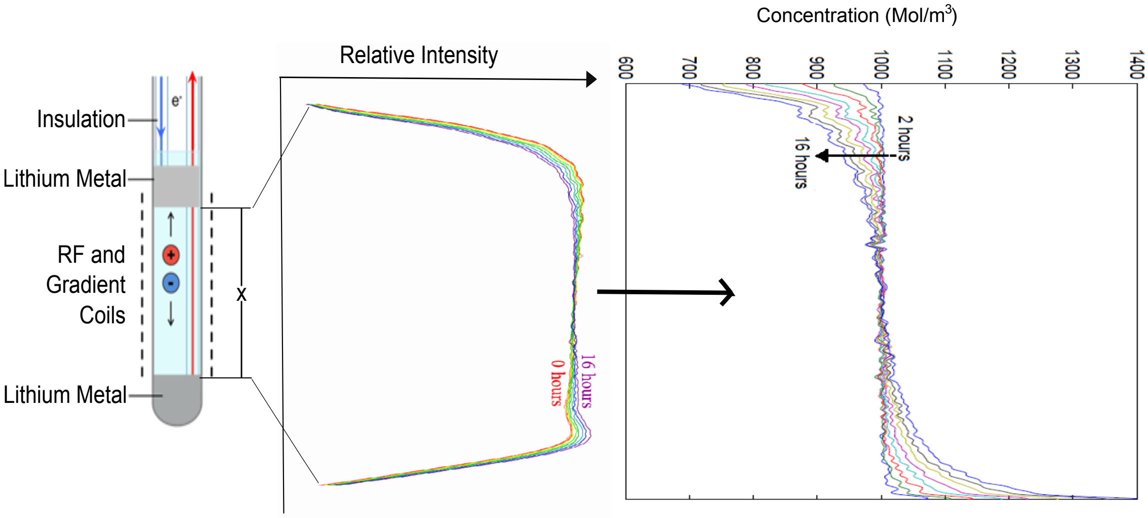

Figure 4.1: Experimental setup and the measured concentration data $\tilde{c}(x,t)$ used in the present study.

4.2.2 The Planck-Nernst Model

Here we recall the classical Planck-Nernst model used to describe the transport of charged species in dilute electrolytes from Chapter 2 and based on the assumptions outlined in Section 2.2, we consider a 1D problem with the spatial coordinate $x \in [0, L]$, where L is the length of the electrolyte filled region in the cell, and time $t \in [0, T]$, where T denotes the duration of the experiment. The assumptions lead to the following partial differential equation (PDE) describing mass transport in the electrolyte solution (4.1a), subject to the boundary conditions (4.1b) and the initial condition (4.1c):

$$\frac{\partial c}{\partial t} = \frac{\partial}{\partial x}\left[D\frac{\partial c}{\partial x} + \frac{(1-t^+)\,I}{FA}\right] \qquad \text{in } (0,L)\times(0,T], \tag{4.1a}$$

$$\left.\frac{\partial c}{\partial x}\right|_{x=0,L} = -\frac{(1-t^+)\,I}{DFA} \qquad \text{in } (0,T], \tag{4.1b}$$

$$c\big|_{t=0} = c^{\text{init}} \qquad \text{in } (0,L), \tag{4.1c}$$

The Fickian diffusion coefficient D and the transference number t^+ are considered unknown and will be reconstructed from the experimental data $\tilde{c}$ using the inverse modelling approach described in the following subsection. To simplify our notation, we will denote the pair of unknown material properties m, regardless of whether these properties are constant ($m = [D, t^+]$), or concentration-dependent ($m = [D(c), t^+(c)]$). The solutions of system (4.1) then define a map $\mathcal{L}$ from the material properties m to the space and time-dependent concentrations, i.e.,

$$c(x, t; m) = \mathcal{L}(m), \qquad 0 \leq x \leq L,\ 0 \leq t \leq T. \tag{4.2}$$

4.2.3 Inverse Modeling

Here we briefly recall the formulation of the inverse modelling technique as an optimization problem. The error functional can thus be represented as

$$\mathcal{J}(m) = \frac{1}{2} \sum_{i=0}^{N_T} \int_0^L \left[c(x, t_i; m) - \tilde{c}(x, t_i)\right]^2 \, dx, \tag{4.3}$$

where N_T is the number of time points t_i where the concentration profiles are acquired during the experiment. We will consider two distinct formulations corresponding, respectively, to constant and to concentration-dependent material properties.

$$\text{P1}: \qquad [\widehat{D}, \widehat{t^+}] = \underset{[t^+, D] \in \mathbb{R}^2}{\operatorname{argmin}} \, \mathcal{J}([D, t^+])$$

$$\text{P2}: \qquad [\widehat{D}(c), \widehat{t^+}(c)] = \underset{[t^+(c),\, D(c)] \in \mathcal{X}}{\operatorname{argmin}} \, \mathcal{J}\left([D(c), t^+(c)]\right),$$

where $\mathcal{X}$ denotes a suitable function space to which the pair $[D(c), t^+(c)]$ belongs. The functions $D(c)$ and $t^+(c)$ are defined on the interval $[c_\alpha, c_\beta]$ bounded by some minimum and maximum concentrations c_α and c_β, respectively. The approach to solve P2 has the general form of iterative gradient-based minimization

$$D^{(n+1)}(c) = D^{(n)}(c) - \xi_D^{(n)} \, \nabla_D \mathcal{J}\left(D^{(n)}(c), t^{+(n)}(c)\right) \qquad n = 1, 2, \dots, \tag{4.4a}$$

$$t^{+(n+1)}(c) = t^{+(n)}(c) - \xi_{t^+}^{(n)} \, \nabla_{t^+} \mathcal{J}\left(D^{(n+1)}(c), t^{+(n)}(c)\right) \qquad n = 1, 2, \dots, \tag{4.4b}$$

$$[D^{(\infty)}(c), t^{+(\infty)}(c)] = [\widehat{D}, \widehat{t^+}], \tag{4.4c}$$

where $\nabla_D \mathcal{J}$ and $\nabla_{t^+} \mathcal{J}$ are the gradients (sensitivities) of error functional (4.3) with respect to perturbations of, respectively, $D(c)$ and $t^+(c)$, whereas $\xi_D^{(n)}$ and $\xi_{t^+}^{(n)}$ are the corresponding lengths of the descent steps in the two directions. The calculation of gradients via adjoint analysis is explained in Section 3.2, whereas additional details and validation of the optimization algorithm are provided in Section 3.4.

The estimates of the material properties obtained by solving problems P1 and P2 are optimal, in the sense of minimizing the error with respect to measurements, cf. (4.3). Such inverse problems are however known to be often "ill-posed", meaning that the presence of noise in the measurement data may significantly affect the reconstructed solution [30, 89]. The sensitivity of the obtained reconstructions to perturbations of the data may be probed by performing a Monte-Carlo analysis [79] in which problems P1 and P2 are solved repeatedly using measurements $\tilde{c}$ artificially contaminated with independent noise samples with an assumed (e.g., normal) distribution and magnitude determined by the known size of the measurement errors. While this approach provides valuable insights about the sensitivity of the reconstructed material properties to noise in the data, it does not quantify their uncertainty in the sense of indicating which values of the material properties are most likely. A solution to this problem is presented in the next subsection.

4.2.4 Bayesian Approach to Uncertainty Quantification

We assume here that both the measurements $\tilde{c}(x,t)$ and the reconstructed material properties $[D, t^{+}]$, or $[D(c), t^{+}(c)]$ denoted as m, are random variables characterized by certain probability density functions (PDFs). More precisely, in the case of concentration-dependent properties, $D(c)$ and $t^{+}(c)$ are given by suitable probability distributions for *all* concentration values $c \in [c_\alpha, c_\beta]$ and the same also applies to the measurements $\tilde{c}$ for different values of $x \in [-0, L]$ and $t \in [0, T]$.

It is important to note that in Bayesian framework, the probabilities are quantifying a state of knowledge and in our case the state of knowledge or how well we know about the material properties given the evidence of the experimental data. This framework also is elegant and powerful in a way that it is able to account for various sources of uncertainty. The probability distribution of the reconstructed material properties are given in terms of the *posterior probability* $\mathbb{P}(m|\tilde{c})$, which is the probability of m attaining a certain value (in problem P2, for a given concentration c) given observations $\tilde{c}$, and can be expressed using Bayes' rule [86, 81, 91]

$$\mathbb{P}(m|\tilde{c}) = \frac{\mathbb{P}(\tilde{c}|m)\,\mathbb{P}(m)}{\mathbb{P}(\tilde{c})}, \tag{4.5}$$

where $\mathbb{P}(m)$ is the *prior* distribution reflecting our a priori assumptions about the solution, $\mathbb{P}(\tilde{c}|m)$ is the *likelihood* of observing particular experimental data for a given set of material properties, whereas $\mathbb{P}(\tilde{c})$ is a normalizing factor.

In terms of the prior distribution $\mathbb{P}(m)$, one can take the distribution of m obtained by performing a Monte-Carlo sensitivity analysis of the deterministic inverse problems P1 and P2, as described at the end of section 4.2.3. This is accomplished by solving problems P1 and P2 $N \geq 1$ times, each time using the original measurements $\tilde{c}$ perturbed with normally-distributed noise with a magnitude given by the known size of experimental errors. The obtained material properties m are then used to construct the prior distribution $\mathbb{P}(m)$. This step appears as STAGE 1 in Algorithms 2 and 3 below. We note that this analysis does not account for how good the fits are, in terms of the value of the error functional (4.3), for various samples of the noise perturbing the measurements. An alternative, neutral, approach would be to take "uninformative" priors given by uniform distributions of m.

As regards the likelihood function, the following ansatz is typically adopted in Bayesian inference [86, 81, 91]

$$\mathbb{P}(\tilde{c}|m) \propto e^{-\mathcal{J}(m)}, \tag{4.6}$$

which expresses the assumption that for a given set of material properties m, measurements resulting in large values of the error functional (4.3) are less likely to be observed. The likelihood function $\mathbb{P}(\tilde{c}|m)$ is approximated by sampling the distribution in (4.6) using the Metropolis-Hastings algorithm [16] to produce M samples. This algorithm is based on the Markov-Chain Monte-Carlo (MCMC) approach [32] employed to sample form the probability distribution of m and at each step involves the solution of the governing system (4.1) for modified (trial) material properties m^* followed by the evaluation of the error functional (4.3). At each step, the algorithm moves in the probability space collecting samples from the probability distribution (4.5). A move in the probability space is accepted or rejected based on a sample acceptance ratio γ defined based on the posterior distribution (4.5) (see Algorithm 2 and 3). If one attempts to move to a point in the probability space that is more probable than the existing point, the move is accepted. On the other hand, if one attempts to move to a less probable point, the algorithm rejects the move with some probability based on the steepness of the probability decrease in the given direction. Thus, the trajectory tends to sample frequently from high-probability regions while occasionally also sampling from low-probability regions. The MCMC algorithm involves a "burn-in" process in which a certain number (usually the first 10%) of the total number M of accepted samples is discarded to avoid outliers common at initial stages.

While application of the Metropolis-Hastings algorithm is fairly straightforward in the finite-dimensional setting of problem P1, it is more delicate in the continuous setting of problem P2. The main difficulty is in constructing random perturbations of the concentration-dependent material properties $D(c)$ and $t^+(c)$ in a way that they will remain smooth enough for the Planck-Nernst system (4.1) to be well defined (normally, these functions should be at least once continuously differentiable and this issue is also addressed in Chapter 3). This is achieved by parameterizing the material properties in terms of their truncated cosine-series representations

$$\begin{aligned} m_P(c) &= \frac{\hat{m}_0}{2} + \sum_{k=1}^{P} \hat{m}_k \cos\left[\frac{2\pi k(c-c_\alpha)}{c_\beta - c_\alpha}\right], \quad c \in [c_\alpha, c_\beta] \qquad (4.7) \\ \text{where} \quad \hat{m}_k &= \frac{2}{c_\beta - c_\alpha} \int_{c_\alpha}^{c_\beta} m(c) \cos\left[\frac{2\pi k(c-c_\alpha)}{c_\beta - c_\alpha}\right] dc, \quad k = 1, \dots, P \end{aligned}$$

and the number of terms P is a discretization parameter. The choice of the cosine-series expansion is dictated by the assumed homogeneous behavior of $D(c)$ and $t^+(c)$ at $c = c_\alpha, c_\beta$. The Metropolis-Hastings algorithm is initialized with a function $m_P(c)$ for which the cosine-series coefficients in (4.7) vanish as $|\hat{m}_k| \sim \mathcal{O}(k^{-2})$. New trial samples are generated by multiplying the cosine-series coefficients $\hat{m}_1, \dots, \hat{m}_P$ by independent random numbers η_k, $k = 1, \dots, P$, chosen such that $|\eta_k| < C$ for all k, where $C > 0$ is a parameter fixed based on the acceptance rate of the Metropolis-Hastings algorithm. For sufficiently large P this approach approximates a continuous random distribution while preserving the required smoothness of the trial material properties $[D(c), t^+(c)]$. The proposed computational approach for Bayesian uncertainty quantification is summarized as Algorithms 2 and 3 for the problems with constant and concentration-dependent material properties, respectively, and is validated in Section 4.3.1. A discussion about the choice of prior distribution is presented in Section 4.4.

Algorithm 2 : Two-stage algorithm to estimate the posterior probability distribution of constant material properties

MATLAB Functions:
`normrnd(M,S)` — MATLAB function that samples from normal random distribution with mean M and standard deviation S,
`fminsearch`— MATLAB function that uses Nelder-Mead simplex algorithm to minimize cost function.

Input:
$\tilde{c}$ — experimental data,
N, M — numbers of samples generated in STAGE 1 and STAGE 2
$\varepsilon_{\mathcal{J}}$ — tolerance in the solution of problem P1 in STAGE 1
$m^{(0)}$ — initial guess in the solution of problem P1 in STAGE 1
$\bar{m}^{(0)}$ — initial guess sample in STAGE 2
C — parameter controlling randomization in in STAGE 2

Output:
an approximation of the posterior probability distribution $\mathbb{P}(m|\tilde{c})$

```
STAGE 1: Construct $N$ samples for prior distribution $\mathbb{P}(m)$
repeat
    perturb measurements $\tilde{c}$ with normally-distributed noise (magnitude given by the size of experimental errors)
    find $\widehat{m}$ by solving problem P1 (using function fminsearch and initial guess $m^{(0)}$)
    store $\widehat{m}$ as a sample for prior distribution
until $N$ prior distribution samples are obtained
assimilate samples to construct $\mathbb{P}(\bar{m})$

STAGE 2: Construct $M$ samples for posterior distribution $\mathbb{P}(m|\tilde{c})$
construct initial sample $\bar{m}^{(0)}$
$k$=0
repeat
    create a new trial position $\bar{m}^* = \bar{m}^k +$ normrnd$(\bar{0}, C)$
    calculate acceptance ratio $\gamma = \frac{\mathbb{P}(\bar{m}^{(*)}|\tilde{c})}{\mathbb{P}(\bar{m}^{(k)}|\tilde{c})}$
    if $\gamma \geq$ rand(1):    $\bar{m}^{(k+1)}$=$\bar{m}^{(*)}$;    $k$=$k+1$,
    else:                        discard $m^{(*)}$
    $k = k + 1$
until $M + M/10$ samples are obtained for posterior distribution
discard the first $M/10$ samples
assimilate the remaining samples to construct posterior probability distribution $\mathbb{P}(m|\tilde{c})$
```

Algorithm 3 : Two-stage algorithm to estimate the posterior probability distribution of constant material properties

MATLAB Functions:

`normrnd(M,S)` — MATLAB function that samples from normal random distribution with mean M and standard deviation S,

`fminsearch`— MATLAB function that uses Nelder-Mead simplex algorithm to minimize cost function.

Input:

$\tilde{c}$ — experimental data,

N, M — numbers of samples generated in STAGE 1 and STAGE 2

$\varepsilon_{\mathcal{J}}$ — tolerance in the solution of problem P2 in STAGE 1

$\hat{m}$ — initial guess in the solution of problem P2 in STAGE 1, (here the solution of problem P1 is used as $\hat{m}$)

$\bar{m}^i$ — initial sample in STAGE 2 (chosen such that $\bar{m}^i \in \mathcal{X}$)

C — parameter controlling randomization in in STAGE 2

Output:

an approximation of the posterior probability distribution $\mathbb{P}(m|\tilde{c})$

```
STAGE 1: Construct N samples for prior distribution of $\mathbb{P}(\bar{m})$
repeat
    perturb measurements $\tilde{c}$ with normally-distributed noise (magnitude given by the size of experimental errors)
    $\bar{m}^{(0)}=\hat{m}$ (initial guess)
    $n=1$
    repeat
        solve governing system (4.2)
        evaluate $\nabla_{\bar{m}}\mathcal{J}$.
        compute the conjugate direction $\mathbf{g}\left[\nabla_{\bar{m}}\mathcal{J}\right]$
        perform line minimization: $\tau_{\bar{m}}^{(n-1)} = \underset{\tau}{\operatorname{argmin}} \left\{\mathcal{J}\left(\bar{m}^{(n-1)} - \tau\,\mathbf{g}\left[\nabla_{\bar{m}}\mathcal{J}\right],\right)\right\}$
        update: $\bar{m}^{(n)} = \bar{m}^{(n-1)} - \tau_{\bar{m}}^{(n-1)}\,\mathbf{g}\left[\nabla_{\bar{m}}\mathcal{J}\right]$
        $n=n+1$
    until $|\mathcal{J}(\bar{m}^{(n)}) - \mathcal{J}(\bar{m}^{(n-1)})| < \varepsilon_{\mathcal{J}}|\mathcal{J}(\bar{m}^{(n)})|$
    store $\bar{m}^{(n)}$ as prior distribution sample
until N prior distribution samples are obtained
assimilate samples to construct $\mathbb{P}(\bar{m})$.
STAGE 2: Construct M samples for posterior distribution $\mathbb{P}(\bar{m}|\tilde{c})$
$\bar{m}^{(0)}=\bar{m}^i$
$k=1$
repeat
    create a new trial position $\bar{f}^* = \bar{f}^k \times$ normrnd$(\bar{0}, C)$
    using inverse Fourier transform obtain $\bar{m}^{(*)}$
    calculate acceptance ratio $\gamma = \frac{\mathbb{P}(\bar{m}^{(*)}|\tilde{c})}{\mathbb{P}(\bar{m}^{(k)}|\tilde{c})}$
    if $\gamma \geq$ rand(1):    $\bar{m}^{(k+1)}=\bar{m}^{(*)}$;    $k=k+1$,
    else:                        discard $\bar{m}^{(*)}$
until M+M/10 samples are obtained for posterior distribution
discard the first $M/10$ samples
assimilate the remaining samples to obtain posterior probability distribution
```

4.3 Results

4.3.1 Validation

In this section, we validate the Bayesian approach to uncertainty quantification introduced in Section 4.2.4. In addition to establishing its consistency, this will also allow us to assess how the results it produces depend on key numerical parameters and properties of the data. We will do this for both problems P1 and P2 using an approach based on "manufactured solutions" [14, 13], where certain values of D and t^+ (in problem P1), or functional forms of $D(c)$ and $t^+(c)$ (in problem P2), are initially assumed and used to generate ”measurements" by solving system (4.1). After being contaminated with the noise of prescribed magnitude, this data is used to solve inverse problems P1 and P2 and then to quantify the uncertainty of the obtained reconstructions using Algorithms 2 and 3. In particular, this approach allows one to determine how the uncertainty of the reconstructions depends on the level of noise in the data. This validation study does not consider model inaccuracy and systematic errors, which might be inherently present in the system.

For problem P1 we assume $D = 10^{-10}$ m^{2}s^{-1} and $t^+ = 0.4$, whereas the assumed functional forms of $D(c)$ and $t^+(c)$ in problem P2 are shown with thick dashed lines in Fig. 4.5a and 4.5b, respectively. We also assume that the electrochemical cell has length $L = 0.002$ m and diameter 0.001 m, the applied current is $I = 100\ \mu$A and the initial salt concentration is $c^{\text{init}} = 1000$ mol m^{-3}, whereas the duration of the experiment is $T = 20$ hours, all of which are in the ballpark of parameters used in practice. System (4.1) and its adjoint (3.15) are solved numerically in MATLAB

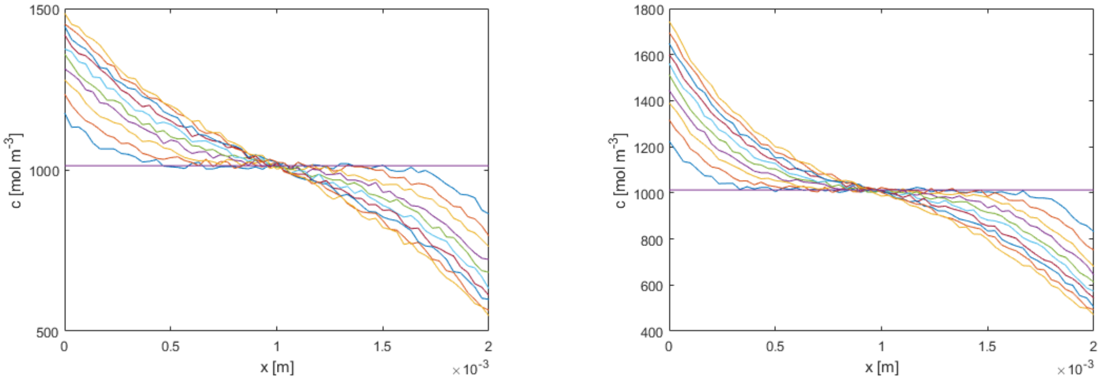

(a) (b)

Figure 4.2: Concentration profiles $\tilde{c}(x,t_i)$, $i = 1,\ldots,N_T$, manufactured by solving problem (4.1) using (a) assumed constant material properties $[D,t^+]$ and (b) assumed concentration-dependent material properties $[D(c),t^+(c)]$. In both cases the added noise has standard deviation $\xi = 25$ mol m^{-3}.

with the routine `pdepe` which uses adaptive spatial discretization and adaptive time-stepping adjusted such that the relative and absolute tolerances, respectively 10^{-8} and 10^{-10}, are satisfied at all points in time and space. Computed concentration profiles recorded at $N_T = 10$ equispaced time levels t_i, $i = 1,\ldots,N_T$, are used as the measurements $\tilde{c}(x,t_i)$ (the integral with respect to time t in (4.3) is therefore replaced with summation over $i = 1,\ldots,N_T$). Measurements generated in this way are then perturbed with normally-distributed noise with the frequency 20 kHz and standard deviation $\xi = 25$ mol m^{-3}. The concentration profiles $\tilde{c}(x,t_i)$, $i = 1,\ldots,N_T$, obtained with constant $[D,t^+]$ and concentration-dependent material properties $[D(c),t^+(c)]$ are shown in Figures 4.2a and 4.2b, respectively. When sampling the likelihood function $\mathbb{P}(\tilde{c}|m)$ in Algorithm 3 expression (4.7) is used with $P = 50$ terms. The constant C is fixed at a value where the ratio of number of accepted samples to the total MCMC step attempted is approximately 0.2.

We begin the presentation of the results by analyzing the effect of the number

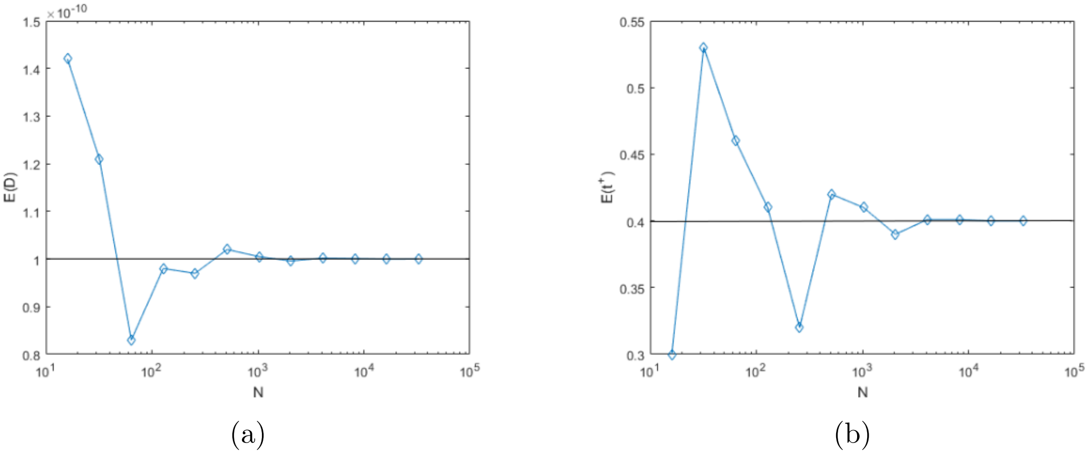

(a) (b)

Figure 4.3: Convergence of the expected (constant) values of (a) D and (b) t^+ to the true values indicated with horizontal lines as the number of samples N and $M = N$ used in Algorithm 2 is increased. Measurement data is available at $N_T = 10$ time levels and the noise standard deviation is $\xi = 25$ mol m^{-3}.

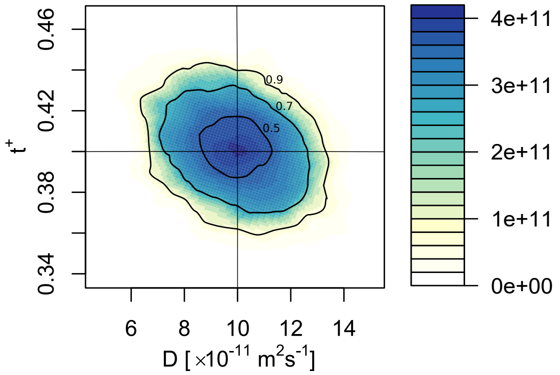

Figure 4.4: Joint posterior probability distribution of the constant diffusion coefficient D and transference number t^+. Measurement data is available at $N_T = 10$ time levels and the noise standard deviation is $\xi = 25$ mol m^{-3}. The contour lines indicate the boundaries of the credibility region with the corresponding credibility values indicated next to the contour lines.

of samples used to approximate the prior probability distribution and the likelihood function $\mathbb{P}(\tilde{c}|m)$ on the convergence of the expected values of the constant material properties in Fig. 4.3. For simplicity, we set $M = N$ in Algorithm 2. In Fig. 4.3a and 4.3b we see that as the number of Monte-Carlo samples N increases the expected values of D and t^+ estimated based on the posterior probability distributions $\mathbb{P}(m|\tilde{c})$ produced by Algorithm 2, converge to their true values. Acceptable accuracy is achieved already for $N = 5,000$, which is the number of samples we will use below. Next, in Fig. 4.4, we present the joint probability density of the constant material properties D and t^+ based on the posterior distributions obtained with Algorithm 2. The approximately circular shape of the isolines in this figure indicates that there is no significant correlation between the uncertainties in the reconstruction of the diffusion coefficient and the transference number. The corresponding results obtained with Algorithm 3 for the problem with concentration-dependent material properties are presented in Fig. 4.5a and 4.5b for $D(c)$ and $t^+(c)$, respectively, together with the corresponding true distributions. The contour plots shown in these figures should be interpreted such that their sections at a given value of c produce the posterior probability distributions functions $\mathbb{P}(D(c)|\tilde{c})$ and $\mathbb{P}(t^+(c)|\tilde{c})$. We observe that, unlike in Fig. 4.5b where the most likely values of the transference number $t^+(c)$ are quite close to the true distribution for all values of c, in Fig. 4.5a a systematic difference between the most likely reconstructed values of $D(c)$ and the true values is evident. We remark here that in the absence of noise in the data, the concentration-dependent diffusion coefficient $D(c)$ obtained by solving problem P2 is inferred very accurately and coincides with the true distribution up to the graphical resolution for all values of c (this result is not shown). Hence, we can conclude that the differences evident

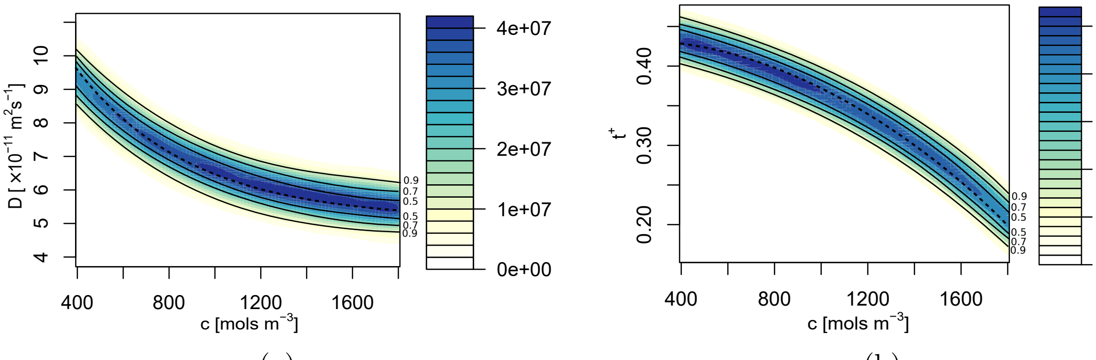

(a) (b)

Figure 4.5: Posterior probability densities of (a) the diffusion coefficient $D(c)$ and (b) the transference number $t^+(c)$ as functions of the concentration c. Measurement data is available at $N_T = 10$ time levels and the noise standard deviation is $\xi = 25$ mol m^{-3}. The thick dashed lines represent the chosen $D(c)$ and $t^+(c)$. The contour lines indicate the boundaries of the credibility region with the corresponding credibility values indicated next to the contour lines.

in Fig. 4.5a are induced by noise and as such can be attributed to the ill-posedness of the inverse problem (cf. the discussion in Introduction).

We now move on to characterize the impact of the noise level in the data $\tilde{c}$ on the uncertainty of the reconstructed material properties. This is done by using noise with three different values of standard deviation $\xi = 25, 50, 75$ mol m^{-3} and computing the posterior distribution of the constant and concentration-dependent material properties, $[D, t^+]$ and $[D(c), t^+(c)]$, using Algorithms 2 and 3. The results are presented, respectively, in Figures 4.6a and 4.7, where they are shown in terms of the 95% credibility bounds defined as the boundaries of parameter regions over which the posterior probability density integrates to 0.95. In this study, we estimate the credibility region by finding an isoline of the PDF function such that over the region enclosed by this isoline, this PDF integrated to 0.95. We use the R function `NIntegrate` on a probability density region with a threshold value for the PDF and then optimize with this threshold value used as a control variable to match the desired

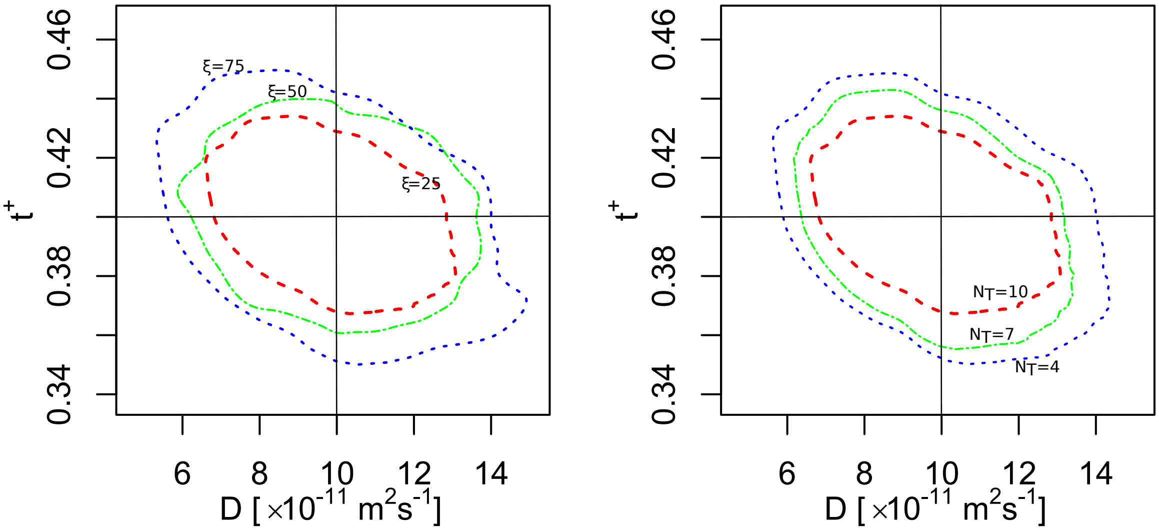

(a) (b)

Figure 4.6: Boundaries of the 95% credibility regions in the joint posterior probability distributions of the constant diffusion coefficient D and transference number t^+ obtained with (a) concentration profiles $\tilde{c}(x, t_i)$ available at $N_T = 10$ time levels and perturbed with noise of different magnitudes (dashed — $\xi = 25$ mol m^{-3}, dot-dash — $\xi = 50$ mol m^{-3}, dotted — $\xi = 75$ mol m^{-3}) , (b) concentration profiles $\tilde{c}(x, t_i)$ available at different numbers of time levels (dashed — $N_T = 10$, dot-dash — $N_T = 7$, dotted — $N_T = 4$) and perturbed with noise of magnitude $\xi = 25$ mol m^{-3}.

credibility value. In this optimization step, we use the `FindRoot` function in R to perform the optimization. For concentration-dependent properties, the credibility range is collected for all discrete concentration values and they are plotted as a function of concentration. We observe in these figures that the credibility regions corresponding to different noise levels have similar shapes and in all cases shrink as the noise level is reduced, which is the expected behavior.

We close this section by analyzing the effect of the amount of available measurement data on the uncertainty of the reconstructed material properties. This is done by varying the number N_T of the time points t_i where measurements $\tilde{c}(x, t_i)$, $i = 1, \ldots, N_T$, are available ($N_T = 4, 7, 10$) while keeping the noise standard deviation

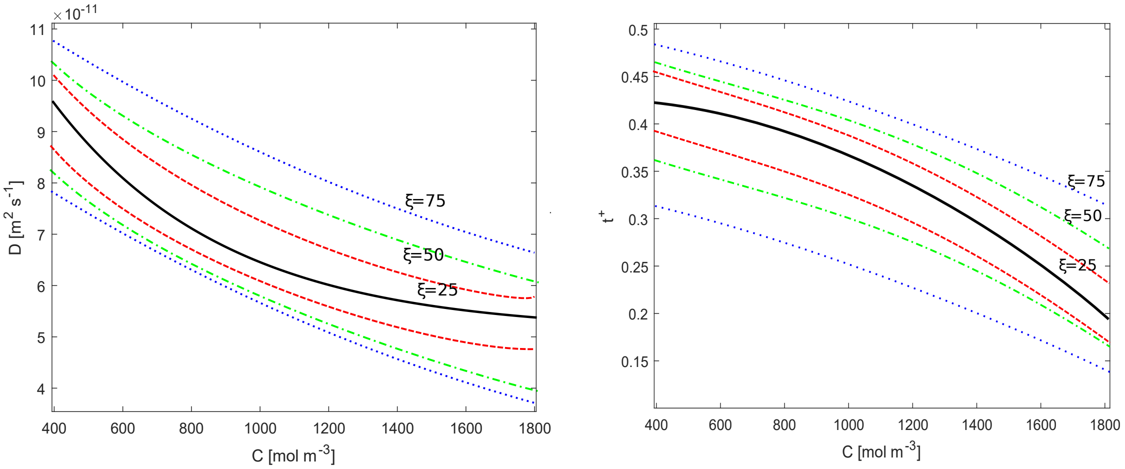

(a) (b)

Figure 4.7: Boundaries of the 95% credibility regions in the posterior probability distributions of (a) the diffusion coefficient $D(c)$ and (b) the transference number $t^+(c)$ for different concentration values. The results are obtained using concentration profiles $\tilde{c}(x, t_i)$ available at $N_T = 10$ time levels and perturbed with noise of different magnitudes (dashed — $\xi = 25$ mol m^{-3}, dot-dash — $\xi = 50$ mol m^{-3}, dotted — $\xi = 75$ mol m^{-3}). The thick solid lines represent the true distributions of $D(c)$ and $t^+(c)$.

fixed at $\xi = 25$ mol m^{-3}. The results obtained for problems with constant and concentration-dependent material properties, $[D, t^+]$ and $[D(c), t^+(c)]$, are presented, respectively, in Figures 4.6b and 4.9, again using the 95% credibility bounds for the posterior probability distributions determined with Algorithms 2 and 3. We can conclude from these figures that the effect of reducing the amount of available data is qualitatively similar to the effect of increasing the noise level in the data, as the uncertainty grows when N_T is decreased.

4.3.2 Application to Experimental Data

In this section we apply the methodology for uncertainty quantification described in Section 4.2.4 and validated in Section 4.3.1 to the inverse problems P1 and P2

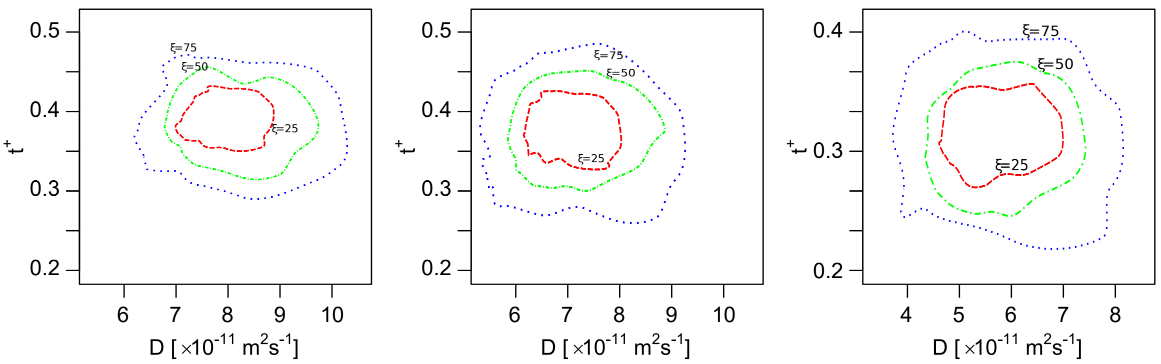

(a) (b) (c)

Figure 4.8: Boundaries of the 95% credibility regions of the joint posterior probability distributions of the diffusion coefficient $D(c)$ and the transference number $t^+(c)$ for different concentration values (a) $c = 700$ mol m^{-3} (b) $c = 1100$ mol m^{-3} (c) $c = 1500$ mol m^{-3}. The results are obtained using concentration profiles $\tilde{c}(x, t_i)$ available at $N_T = 10$ time levels and perturbed with noise of different magnitudes (dashed — $\xi = 25$ mol m^{-3}, dot-dash — $\xi = 50$ mol m^{-3}, dotted — $\xi = 75$ mol m^{-3}). The thick solid lines represent the true distributions of $D(c)$ and $t^+(c)$.

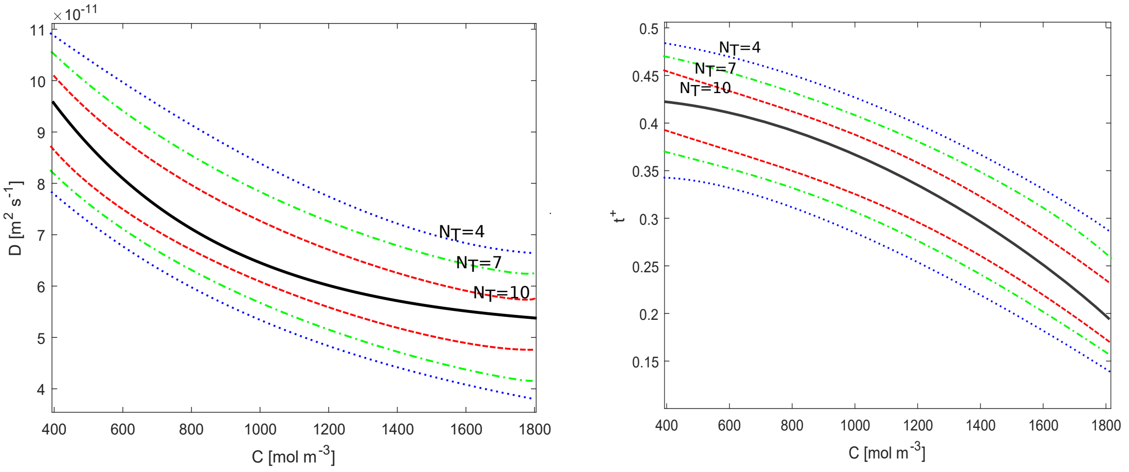

(a) (b)

Figure 4.9: Boundaries of the 95% credibility regions in the posterior probability distributions of (a) the diffusion coefficient $D(c)$ and (b) the transference number $t^+(c)$ for different concentration values. The results are obtained using concentration profiles $\tilde{c}(x, t_i)$ available at different numbers of time levels (dashed — $N_T = 10$, dot-dash — $N_T = 7$, dotted — $N_T = 4$) and perturbed with noise of magnitude $\xi = 25$ mol m^{-3}. The thick solid lines represent the true distributions of $D(c)$ and $t^+(c)$.

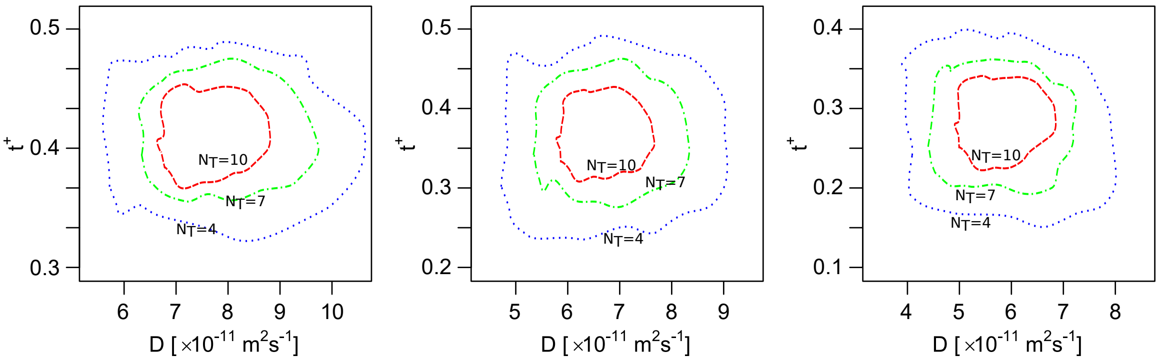

(a) (b) (c)

Figure 4.10: Boundaries of the 95% credibility regions of the join posterior probability distributions of the diffusion coefficient $D(c)$ and the transference number $t^+(c)$ for different concentration values (a) $c = 700$ mol m^{-3} (b) $c = 1100$ mol m^{-3} (c) $c = 1500$ mol m^{-3}. The results are obtained using concentration profiles $\tilde{c}(x, t_i)$ available at different numbers of time levels (dashed — $N_T = 10$, dot-dash — $N_T = 7$, dotted — $N_T = 4$) and perturbed with noise of magnitude $\xi = 25$ mol m^{-3}. The thick solid lines represent the true distributions of $D(c)$ and $t^+(c)$.

involving, respectively, constant and concentration-dependent material properties and using the experimental data described in Section 4.2.1. The joint posterior probability density obtained for constant $[D, t^+]$ is shown in Fig. 4.11a, whereas the posterior probability densities of $D(c)$ and $t^+(c)$ as functions of the concentrations c are shown in Figures 4.11b and 4.11c. In addition, in Figures 4.12a–4.12c we also present the joint posterior probability densities of $[D(c), t^+(c)]$ for three selected concentration values (these distributions are extracted from the data in Figures 4.11b and 4.11c by constructing sections at the indicated values of c).

First, in Fig. 4.11 we note that the expected values of both constant and concentration-dependent material properties as well as the trends with changes in the concentration revealed in the latter case agree with the results known from the literature [79]. In Fig. 4.11a we also observe that the reconstructed constant material properties exhibit significant uncertainties which, unlike the validation results from

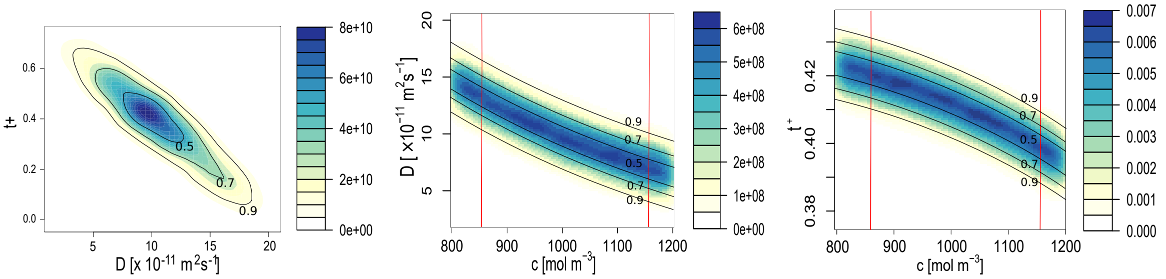

(a) (b) (c)

Figure 4.11: (a) Joint posterior probability distribution of the constant diffusion coefficient D and transference number t^+, posterior probability densities of (b) the diffusion coefficient $D(c)$ and (c) the transference number $t^+(c)$ as functions of the concentration c, all obtained based on the measurement data described in Section 4.2.1. The contour lines indicate the boundaries of the credibility region with the corresponding credibility values indicated next to the contour lines.

Fig. 4.4, are correlated in the sense that larger values of the diffusion coefficient D are likely to occur together with smaller values of the transference number t^+, and vice versa. On the other hand, in the concentration-dependent case the reconstruction uncertainty is significantly reduced for both $D(c)$ and $t^+(c)$ for all concentration values c. In both cases this uncertainty is small relative to the variation of $D(c)$ and $t^+(c)$ over the entire range of c. Moreover, Figures 4.12a–4.12c demonstrates that, in contrast to the case of constant material properties, cf. Fig. 4.11a, in the concentration-dependent case there is no significant correlation between the uncertainties of $D(c)$ and $t^+(c)$ at particular values of c.

4.3.3 Computational Time

In this section, the computational time associated with various algorithms is discussed. The data from 'Experiment I' (section 2.1.1) and Planck-Nernst model (2.12) is used to obtain the computational time for estimating diffusion coefficient

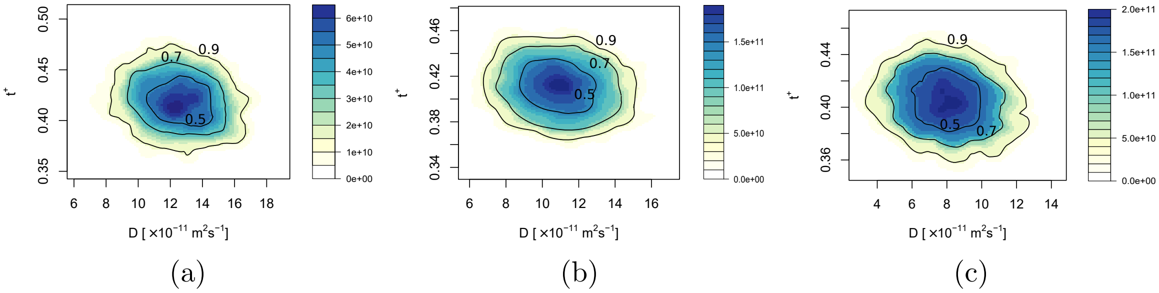

(a) (b) (c)

Figure 4.12: Joint posterior probability distribution of the concentration-dependent diffusion coefficient $D(c)$ and transference number $t^{+}(c)$ at the concentrations (a) $c = 900$ mol m^{-3}, (b) $c = 1,000$ mol m^{-3} and (c) $c = 1,100$ mol m^{-3}, cf. Figures 4.11b and 4.11c, obtained based on the measurement data described in Section 4.2.1. The contour lines indicate the boundaries of the credibility region with the corresponding credibility values indicated next to the contour lines.

Table 4.1: Computational times required to estimate material properties and quantify their uncertainty (all calculations performed on single core).

Problem	Gradient Descent	Monte-Carlo sampling	MCMC sampling
Sample size	1	5000	5000
P1 (min)	0.26	1142	32
P2 (min)	9.6	51164	396

(D) and transference number (t^+). We also estimate the computational time needed to quantify uncertainty in reconstructing the material properties and they are shown in Table 4.1. As the Monte-Carlo algorithm uses a gradient descent approach to obtain one sample, the number of times it needs to solve the governing system and adjoint system is much higher when compared to the MCMC algorithm. The computational time needed to obtain 5000 samples in the Monte-Carlo algorithm when compared against the MCMC algorithm is about 35 times larger for P1 problem and 130 times larger for P2, respectively. Based on the computational time, we can clearly see the advantage of using MCMC algorithm over Monte-Carlo for computing uncertainty.

4.4 Choice of The Prior Distribution

We note that, somewhat unconventionally, both the *prior* distribution and the *likelihood* function are derived based on the same experimental data. While in this validation study there is no choice (other than perhaps an uninformative prior), this will lead to tighter credibility bounds as discussed below. As a Monte-Carlo method is used to obtain prior, it contains the uncertainty information due to noise. On the other hand, the likelihood function, related to the error function ($\mathcal{J}$), quantifies the uncertainty due to the experimental errors and approximations inherent in the physics-based model. Though the prior and the likelihood distributions are derived in a fundamentally different way, the resulting posterior distribution may lead to a tighter bound because of the same data source. Indeed in Fig. 4.13, we can see that the knowledge we gain from both the prior and likelihood are similar and leads to a posterior distribution with lower uncertainty. Because of resulting lower uncertainty, this choice of prior distribution is not recommended. Therefore in our investigation in

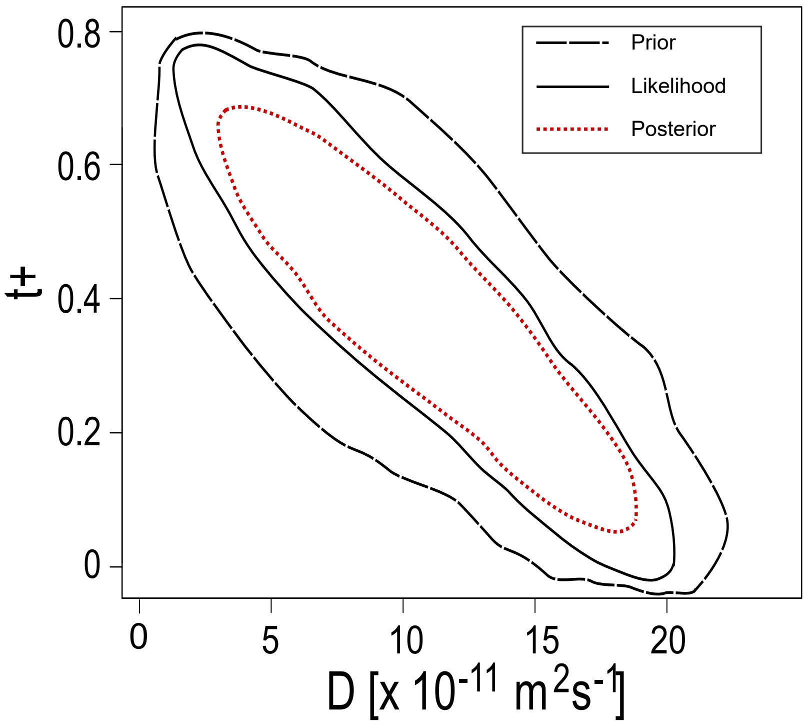

Figure 4.13: 95% credibility interval calculated for prior, likelihood and posterior probability distribution functions to show the effect of using prior and likelihood derived from same data.

Chapter 6, we use a prior obtained based on literature data reported for the material properties, which is more consistent with the traditional Bayesian approach.

4.5 Conclusions

In this study, we have developed and carefully validated a state-of-the-art Bayesian approach to quantify the uncertainty of material properties reconstructed from experimental data. This approach combines a recently developed inverse-modelling technique capable of inferring general concentration-dependent material properties subject to minimal assumptions [79] with a Markov-Chain Monte-Carlo method for sampling the likelihood function. We emphasize that while the present study focuses on an electrochemical system modeled by the Planck-Nernst equation (4.1), the proposed approach is in fact also applicable to a broad range of problems in chemistry where macroscopic models are used. Extensive numerical tests of the method confirm that it exhibits the expected behavior as different parameters are varied.

Application of the proposed approach to actual experimental data allows us to place rigorous “error bounds” in the reconstructed material properties. These results demonstrate that while the uncertainty can be non-negligible for constant material properties, it is significantly reduced in the concentration-dependent case. The reason for this is that the required regularity of $D(c)$ and $t^+(c)$ as functions of c imposes some constraints on how rapidly the material properties can vary with c. As a result, the reconstruction uncertainty is small relative to the range of variation of both $D(c)$ and $t^+(c)$, which offers confidence in the reliability of inverse modelling.

Chapter 5

Ion-Pairing Effects

This chapter is derived from the results published in a research article which appeared in the Journal of Electrochemical Society [69]. My role in this work was to develop the computational tools for the inverse modelling and extend Planck-Nernst model with ion-pairing effects along with our collaborators Dr. Giles Richardson, Dr. Jamie Foster and Dr. Ion Halalay. Our collaborators Dr. Sergey Krachkovskiy and Dr. Gillian Goward provided us with the experimental data. In this study we first demonstrate that inverse modelling performed using data from Experiment II described in Section 2.1.2 and the Planck-Nernst equation (2.12) produces negative transference numbers. Such a physically inconsistent reconstruction of a constitutive relation indicates the loss of validity of the Planck-Nernst equation as a mathematical model for this process. Then, we consider the formation of ion pairs and clusters as a possible effect responsible for the appearance of negative transference numbers and derive an extended version of the Planck-Nernst system which accounts for these additional species. However, a careful analysis of this model reveals that incorporation of ion-pairing effects into the modelling will not change the transference numbers inferred from the experimental data via inverse modelling. Thus, other effects need to be considered, which will be done in Chapter 6. The detailed analysis of ion-pairing effects is provided below in this chapter.

5.1 Introduction

In this study our collaborators Dr. Sergey Krachkovskiy and Dr. Gillian Goward determined Li concentration profiles in a symmetric Li-Li cell filled with 1M $LiPF_6$ in a binary mixture of ethylene carbonate (EC) and dimethyl carbonate (DMC) with a 1:1 ratio by volume under galvanostatic conditions. Applying the inverse modelling (IM) technique to the data obtained from this experiment leads to negative values of the transference number $t^+(c) < 0$ at large concentrations. For binary electrolytes based on lithium salts and neutral organic carbonates, such as the one used in our study, negative transference numbers are not possible [40, 99]. However, negative values of lithium transference numbers can occur for lithium salt/ionic liquid ternary mixtures with two cations and common anion, as reported in [33]. It has long been known that ion aggregation occurs in certain electrolytes, as has been deduced by Onsager from experiments in which the conductivity increases with field strength [62, 61]. Initially, we attributed the predicted negative transference numbers to the omission of ionic aggregation from the model noting that: (i) there is good evidence that such species can form in $LiPF_6$ in EC:DMC which has a relatively low dielectric permittivity ($\varepsilon \approx 30$) and therefore exhibits a high degree of ion association (ion pairing$> 50\%$) [40]; (ii) NMR experiments detect all Li nuclei independently of whether they are in the form of free cations or part of a larger aggregate; and (iii) ion pairs, being neutral, do not perform a migration motion in an applied electric field. Moreover, it has been postulated that a phenomenon which could give rise to negative transference numbers in binary systems are the formation and transport of ionic aggregates which form and disintegrate spontaneously at increased electrolyte concentrations [19]. We demonstrate in the present study that incorporation of ionic aggregation into an extended Nernst-Planck model does not in fact change the transference numbers that can be inferred from the data. It is therefore apparent that in order to obtain an accurate model of ion transport at high concentrations, one must augment the Nernst-Planck model with other physical effects such as those discussed in Chapter 6. The structure of the chapter is as follows. In Section 5.2 we describe the experiment to be modeled. Following that, we recall the standard Planck-Nernst model from Section 2.2 together with all its modelling assumptions, and we present results indicating the loss of its validity at moderate and high salt concentrations. An augmented model accounting for ion-pairing effects is introduced in Section 5.4, where careful analysis demonstrates that in the limit of fast reaction rates this augmented model remains formally equivalent to the original Planck-Nernst system.

5.2 Experimental

In this section we recall Experiment II described in Section 2.1.2 where we obtained concentration profiles, hereafter denoted $\tilde{c}(x,t)$, are shown in Fig. 2.4 at different times $t \in [0, 14 \text{ hours}]$ as functions of the space coordinate x.

5.3 The Planck Nernst Model

Assumptions and derivation of the standard Planck-Nernst model are presented in Section 2.2. They clearly show that only diffusion and migration are taken into account in describing the transport of the ions in the electrolyte. In this section, we use inverse modelling based on model (2.12) to estimate the material properties and the results are presented below.

5.3.1 Material Properties Estimates Based on the Nernst-Planck Model

In our prior investigation [76] the inverse modelling approach, described in Section 3.1, was applied to infer material properties of lithium bis(trifluoromethanesulfonyl)imide solutions in propylene carbonate with concentrations up to 1.1M and produced thermodynamically consistent reconstructions of the effective diffusivity and Li^+ transference number as functions of the salt concentration. However, when this approach is applied to the concentration profiles shown in Section 2.1.2, cf. Fig. 2.4, which feature salt concentrations up to 2.2 M, the results shown in Fig. 5.1 are no longer physically consistent. Specifically, while the reconstruction of the diffusion coefficient $D(c)$ is in the expected range, the reconstructed values of the Li^+ transference number $t^+(c)$ are negative for most of the salt concentrations, i.e., at $>$ 0.85M. Under assumptions A1–A8 from Section 2.2, a negative transference number t^+ implies that the cationic current due to migration has a direction opposite to the electric field, which is physically impossible for binary symmetric electrolytes. At the same time, we emphasize that the negative transference numbers were obtained as

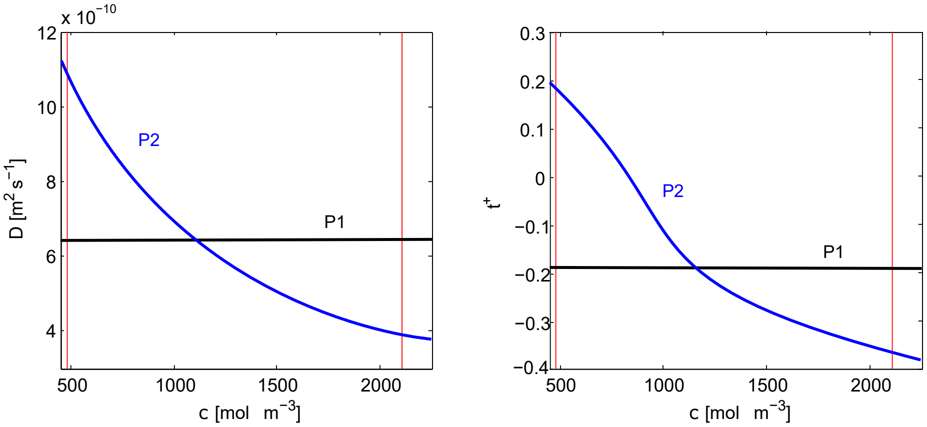

Figure 5.1: Constant and concentration-dependent effective salt diffusivities (left) and Li^+ transference numbers (right) reconstructed from the measurement data described in Section 5.2 using the inverse modelling approach (problems P1 and P2 defined in Appendix 6.4.1) based on system (2.12)

the constitutive relation in system (2.12) that allows this system to *optimally* match the experimental data, in the sense of minimization of the least-square error (for details, see the minimization problems P1 and P2 defined in Section 3.1). Therefore, such a result demonstrates that system (2.12) no longer provides a physically valid description of the data. This failure is clearly attributable to the fact that system (2.12) does not account for physical effects which become important at higher concentrations. Such effects may include the formation of neutral ion pairs, different forms of advection [45] or the motion of the reaction surface as dendrites are formed on the electrode surfaces. We will discuss the latter effect in the next chapter.

5.3.2 Prior Reports of Negative Cation Transference Numbers

Several prior studies have reported negative transference numbers and speculate about their possible origins. For example, investigation [21] provides evidence for a negative transference number measured in a lithium binary symmetric electrolyte. While the authors mention a number of possible reasons for negative transference numbers, they conclude that the formation of large complexes and high molecular weight of the anion may be the key factor. An analogous opinion is expressed in monograph [71] where the authors argue that formation of ion complexes of cations and anions with a net negative charge at a higher salt concentration in a non-symmetric electrolyte can result in a negative transference number. This hypothesis was also reinforced by other studies [24]. The thermodynamic validity of negative transference number was considered in [52]. Based on the analysis presented in that study, one can conclude that in principle negative transference numbers may arise under certain conditions in *non-binary* electrolytes. Since the experimental set-up discussed in Section 5.2 involves a binary electrolyte, this argument cannot explain the results reported in Section 5.3.1, cf. Figure 5.1. Hence, in the next section, we will address the question of whether ion-paring effects could be used to justify negative transference numbers.

5.4 Transport Model with Ion-Pairing Effects

In this section, we formulate a generalized version of the Nernst-Planck model discussed in Section 2.2 that explicitly accounts for the ion-pairing effects. We will then draw some conclusions about how this extension affects the reconstructions of material properties via inverse modelling. Henceforth, we will use the term "ion pair" to describe complexes that are formed when a positive and negative ion come sufficiently close together to become (reversibly) bound by their Coulombic interaction. The formation of an ion pair could then occur via the reaction $Li^{+}+A^{-} \rightleftharpoons LiA$, where A^{-} represents the anion in the binary symmetric salt LiA. Of course, it is conceivable that higher-order clusters (consisting of more than one of either the positive and negative ions) may form in electrolytic solutions and recent reports have indicated the presence of higher-order clusters in Li-ion battery electrolytes [90] based in molecular dynamics (MD) simulations. We note, however, that MD probes phenomena on time scale several orders of magnitude faster than the timescales for diffusion in liquids and no reports regarding the lifetime of higher-order clusters was provided. Furthermore, the absence of the signature typical for the existence of substantial amounts of triple ions in the ionic conductivity data for $\mathrm{LiPF_6}$/carbonates solutions is also reported [48]. Therefore, for simplicity, in this section, we neglect the presence of higher-order ion clusters. However, this analysis arrives at the same conclusions when extended to higher-order clusters, as demonstrated in Appendix A3.

Conservation equations for each of the three species in the system can be written as follows

$$\frac{\partial c_+}{\partial t} + \frac{\partial \mathcal{F}_+}{\partial x} = -Q(c_+, c_-, c_o), \tag{5.1a}$$

$$\frac{\partial c_-}{\partial t} + \frac{\partial \mathcal{F}_-}{\partial x} = -Q(c_+, c_-, c_o), \tag{5.1b}$$

$$\frac{\partial c_o}{\partial t} + \frac{\partial \mathcal{F}_o}{\partial x} = Q(c_+, c_-, c_o), \tag{5.1c}$$

where c_+, c_-, and c_o, are the cation, anion and ion-pair concentrations, respectively, $\mathcal{F}_+$, $\mathcal{F}_-$, and $\mathcal{F}_o$, are the corresponding fluxes (specified in Appendix A1), whereas $Q(c_+, c_-, c_o)$ is the rate of the ion-pair formation reaction. In symmetrical electrochemical cells with lithium metal electrodes, lithium is stripped from one electrode deposited onto the other. The possible electrochemical reactions that can lead to lithium deposition/stripping are [83]

$$\text{(I)} \quad \mathrm{Li} \rightleftharpoons \mathrm{Li}^+ + e^-, \tag{5.2a}$$

$$\text{(II)} \quad \mathrm{Li} + \mathrm{A}^- \rightleftharpoons \mathrm{LiA} + e^-. \tag{5.2b}$$

For reaction (I) we denote the forward reaction rate (per unit area) by $r_{(\mathrm{I})}$, on the electrode at $x = 0$, and by $R_{(\mathrm{I})}$, on the electrode at $x = L$. For reaction (II) we denote the forward reaction rate (per unit area) by $r_{(\mathrm{II})}$ on $x = 0$ and by $R_{(\mathrm{II})}$ on $x = L$. The appropriate boundary conditions on the ionic fluxes are thus

$$\mathcal{F}_+|_{x=0} = r_{(\mathrm{I})}, \tag{5.3a}$$

$$\mathcal{F}_-|_{x=0} = -r_{(\mathrm{II})}, \tag{5.3b}$$

$$\mathcal{F}_o|_{x=0} = r_{(\mathrm{II})}. \tag{5.3c}$$

$$\mathcal{F}_+|_{x=L} = -R_{(\mathrm{I})}, \tag{5.3d}$$

$$\mathcal{F}_-|_{x=L} = R_{(\mathrm{II})}, \tag{5.3e}$$

$$\mathcal{F}_o|_{x=L} = -R_{(\mathrm{II})}. \tag{5.3f}$$

which can, in turn, be related to the current density flowing through the device via

$$j|_{x=0} = \mathcal{F}(r_{(I)} + r_{(II)}), \quad \text{and} \quad j|_{x=L} = -\mathcal{F}(R_{(I)} + R_{(II)}). \tag{5.4}$$

5.4.1 Charge Neutrality

As is usual in such charge transport problems, at realistic ion concentrations there is almost exact charge neutrality

$$c_- \approx c_+$$

throughout nearly all of the electrolyte, except in very narrow Debye layers adjacent to the electrodes (typically of size around 1nm). This is a consequence of Poisson's equations and the very short Debye length of the electrolytes used in battery applications.

5.4.2 Reaction Quasi-Equilibrium

Borodin *et al.* [11] estimate the reaction rate for the dimerization reaction k to be of the order of 10^9s^{-1} and this allows us to determine how close to quasi-equilibrium the dimerization reaction will be. In the immediate vicinity of the electrodes, we do not expect the reaction to be close to equilibrium because the reactions occurring there act to drive the system away from equilibrium. However, by comparing the timescale for diffusion of ions L^2/D to the reaction rate timescale $1/k$ we can obtain an estimate of the length scale L away from the electrodes over which the system shows significant deviation from equilibrium. With an estimate of $D \approx 10^{-9}\text{m}^2\text{s}^{-1}$, this gives $L \approx 1\text{nm}$. Thus we expect the dimerization reaction to be at quasi-equilibrium throughout the electrolyte except in narrow *reaction layers*, of width $\approx 1\text{nm}$, in the immediate vicinity of the electrodes.

5.4.3 The Bulk Equations

Away from the Debye layers and reaction layers lying adjacent to the electrodes we expect almost exact charge neutrality and almost exact equilibrium of the dimerization reaction. These two assumptions allow us to considerably simplify the governing equations by writing

$$c_- = c \quad \text{and} \quad c_+ = c, \quad \text{(charge neutrality)} \tag{5.5}$$

and

$$c_o = F(c), \quad \text{(quasi-equilibrium of dimerisation reaction).} \tag{5.6}$$

Here the equilibrium function $F(c)$ can be obtained by balancing the chemical potential of the electrolyte with that of the dimer. We note that a mass action balance, as considered for example in [26], would give $[c_+][c_-] = M_F[c_o]^2$, with an equilibrium constant M_F. Therefore, we would have $F(c) = M_F c^2$ in (5.6), which is a special case of the present more general approach. In (5.5) and (5.6) we therefore have two equations for the three variables c_+, c_- and c_o, and we need a further equation and appropriate boundary conditions that will allow us to fully determine these variables.

5.4.4 A Transport Equation for Total Lithium Concentration in the Bulk

In order to close the problem for c_+, c_- and c_o in the bulk region (away from the Debye and reaction layers adjacent to the electrodes) we seek a diffusion equation for the total lithium concentration in the electrolyte

$$[\mathrm{Li}] = [\mathrm{Li}^+] + [\mathrm{Li\,A}] = c_+ + c_o. \tag{5.7}$$

This should be in a form in which the dimerisation reaction rate Q does not appear explicitly. Although the reaction occurs close to quasi-equilibrium *it is not necessarily* true that the Q terms in (5.1a)-(5.1c) are negligible. In addition, given the experiment that we are trying to model, we require a relation between the total lithium flux and the current density at the electrodes. Throughout nearly all the electrolyte (with the exception of the Debye layer) charge neutrality $c_- = c_+$ is satisfied and we can rewrite (5.7) in the form $[\mathrm{Li}] = \frac{1}{2}(c_+ + c_-) + c_o$. This motivates us to define the total lithium concentration c_T and the total lithium flux $\mathcal{F}_T$ (outside the Debye layer) by the expressions

$$c_T = \frac{1}{2}(c_+ + c_-) + c_o, \quad \text{and} \quad \mathcal{F}_T = \frac{\mathcal{F}_- + \mathcal{F}_+}{2} + \mathcal{F}_0. \tag{5.8}$$

We note that while c_T does not represent the total lithium concentration [Li] in the narrow Debye layer, it is still possible to write down a conservation equation for c_T throughout the entire electrolyte (including the Debye layer). This conservation equation can be obtained by adding twice (5.1c) to (5.1a) and (5.1b) and dividing the result by two which yields an equation that is independent of the volumetric reaction rate Q, namely

$$\frac{\partial c_T}{\partial t} + \frac{\partial \mathcal{F}_T}{\partial x} = 0. \tag{5.9}$$

Appropriate boundary conditions on this conservation equation for c_T can be derived by re-expressing $\mathcal{F}_T$ on the boundaries in terms of the reaction rates there, via (5.3a)-(5.3f) and (5.4). This results in two conditions that are independent of the reactions occurring in the boundary layers

$$\mathcal{F}_T|_{x=0} = \frac{j(t)}{2F}, \quad \text{and} \quad \mathcal{F}_T|_{x=L} = \frac{j(t)}{2F}. \tag{5.10}$$

The total lithium flux $\mathcal{F}_T$ is related to total lithium concentration c_T, except in the narrow Debye and reaction layers adjacent to the electrodes, via the relation

$$\mathcal{F}_T = -\widetilde{D}(c_T)\frac{\partial c_T}{\partial x} - \frac{j}{2F}(1 - 2t^+). \tag{5.11}$$

which is derived in Appendix A1, cf. equation (A.17). Even though this definition of the flux does not apply in the Debye and reaction layers, it holds in the central *bulk region* that extends across nearly the entire electrolyte. Since the Debye and reaction layers are narrow, their capacity for ions and ion pairs is low and consequently the total flux $\mathcal{F}_T$ across them is almost uniform (an argument that has been formalized by conducting a boundary layer analysis of equation (5.9), see appendix A2). Thus the boundary conditions (5.10) can be applied directly to the bulk flux $\mathcal{F}_T$, as defined in (5.11), even though this relation does not hold in the Debye and reaction layers adjacent to the reaction surfaces $x = 0, L$.

We note that when we substitute equation (5.11) for the flux into the conservation equation (5.9) and the boundary conditions (5.10), we retrieve equations (4.1a)–(4.1b) which were used in the original inverse modelling approach, namely,

$$\frac{\partial c_T}{\partial t} = \frac{\partial}{\partial x}\left(\widetilde{D}(c_T)\frac{\partial c_T}{\partial x}\right) - \frac{\partial t^+}{\partial x}\frac{j}{F}, \tag{5.12}$$

$$\widetilde{D}(c_T)\frac{\partial c_T}{\partial x}\bigg|_{x=0} = -\frac{j}{F}(1-t^+), \tag{5.13}$$

$$\widetilde{D}(c_T)\frac{\partial c_T}{\partial x}\bigg|_{x=L} = -\frac{j}{F}(1-t^+). \tag{5.14}$$

where here j is constant and related to the total current I via $j = I/A$. It is thus immediately apparent that invoking ion pairing cannot resolve the issue of negative transference numbers, since the system for the total lithium concentration that we obtain here is formally identical to the original system investigated in the inverse-modelling approach used to determine the electrolyte properties.

5.5 Conclusions and Outlook

The formal equivalence of the reduced system (5.12)–(5.14) with the effective diffusion coefficient $\widetilde{D}$, cf. (A.16), and the original Nernst-Planck model (2.12) demonstrates that accounting for ion-pairing under the assumption of fast reaction rates cannot affect the transference numbers reconstructed via inverse modelling. In particular, the incorporation of this effect will not resolve the problem highlighted in Section 5.3.1 where negative transference numbers were obtained from reconstructions. As demonstrated in Appendix A3, this conclusion still holds even when higher-order ion clusters are taken into account. These findings, therefore, call into question the claim made in [24] about the relation between negative transference numbers and ion pairing. Since the extended model introduced in Section 5.4 which accounts for ion pairing still cannot provide a physically consistent description of the galvanostatic experiment (cf. Section 5.2), one needs to consider other physical effects not accounted for in the Nernst-Planck model. One such candidate is the incorporation of the motion of the reaction surface owing to dendrite growth. Inverse modelling in the presence of such effects will be the topic in the next chapter.

Chapter 6

Effect of Dendrite Growth

This Chapter is derived from the results of a research article currently under review [77]. My role in this work was to develop inverse modelling and uncertainty quantification framework and also to develop an extended Planck-Nernst model to include dendrite growth in collaboration with Dr. Giles Richardson and Dr. Jamie Foster. The experimental data was provided by Dr. Sergey Krachkovskiy, Mr. David Bazak and Dr. Gillian Goward. Here we consider a modification of the Planck-Nernst model accounting for the loss of Lithium from the electrolyte due to the formation of dendritic structures near one of the electrodes, an effect which was observed in experiments. We use the tools of inverse modelling in combination with concentration measurements acquired with NMR to probe the validity of a modified Planck-Nernst model in which the depletion of Lithium is described in different ways.

6.1 Introduction

In the present investigation, we use the inverse-modelling approach to probe the validity of a family of mathematical models for the transport of charged species in electrolytes at moderate concentrations where a standard Planck-Nernst theory [55] is not sufficient. Once such a physically-consistent model is identified, it is used to infer optimal estimates of the diffusivity and the transference numbers (these estimates are *optimal* in a mathematically precise sense, because they minimize suitably defined prediction errors). Our focus here is on a canonical electrochemical experiment where a constant current applied across the electrodes [25, 64] is often described in terms of the Planck-Nernst theory based on assumptions A1–A8 and model (2.12) outlined in Section 2.2. While constant values of D and t^+ correspond to the dilute limit (small concentrations), concentration-dependent material properties $D(c)$ and $t^+(c)$ are used to effectively account for departures from the ideal behavior. In an earlier study [79] we were able to estimate consistent material properties using inverse modelling based on this model and an experiment featuring a rather narrow range of concentrations between 900 mols/m^3 to 1100 mols/m^3, demonstrating that system (2.12) provides an accurate description of transport phenomena in this regime. On the other hand, application of system (2.12) to model an experiment shown in Section 2.1.2 with a larger range of concentrations resulting from a higher applied current I leads to physically inconsistent negative transference numbers obtained via inverse modelling as shown in Section 5.3.1. The reason for this is that the Planck-Nernst model (2.12) does not account for some physical effects affecting transport in experiments conducted at higher concentrations. One such phenomenon is the formation of ion pairs and higher-order ion clusters. However, as was shown rigorously in Chapter 5

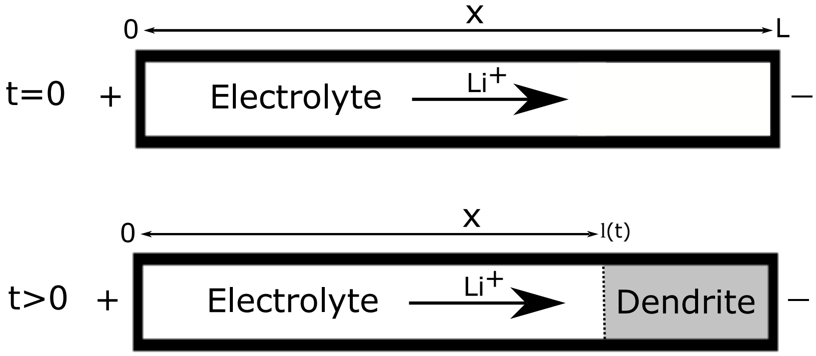

Figure 6.1: Schematic illustration of the electrochemical cell (a) at the beginning of the experiment (at time $t = 0$) when there is no dendritic growth and (b) in the course of the experiment (i.e., for $t > 0$) when the dendritic region grows from the negative (right) electrode. The standard Planck-Nernst model (2.12) is defined on the domain illustrated in panel (a), whereas the modification of this model given in (6.1) accounts for the presence of the dendritic region shown in panel (b).

and [69], this effect cannot in fact influence the transference numbers inferred from the measured concentration profiles via inverse modelling. Influence from advection effects where there is a motion induced in the liquid owing to the intrusion (recession) of plating (stripping) electrode. Based on the current of 75 μA and a tube diameter of 5 mm, we estimate that if the electrode interface were to remain planar (consistent with assumption A4) and metallic, then the velocity of the interface, $\dot{s}$, would be about 7.29 $\mathring{A}/sec$. By then comparing the sizes of the fluxes driven by diffusion (Dc/L), migration ($(1 - t^{+})I/(FA)$) and advection ($\dot{s}c$), we find that advective effects are insignificant (driving fluxes around one hundred times smaller) compared to diffusion or migration.

In the present study, we focus on another effect, namely, deposition of lithium from the electrolyte in the form of dendritic structures near one of the electrodes [95, 57]. This phenomenon leads to the formation of a porous matrix influencing lithium transport in the affected region, cf. Figure 6.1, and has been the subject of numerous investigations surveyed in the recent monograph [97] (in fact, analogous questions have also been studied for electrodes made from different metals [8]). Some studies reported that when a single dendrite grows from the substrate, deposition occurs on its tip due to the strength of the electric field [51, 18, 2, 3]. However, because of their plastic deformation, the dendrites detach from the substrate, or from one another, and then deposition transitions to base-controlled growth [29, 36]. On the other hand, clear experimental evidence of Li deposition occurring in $LiPF_6$–EC/DMC and resulting in "mossy" dendrite growth was provided by Steiger et al. [84] where the authors documented mechanisms for lithium deposition away from the base and dendrite tips. Given these different observations, in our investigation we consider different ways of macroscopically accounting for the effect of lithium deposition in a modified Planck-Nernst model and demonstrate using inverse modelling that one of the proposed approaches does lead to physically consistent reconstructions of the material properties and to accurate predictions of the evolution of the concentration profiles in time.

In this study, we consider a standard electrolyte, Lithium Hexafluro Phosphate $LiPF_6$, dissolved in 1:1 mixture of Ethylene Carbonate (EC) and Di-Methyl Carbonate (DMC), which is often used in batteries with additives. Determination of the material properties, diffusivity and the transference number, of this electrolyte, has been the subject of many investigations [1, 35, 38, 39] and the results are compiled in Figures 6.2 in the case of constant material properties and in Figures 6.3(a) and 6.3(b) when the material properties depend on concentrations (numerical values of these material properties are also tabulated in Appendix B1). This data will help us verify that

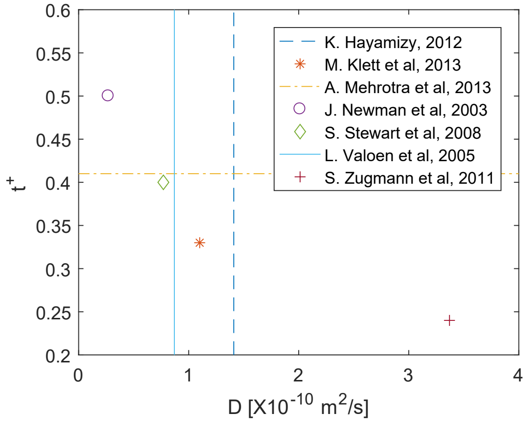

Figure 6.2: Values of the constant diffusion coefficient D and the transference number t^+ reported in the literature for LiPF$_6$–EC/DMC [35, 38, 49, 56, 85, 92, 100]. When the values of both D and t^+ are reported, they are represented with a symbol, whereas if the value of D or t^+ is reported only, it is represented with a vertical or a horizontal line.

the results obtained with inverse modelling and the Planck-Nernst model modified to account for the dendritic growth do indeed fall in the correct range. Finally, we will use the recently developed tools of Bayesian inference [78] to blend the results from the literature together with our experimental data and the assumed mathematical model to quantify the uncertainty of the reconstructed material properties.

The structure of the chapter is as follows: in the next section we describe our experimental set-up, whereas the Planck-Nernst model (2.12) is modified to account for the dendrite growth is introduced in Section 6.3; our computational approach is then described in Section 6.4 and the main results are presented in Section 6.5; discussion and final conclusions are deferred to Section 6.6, whereas some additional data and more technical material is collected in two appendices.

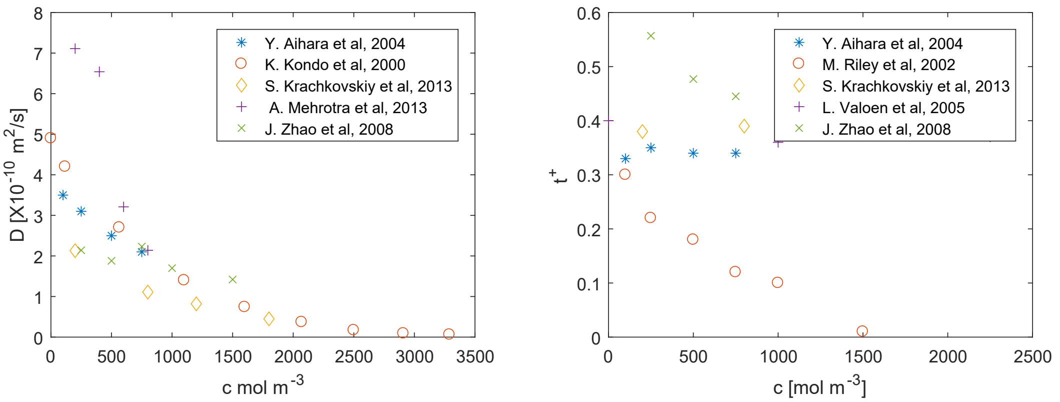

(a) (b)

Figure 6.3: (a) Dependence of the diffusion coefficient $D(c)$ on the concentration c reported in the literature for LiPF$_6$–EC/DMC [1, 39, 41, 49, 98]. (b) Dependence of the transference number $t^+(c)$ on the concentration c reported in the literature for LiPF$_6$–EC/DMC [1, 70, 41, 92, 98].

6.2 Experimental

Here we recall the experiment described in Section 2.1.2 where NMR concentration profiles are obtained in 2-hour intervals for the total of 14 hours for the standard electrolyte of LiPF$_6$ in EC/DMC. The growth of the dendritic region is modelled based on a separate experiment designed to probe how this region expands with time, cf. figure 6.1(b), depending on the applied current I. These results are presented in Figure 6.5 where we show the position $l(t)$ of the left boundary of the dendritic region as function of time t. As is evident from this data, there is an approximately linear dependence of $l(t)$ on time with the magnitude of the proportionality constant (corresponding to the slope the linear fits to the data in Figure 6.5) increasing with the applied current. This observation together with the data from Figure 6.4 allows us to quantify the growth of the dendritic region $[l(t), L]$, which is used to develop a modified Planck-Nernst model in the next section.

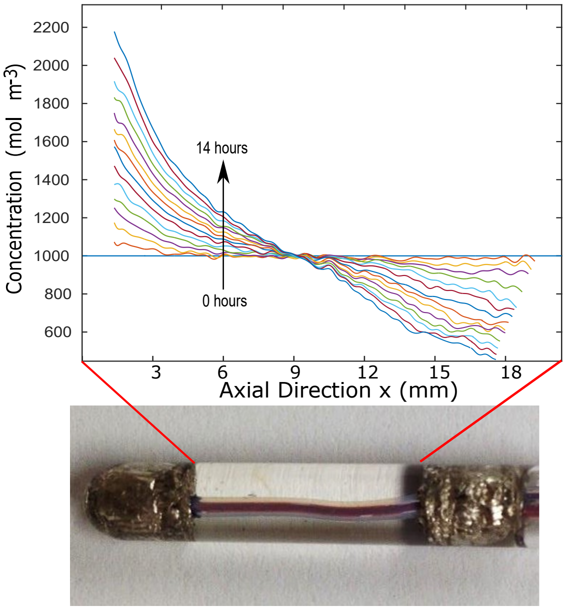

Figure 6.4: Concentration profiles obtained via in-situ magnetic resonance imaging during a galvanostatic polarization experiment. The shrinking of the region where the concentration profiles are acquired with time is evident near the negative (right) electrode.

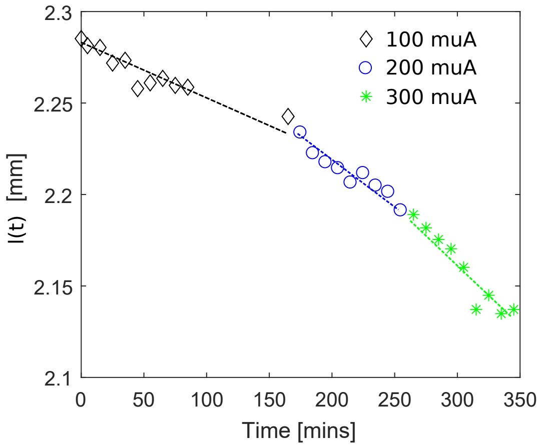

Figure 6.5: Dependence of the location $l(t)$ of the left boundary of the dendritic region, cf. figure 6.1(b), on time t for different applied currents I.

6.3 The Planck-Nernst Model with Dendrite Growth

Based on the observations made in Section 6.2 about the growth of the dendritic region, we now propose a modification of the Planck-Nernst model (2.12) that will account for this phenomenon. We emphasize that this is a highly idealized model which aims only to describe the depletion of lithium from the electrolyte in the dendritic region without attempting to provide any information about the structure of this region. In formulating this modified model we retain assumptions A1–A6 from Section 6.1, replace assumption A7 with a new assumption A8' given below and add the following assumptions A8–A10

A7': cations strip from the positive electrode (at $x = 0$) uniformly in the transverse direction and their flux corresponds to the applied electric current [59, 55];

A8: cations deposit onto the negative electrode non-uniformly in space forming dendrites that grow into the electrolyte at a rate proportional to the applied current [95]; the domain occupied by the dendrites is $[l(t), L]$, cf. Figure 6.1(b), where $l(t)$ is a known decreasing function of time such that $l(0) = L$, cf. Figure 6.5;

A9: Throughout the experiment the dendrites occupy a negligible fraction of the volume of the electrolyte such that the porosity of this region need not be taken into account;

A10: The loss of cations from the electrolyte due to their deposition on the dendrites is modeled by a sink term with a prescribed spatial distribution $\mathcal{F}_{l(t)}(x)$; this distribution function vanishes outside the dendritic region $[l(t), L]$.

With these additional assumptions, our model now takes the form

$$\begin{aligned}
\frac{\partial c}{\partial t} &= \frac{\partial}{\partial x}\left[D\frac{\partial c}{\partial x} + \frac{(1-t^{+})\,I}{FA}\right] - \frac{(1-t^{+})\,I}{FA}\mathcal{F}_{l(t)}(x) && \text{in } (0,L)\times(0,T], && (6.1\text{a})\\
\left.\frac{\partial c}{\partial x}\right|_{x=0} &= -\frac{(1-t^{+})\,I}{DFA} && \text{in } (0,T], && (6.1\text{b})\\
\left.\frac{\partial c}{\partial x}\right|_{x=L} &= 0 && \text{in } (0,T], && (6.1\text{c})\\
c\big|_{t=0} &= c_i && \text{in } (0,L), && (6.1\text{d})
\end{aligned}$$

where $l(t) = L - kIt$ with a certain constant $k > 0$, which is justified by the data presented in Figure 6.5. We note that the value of the constant k, which describes how rapidly the dendritic region $[l(t), L]$ spreads into the bulk of the electrolyte, can be deduced from the concentration measurements shown in Figure 6.4 by assessing the width $L - l(T)$ of the dendritic region at the end of the experiment. The key difference between the standard Planck-Nernst model (2.12) and its modified version (6.1) is the presence of the sink term proportional to the function $\mathcal{F}_{l(t)}(x)$ which describes how lithium from the electrolyte is lost due to its deposition within the growing dendritic region $[l(t), L]$. While this process can be described in various ways, the proposed model (6.1a) arguably combines simplicity with flexibility inherent in different possible forms of the function $\mathcal{F}_{l(t)}(x)$, which we will refer to as the "sink function". Given the different lithium deposition scenarios evidenced in the experimental studies discussed in Introduction, we will consider the following three distinct forms of "sink function":

case A: the loss of lithium occurs only at the interface $x = l(t)$ between the bulk of the electrolyte and the dendritic region, i.e.,

$$\mathcal{F}_{l(t)}(x) = \delta(l(t) - x), \tag{6.2}$$

where $\delta(\cdot)$ is the Dirac distribution; this corresponds to deposition occurring at the tips of the growing dendrites only,

case B: the rate of lithium loss decreases linearly from its maximum at the moving interface ($x = l(t)$) to zero at the electrode ($x = L$), i.e.,

$$\mathcal{F}_{l(t)}(x) = \begin{cases} \frac{2(L-x)}{(L-l(t))^2} & l(t) \leq x \leq L \\ 0 & \text{otherwise} \end{cases}, \tag{6.3}$$

case C: the loss of lithium occurs uniformly between the moving interface at $x = l(t)$ and the electrode at $x = L$, i.e.,

$$\mathcal{F}_{l(t)}(x) = \begin{cases} \frac{1}{L-l(t)} & l(t) \leq x \leq L \\ 0 & \text{otherwise} \end{cases}. \tag{6.4}$$

We note that cases A, B and C correspond to the rate of the loss of lithium being progressively less localized near the tips of the dendrites at $x = l(t)$, and in all cases the sink function is normalized such that $\int_{l(t)}^{L} \mathcal{F}_{l(t)}(x')\, dx' = 1$.

6.4 Computational Approaches to Inverse Modelling and Uncertainty Quantification

In this section, we provide an overview of the computational approaches employed to solve the inverse-modelling problem for both constant and concentration-dependent material properties and assess their uncertainty. Further details are provided in Appendices B.

6.4.1 Inverse Modelling

The unknown material properties, D and t^+, can be reconstructed based on the assumed transport model, such as system (2.12) or (6.1), and using the concentration profiles obtained in the NMR experiment described in Section 6.2. We will use the inverse modelling approach developed and validated in Chapter 3 in which the problem is framed as minimization of a cost functional representing the least-squares deviation between the concentration values predicted by the model (denoted c in systems (2.12) and (6.1)) and the experimentally determined concentration values $\tilde{c}$. The cost functional can thus be represented as

$$\mathcal{J}([D,t^+]) = \frac{1}{2}\sum_{i=1}^{N_T}\int_0^L \left[c(x,t_i;D,t^+) - \tilde{c}(x,t_i)\right]^2 \, dx, \tag{6.5}$$

where t_i, $i = 1,\dots,N_T$, are the time levels when the experimental

6.2).

We will consider two distinct formulations corresponding, respectively, to constant and to concentration-dependent material properties.

$$\text{P1}: \qquad [\widehat{D}, \widehat{t^+}] = \underset{[t^+, D] \in \mathbb{R}^2}{\operatorname{argmin}} \mathcal{J}(D, t^+)$$

$$\text{P2}: \qquad [\widehat{D}(c), \widehat{t^+}(c)] = \underset{[t^+(c),\, D(c)] \in \mathcal{X}}{\operatorname{argmin}} \mathcal{J}\left(D(c), t^+(c)\right),$$

where $\mathcal{X}$ denotes a suitable function space to which $D(c)$ and $t^+(c)$ belong. The computational approach required to solve the problem P2 with concentration-dependent material properties is more involved and necessitates specialized tools described in detail in Chapter 3.

6.4.2 Bayesian Uncertainty Quantification

In order to quantify the uncertainty arising in estimation due to, e.g., modelling and measurement errors, we use a state-of-the-art technique based on Bayesian inference [78] as described in Chapter 4. In this approach a probabilistic setting is adopted as a way to quantify uncertainty resulting from incomplete knowledge about the problem. Here we will represent the reconstructed material properties $[D, t^+]$, or $[D(c), t^+(c)]$, in terms of random variables characterized by certain probability density functions (PDFs). More precisely, in the case of concentration-dependent properties, $D(c)$ and $t^+(c)$ are given by suitable probability distributions for *all* concentration values $c \in [c_\alpha, c_\beta]$ and the same also applies to the measurements $\tilde{c}$ for different values of $x \in [0, L]$ and $t \in [0, T]$.

In the Bayesian framework the probability distribution of the reconstructed material properties are given in terms of the *posterior* probability $\mathbb{P}([D, t^+]|\tilde{c})$, which is the probability of $[D, t^+]$ attaining certain values (in problem P2, for a given concentration c) given the entire set of observations $\tilde{c}$, and can be expressed using Bayes' rule [86, 81, 91]

$$\mathbb{P}([D, t^+]|\tilde{c}) = \frac{\mathbb{P}(\tilde{c}|[D, t^+])\, \mathbb{P}([D, t^+])}{\mathbb{P}(\tilde{c})}, \tag{6.6}$$

where $\mathbb{P}([D, t^+])$ is the *prior* distribution reflecting our a priori assumptions about the solution, $\mathbb{P}(\tilde{c}|m)$ is the *likelihood* of observing particular experimental data for a given set of material properties and $\mathbb{P}(\tilde{c})$ is a normalizing factor.

In the present study the prior $\mathbb{P}([D, t^+])$ is constructed using the data reported in the literature for the diffusivity and the transference numbers for the electrolyte considered here, cf. Figures 6.2 and 6.3 as well as Appendix B1, and is shown in Figure 6.6. Details concerning the computation of such a prior is provided in Appendix B2. Priors defined in this way can be "weak" or "strong" [43], depending on their relative deviation from the uniform distribution which is also reflected in the width of the range $[\min_{D,t^+} \mathbb{P}([D, t^+]), \max_{D,t^+} \mathbb{P}([D, t^+])]$. Given the differences in experimental conditions resulting in various possible interpretations of the data from the literature, the prior adopted in the present study is "weak", cf. Figure 6.6, such that it will not dominate the posterior probability given in (6.6).

As regards the likelihood function, the following relation is typically adopted in Bayesian inference [86, 81, 91]

$$\mathbb{P}(\tilde{c}|[D, t^+]) \propto e^{-\mathcal{J}(D,t^+)}, \tag{6.7}$$

which expresses the assumption that for a given set of material properties $[D, t^+]$, measurements resulting in large values of the error functional (6.5) are less likely to

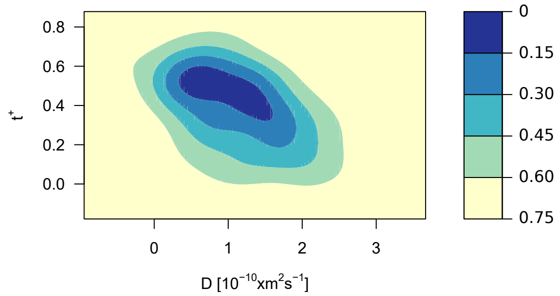

Figure 6.6: The "weak" prior $\mathbb{P}([D,t^+])$ constructed as described in Appendix B2 based on the literature data for diffusivity and the transference numbers, cf. Figures 6.2 and 6.3. Since in the calculation of the posterior suitable normalization is ensured by the expression in the denominator in (6.6), for simplicity, the prior shown here has an arbitrary scaling.

be observed. An intuitive motivation for the choice of an exponential function in (6.7) is that when $\mathcal{J}([D,t^+])$ is quadratic in $[D,t^+]$, relation (6.7) produces a normal distribution. A more rigorous justification of this choice can be found for example in [86]. The likelihood function $\mathbb{P}(\tilde{c}|[D,t^+])$ is approximated by sampling the distribution in (6.7) using the Metropolis-Hastings algorithm [16] to produce M samples. Details concerning the computational algorithm are provided in Appendix B2.

Thus, the Bayesian representation of the uncertainty (6.6) combines the knowledge about the material properties already available in the literature as the prior $\mathbb{P}([D,t^+])$, cf. Figure 6.6, with a measure of uncertainty based on how well model (6.1) fits the data which is represented by the likelihood function $\mathbb{P}(\tilde{c}|[D,t^+])$. Since a weak prior is used, the posterior distribution $\mathbb{P}([D,t^+]|\tilde{c})$ will be in the favor of the likelihood function. This approach to uncertainty quantification in electrochemical systems was developed and thoroughly validated in [78].

6.5 Results

In this section, we present and analyze the reconstructions of the material properties obtained using the inverse-modelling approach of Section 6.4.1 based on the standard and modified Planck-Nernst models (2.12) and (6.1). The uncertainty of the obtained estimates are quantified with the Bayesian approach described in Section 6.4.2. First, we focus on inferring constant material properties, cf. problem P1, and then consider reconstruction of concentration-dependent material properties by solving problem P2 for the most accurate variant of the modified model (6.1).

We begin the presentation of our results by showing the optimal reconstructions $\widehat{D}$ and $\widehat{t}^+$ of the constant material properties based on the standard Planck-Nernst model (2.12) and the modified model (6.1) with three different forms (6.2)–(6.4) of the sink function $\mathcal{F}_{l(t)}(x)$ in Figure 6.7. The reconstructions are obtained by solving optimization problem P1 and the corresponding values of the error functional (6.5) are given in Table 6.1, whereas Figure 6.7 also contains information about the relative uncertainty of the reconstructions determined as discussed in Section 6.4.2, i.e. for each panel of Figure 6.7 the solid lines represent the optimal reconstructions $[\widehat{D}, \widehat{t}^+]$ obtained by solving problem P1 whereas the color contours represent the corresponding posterior probability distributions (6.6). The data shown in Figure 6.7(a) for the standard Planck-Nernst model (2.12) confirms the observations already made in Chapter 5, namely, that the inverse modelling leads to a negative transference number $\widehat{t}^+ < 0$ obtained via inverse modelling, which is physically inconsistent and hence calls into question the validity of the standard Planck-Nernst system (2.12) as a model for the data described in Section 6.2. This issue is only partially remedied, in the sense that the obtained values of $\widehat{t}^+$ become less negative, when the reconstructions are performed based on the modified model (6.1) with the sink function $\mathcal{F}_{l(t)}(x)$ defined in (6.2) and (6.3), cf. Figures 6.7(b) and 6.7(c). We note that in all these cases the maximum of the posterior probability distribution $\mathbb{P}([D, t^{+}]|\tilde{c})$ corresponds to positive transference number t^{+}, which is due to the prior obtained based on positive transference numbers only, cf. Figure 6.6. On the other hand, in Figure 6.7(d) we observe that the reconstructed transference number $\widehat{t}^{+}$ obtained based on the modified Planck-Nernst model (6.1) with a constant sink function (6.4) is positive. In this case the optimal reconstructions $[\widehat{D}, \widehat{t}^{+}]$ are also near the values of $[D, t^{+}]$ maximizing the posterior probability distribution $\mathbb{P}([D, t^{+}]|\tilde{c})$, indicating that the reconstructions $[\widehat{D}, \widehat{t}^{+}]$ are now closer to the literature data. Moreover, since the posterior probability distribution in Figure 6.7(d) is more isotropic than in the previous cases, this implies a weaker correlation between the uncertainties of D and t^{+}. By comparing the results shown in Figures 6.7(a)–(d) we note that the main improvement, both in terms of the reconstructed values and their uncertainties, results from replacing models with a localized depletion of lithium (i.e., the standard Planck-Nernst model with the boundary condition (4.1b) and the modified Planck-Nernst model (6.1) with the sink function given in case A) with models in which this depletion is distributed in space (the modified Planck-Nernst model (6.1) with the sink functions given in cases B and C). In order to elucidate how the structure of the sink function affects the reconstruction of the transference number t^{+}, we have solved problem P1 using a family of sink function constructed such that the constant "slope" $s = \frac{d}{dx}\mathcal{F}_{l(t)}(x)$, $x \in [l(t), L]$, was allowed to vary continuously from $-\infty$ to $+\infty$ while satisfying the constraint $\int_{l(t)}^{L} \mathcal{F}_{l(t)}(x')\, dx' = 1$. Thus, the standard Planck-Nernst model (2.12) and variants A–C of the modified model (6.1), cf. (6.2)–(6.4), can be viewed as special cases of this more general family, see Figure 6.8(a). As is evident from the data shown in Figure 6.8(b), within this family of sink functions, case C corresponds in fact to the maximum value of the reconstructed transference number $\widehat{t^+}$.

Planck-Nernst Model	Sink Function $\mathcal{F}_{l(t)}(x)$	Inverse Problem	$\mathcal{J}([\widehat{D},\widehat{t^+}])$
standard, Eq. (2.12)	—	P1	2.61
modified, Eq. (6.1)	case A, Eq. (6.2)	P1	2.26
modified, Eq. (6.1)	case B, Eq. (6.3)	P1	2.12
modified, Eq. (6.1)	case C, Eq. (6.4)	P1	2.21
modified, Eq. (6.1)	case C, Eq. (6.4)	P2	1.14

Table 6.1: Final values of the error functional $\mathcal{J}([\widehat{D},\widehat{t^+}])$ obtained in the different cases considered.

The experimental concentration profiles $\tilde{c}(x,t_i)$, cf. Figure 6.4, are compared to the concentration profiles $c(x,t_i)$ predicted by the standard Planck-Nernst model (2.12) and the modified model (6.1) with a constant sink function (6.4) using their respective optimal material properties $[\widehat{D},\widehat{t^+}]$ in Figures 6.9 and 6.10, respectively. The main difference between these two cases is that in the former the concentration profiles $c(x,t_i)$ predicted by the model exhibit large deviations from the measured profiles $\tilde{c}(x,t_i)$ close to the right electrode, which is where the dendritic regions appears. The quality of fits in this region is noticeably improved when the modified Planck-Nernst model (6.1) is used, arguably due to a suitable choice of the sink function $\mathcal{F}_{l(t)}(x)$, cf. (6.4). This improvement is also reflected in the difference of the values of the error functional (6.5) obtained in the two cases, cf. Table 6.1. As deposition of lithium continues, a porous structure with a certain porosity $\phi(x,t)$ depending on

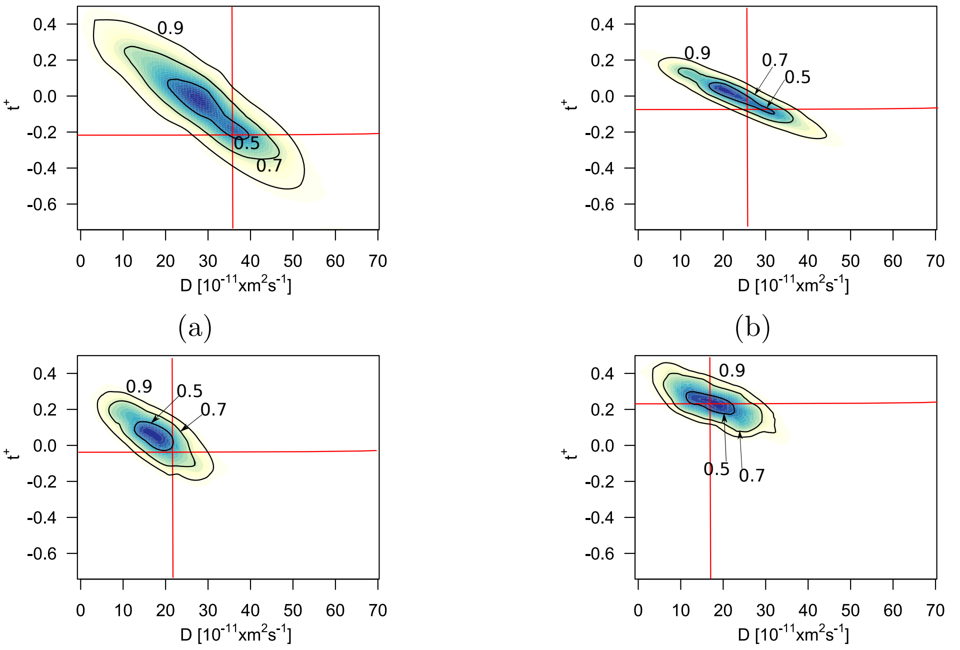

(a) (b)

(c) (d)

Figure 6.7: (red solid lines) Reconstructions of constant material properties $[\widehat{D}, \widehat{t^+}]$ using (a) the standard Planck-Nernst model (2.12), (b) modified model (6.1) with sink function (6.2) (case A), (c) modified model (6.1) with sink function (6.3) (case B), and (d) modified model (6.1) with sink function (6.4) (case C). The associated posterior probability distributions are indicted with filled contours. The contour lines indicate the boundaries of the credibility region with the corresponding credibility values indicated next to the contour lines. Information about the values of the material properties reported in the literature, cf. Figure 6.2, is contained in the posterior probability distribution through the choice of the prior, cf. relation (6.6) and Figure 6.6.

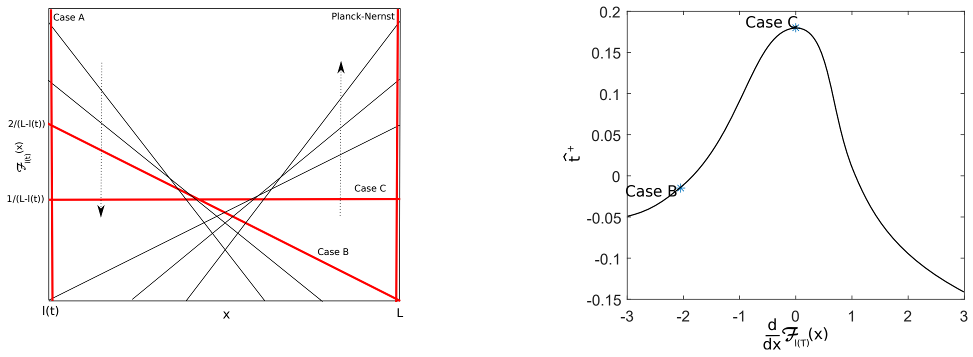

(a) (b)

Figure 6.8: (a) Sink functions with different slopes $s = \frac{d}{dx}\mathcal{F}_{l(t)}(x)$, $x \in [l(t), L]$, varying continuously from $-\infty$ to $+\infty$ (the vertical arrows indicate the trends with the increase of s whereas the thick red lines represent the standard Planck-Nernst model (2.12) and the different variants of the modified model (6.1) arising as special cases for particular values of s); (b) transference numbers $\widehat{t^+}$ inferred by solving problem P1 as function of the slope s characterizing the sink function $\mathcal{F}_{l(t)}(x)$, cf. panel (a).

both space and time is formed in the dendritic region $[l(t), L]$. The corresponding volume fractions $1 - \phi(x,t)$ occupied by lithium dendrites predicted by the modified Planck-Nernst model (6.1) with a constant sink function (6.4) are shown in Figure 6.11 for as functions of $x \in [l(T), L]$ for different times spread uniformly between 0 and T. This data illustrates how the dendritic region progressively spreads into the bulk of the electrolyte. Another interpretation is that if one assumed that all lithium is deposited on a *single* dendrite, then the curves shown in Figure 6.11 would describe its time-evolving shape. The average porosity of the dendritic region at the end of the experiment is $[\int_{l(T)}^{L} \phi(x,T)\, dx]/[L - l(T)] = 0.9675$.

Since it gives the best results, we now focus on the modified Planck-Nernst model (6.1) with a constant sink function (6.4) and consider reconstruction of concentration-dependent material properties, cf. problem P2. The optimal reconstructions $\widehat{D}(c)$ and $\widehat{t^+}(c)$ are shown as functions of the concentration c in Figures 6.12(a) and 6.12(b), respectively, together with the associated posterior probability distributions. As is evident from these figures, the obtained optimal reconstructions $\widehat{D}(c)$ and $\widehat{t}^{+}(c)$ are consistent, both in terms of values attained and the dependence on c, with the literature data summarized in Figures 6.3(a) and 6.3(b), although the literature data for the transference numbers exhibits a significant scatter for all values of c. We note that the uncertainty of $\widehat{D}(c)$ and $\widehat{t}^{+}(c)$, given by the posterior probability distribution at the given value of c, is rather modest and significantly smaller than the entire range of variation of $\widehat{D}(c)$ and $\widehat{t}^{+}(c)$ for $c \in [200, 2000]$. This uncertainty is also essentially independent of the concentration c. Finally, in Figure 6.13 we compare the corresponding concentration profiles $c(x, t_i)$ with the experimental profiles $\tilde{c}(x, t_i)$. As is evident from the comparison of this figure with Figure 6.10, there is a further improvement in the quality of the fits, which is also reflected in an additional decrease of the value of the error function (6.5), cf. Table 6.1.

6.6 Conclusions

In this section, we briefly summarize our findings from Section 6.5. As is evident from Figure 6.7(d), the modified Planck-Nernst model (6.1) with a constant sink function (6.4) leads to the most consistent reconstruction of the material properties, since in all other cases, including the standard Planck-Nernst model (2.12), the inferred transference numbers $\widehat{t}^{+}$ are negative, cf. Figures 6.7(a)–(c). This demonstrates that the constant sink function (6.4), describing a uniform in space depletion of lithium, offers a satisfactory account of the effect of the formation of the dendritic region on the transport processes in the electrolyte (we have also considered forms of the sink function $\mathcal{F}_{l(t)}(x)$ other than given in (6.2)–(6.3), but the results were inferior with respect to those obtained with (6.4)). This conclusion is reinforced by the improved quality of the concentration fits near the right electrode obtained with the modified model (6.1) as compared to the fits obtained with the standard model (2.12), cf. Figure 6.9 versus Figure 6.10. The fact that the modified model (6.1) reproduces the experimental measurements most accurately when it is combined with a constant sink function (6.4) allows us to speculate that lithium is deposited not only on the tips of the dendrites, but also within the entire dendritic region (for example, in the form of new dendrites growing from the negative electrode or sideways off the existing dendrites). Modelling this process based on first principles remains a challenging open problem [95].

The reconstructions obtained based on the modified model (6.1) with the constant sink function (6.4) are characterized by the smallest uncertainty with the weakest degree of correlation between the uncertainties of D and t^+. Finally, we also note that the concentration-dependent diffusivity $\widehat{D}(c)$ reconstructed by solving problem P2 agrees well with the literature data, both in terms of the values and the dependence on c, cf. Figures 6.3(a) and 6.12(a). As regards the concentration-dependent transference numbers, the obtained reconstruction $\widehat{t^+}(c)$ corresponds to the lower end of the range of values reported in the literature, cf. Figures 6.3(b) and 6.12(b). Concerning the dependence on the concentration, the decrease of the optimally reconstructed material property $\widehat{t^+}(c)$ with c is consistent with the trends evident in most, albeit not in all, data-sets from the literature.

To conclude, we have developed and validated a novel model for the transport of charged species in electrolytes in the presence of dendritic growth. We also add that the present study represents an innovative application of the concepts of inverse modelling and uncertainty quantification to validate or invalidate different models of complex transport phenomena.

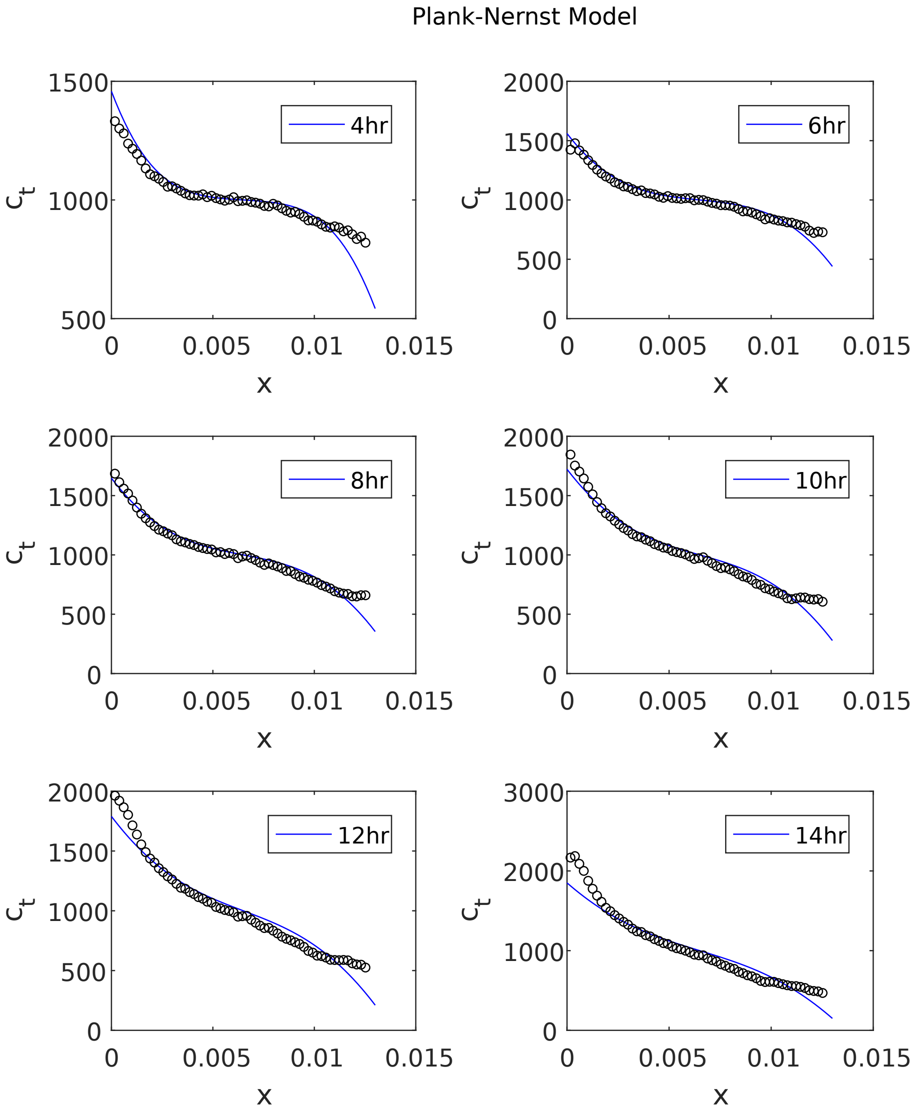

Figure 6.9: Experimental concentration profiles $\tilde{c}(x, t_i)$ (symbols) and the concentration profiles predicted by the standard Planck-Nernst model (2.12) using the optimal constant material properties $[\widehat{D}, \widehat{t^+}]$ (solid lines) at different time levels $t_i = 4, 6, 8, 10, 12, 14$ hours. The size of the symbols (circles) indicates the error in the experimental data

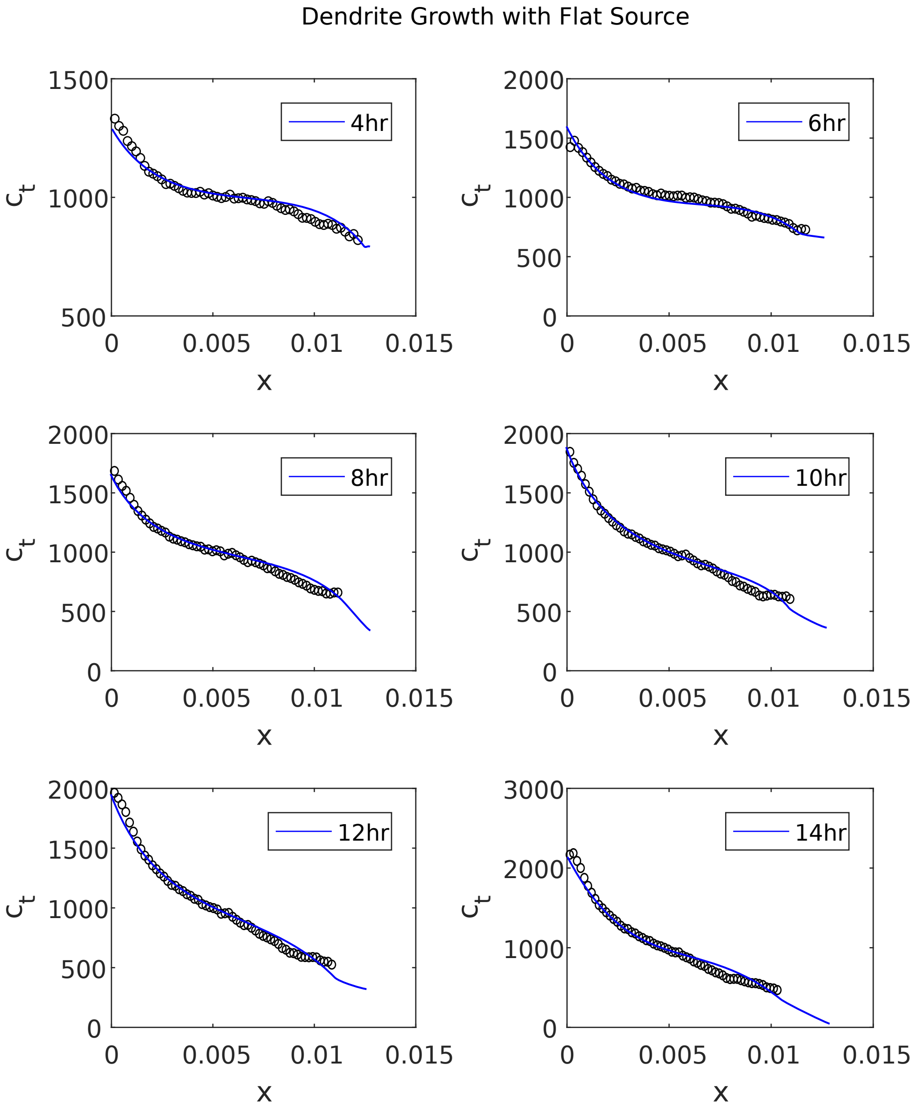

Figure 6.10: Experimental concentration profiles $\tilde{c}(x, t_i)$ (symbols) and the concentration profiles predicted by the modified Planck-Nernst model (6.1) with a constant sink function (6.4) and using the optimal constant material properties $[\widehat{D}, \widehat{t}^{+}]$ (solid lines) at different time levels $t_i = 4, 6, 8, 10, 12, 14$ hours. The size of the symbols (circles) indicates the error in the experimental data

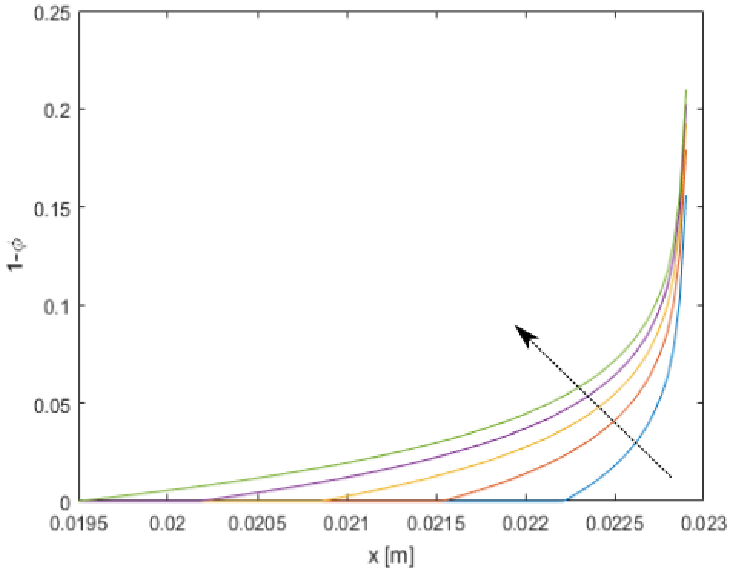

Figure 6.11: The volume fractions $1-\phi(x,t)$ occupied by lithium dendrites predicted by the modified Planck-Nernst model (6.1) with a constant sink function (6.4) as functions of $x \in [l(T), L]$ for different times spread uniformly between 0 and T (the arrow indicates the trend with the increase of time t).

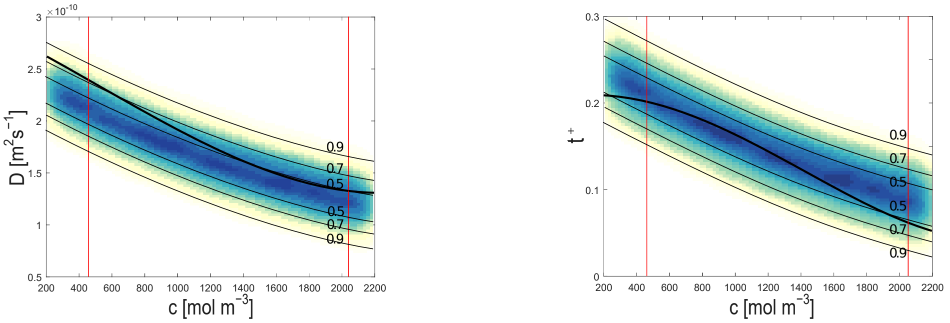

(a) (b)

Figure 6.12: Reconstruction of concentration-dependent (a) diffusivity $\widehat{D}(c)$ and (b) transference number $\widehat{t^+}(c)$ (black solid lines) together with the associated posterior probability distributions (filled contours) as functions of the concentration c for the modified Planck-Nernst model (6.1) with the constant sink function (6.4), case C. The contour lines indicate the boundaries of the credibility region with the corresponding credibility values indicated next to the contour lines. Information about the values of the material properties reported in the literature, cf. Figure 6.3, is contained in the posterior probability distribution through the choice of the prior, cf. relation (6.6) and Figure 6.6.

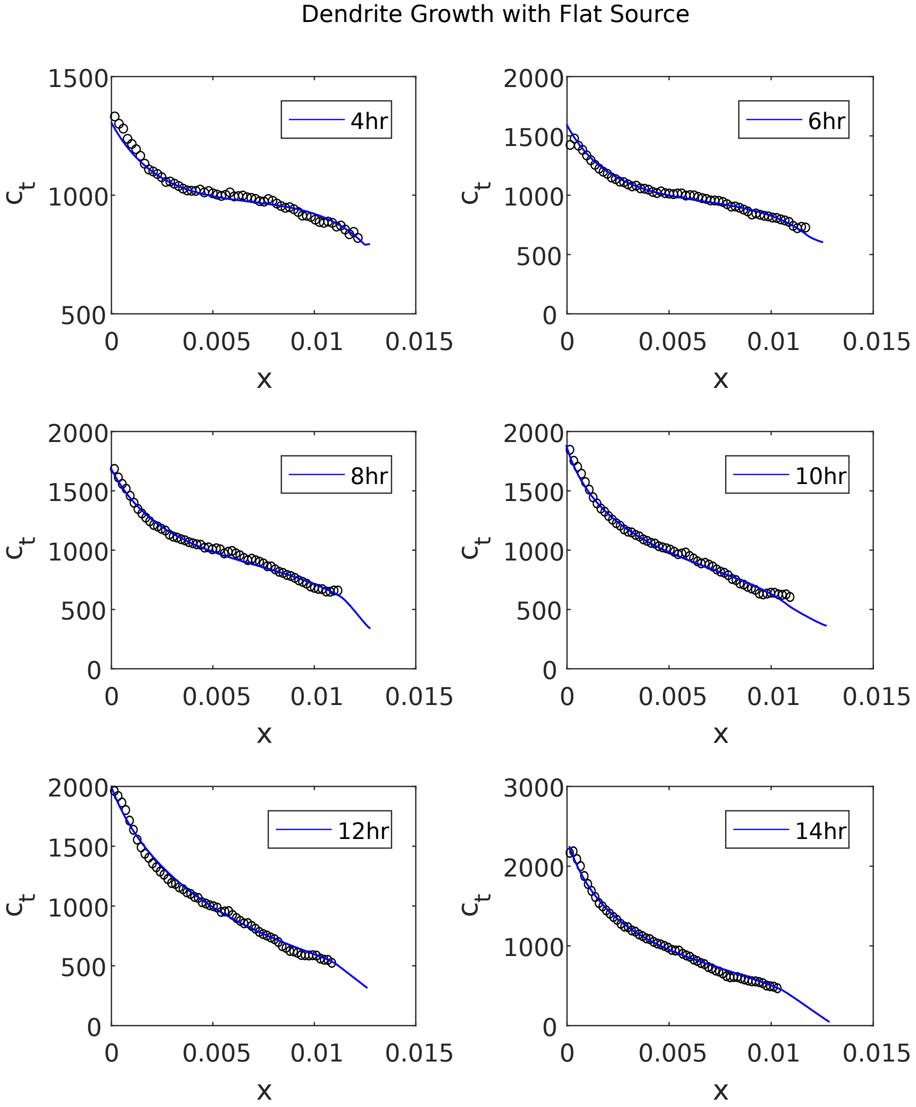

Figure 6.13: Experimental concentration profiles $\tilde{c}(x, t_i)$ (symbols) and the concentration profiles predicted by the modified Planck-Nernst model (6.1) with a constant sink function (6.4), case C, and using the optimal concentration-dependent material properties $[\widehat{D}(c), \widehat{t^+}(c)]$ (solid lines) obtained as a solution for problem P2 at different time levels $t_i = 4, 6, 8, 10, 12, 14$ hours. The size of the symbols (circles) indicates the error in the experimental data

Chapter 7

Summary, Conclusion and Outlook

In this study, multiple models for material transport in electrolyte were considered based on the Planck-Nernst theory. Algorithms were developed to obtain the concentration-dependent material properties and estimate the uncertainty associated with them. This approach was tested and validated at various levels and then used to infer the concentration-dependence of material properties of lab-made and commercial Li-ion battery electrolytes. Important aspects of this thesis are summarized as follows:

- State-of-the-art computational framework for reconstructing the material properties from experimental data has been developed based on adjoint analysis and optimization techniques. An additional framework to estimate uncertainty based on Bayesian statistics has been developed, validated and implemented to understand how sensitive our estimates of material properties deduced using inverse modelling are with respect to various sources of uncertainty. These computational tools have allowed us to draw novel conclusions about the validity of the Planck-Nernst model and its various modifications.

- Ion-pairing phenomena have no effect on our inverse-modelling estimates and therefore the non-physical values obtained for the transference number are likely not due to these ion-pairing effects as speculated in some electrochemistry literature.
- Dendrite growth plays an important role in ion transport in the electrolyte and this phenomenon has a significant effect on our estimates of material properties. Based on our analysis with inverse modelling and uncertainty quantification, we can conjecture that uniform deposition of Li can be a possible reason for the appearance of the negative transference number.

By addressing the above-mentioned problem, the present investigation helps to make modelling Li-ion batteries more accurate and reliable.

Appendix A

Ion-Pairing Effects

A1 The Total Lithium Flux in the Bulk

In this appendix we give the details behind the modification to the Nernst-Planck equations accounting for ion pairing. We begin by stating expressions for the fluxes of positive ions $\mathcal{F}_+$, negative ions $\mathcal{F}_-$ and ion pairs $\mathcal{F}_o$ using the Maxwell-Stefan diffusion formalism which is applicable to moderately concentrated electrolytes [52]

$$\mathcal{F}_+ = -\frac{D_+ c_+}{RT}\frac{\partial \mu_+}{\partial x}, \qquad \mu_+ = \mu_+^\Phi + RT\log a_+ + F\phi, \tag{A.1a}$$

$$\mathcal{F}_- = -\frac{D_- c_-}{RT}\frac{\partial \mu_-}{\partial x}, \qquad \mu_- = \mu_-^\Phi + RT\log a_- - F\phi, \tag{A.1b}$$

$$\mathcal{F}_o = -\frac{D_o c_o}{RT}\frac{\partial \mu_o}{\partial x}, \qquad \mu_o = \mu_o^\Phi + RT\log a_o, \tag{A.1c}$$

where D_k, μ_k^Φ and μ_k, and a_k are, respectively, the diffusion coefficient, the reference and total electrochemical potential and activity of the kth species (for $k = +, -, o$), whereas ϕ is the electric potential. Within the electrolyte and away from the double layers at the electrode there is almost exact charge electroneutrality, *i.e.* $c_+ = c_-$.

This allows us to write

$$c_+ = c, \qquad \text{and} \qquad c_- = c. \tag{A.2}$$

Substituting these electroneutrality relations into equations (2.3a)–(2.3b) and subtracting these two equations gives the following relation for current conservation

$$\frac{\partial j}{\partial x} = 0, \qquad \text{where} \qquad j = F(\mathcal{F}_+ - \mathcal{F}_-), \tag{A.3}$$

in which j is the current density. On substituting for $\mathcal{F}_+$ and $\mathcal{F}_-$ from (A.1a)–(A.1b), the expression for j may also be written as

$$j = -\frac{Fc}{RT}\left(D_+\frac{\partial \mu_+}{\partial x} - D_-\frac{\partial \mu_-}{\partial x}\right). \tag{A.4}$$

At this stage it is convenient to introduce the electrolyte chemical potential μ_e defined as

$$\mu_e = \frac{\mu_+ + \mu_-}{2}, \tag{A.5}$$

which has the property that it is independent of the electric potential, since by using the definitions of the electrochemical potentials found in (A.1a)–(A.1b) and (A.5) we see that

$$\mu_e = \mu_e^{\Phi} + RT\log(a_e(c)), \quad \text{where} \quad a_e(c) = [a_+(c)a_-(c)]^{1/2} \quad \text{and} \quad \mu_e^{\Phi} = \frac{\mu_+^{\Phi} + \mu_-^{\Phi}}{2}. \tag{A.6}$$

Where the dimerization reaction $\mathrm{Li}^+ + \mathrm{A}^- \rightleftharpoons \mathrm{LiA}$ is in quasi-equilibrium, the following relation between the chemical potentials is satisfied

$$\mu_+ + \mu_- = \mu_o \tag{A.7}$$

Table A1.1: Typical values of dimensional parameters.

Parameter	Symbol	Value	Units	Source
Debye Length	L_D	$O(10^{-9})$	m	[93]
Cell Length	L	$O(10^{-2})$	m	Experiment
Reaction Rate	k	$O(10^{9})$	$\frac{1}{s}$	[11]
Time of Experiment	τ	$O(10^{4})$	s	Experiment
Concentration	$\hat{c}$	10^{3}	$\frac{mol}{m^3}$	Experiment

which in turn implies that

$$a_o = K a_e^2, \quad \text{where} \quad K = \exp\left(\frac{2\mu_e^{\Phi} - \mu_o^{\Phi}}{RT}\right), \tag{A.8}$$

and since $a_e = a_e(c)$ and $a_o = a_o(c_o)$, this implies a functional relationship between c_o and c. Since we will be working with the "total concentration" $c_T = c_o + c$, as defined in (5.8), it is most helpful to express this in the functional form

$$c_o = f(c_T), \tag{A.9}$$

from which it follows that

$$c = c_T - f(c_T). \tag{A.10}$$

We now seek to express the ion fluxes, as defined in (A.1a)–(A.1b), solely in terms of the electrolyte chemical potential μ_e and the current density j. We do this (following [55]) by referring to relation (A.4) and recasting (A.1a)–(A.1b) in the following form

$$\begin{aligned}
\mathcal{F}_+ &= -\frac{c}{RT}\left[D_+\frac{\partial\mu_+}{\partial x} - \alpha\left(D_+\frac{\partial\mu_+}{\partial x} - D_-\frac{\partial\mu_-}{\partial x}\right)\right] + \alpha\frac{j}{F},\\
\mathcal{F}_- &= -\frac{c}{RT}\left[D_-\frac{\partial\mu_-}{\partial x} - \beta\left(D_+\frac{\partial\mu_+}{\partial x} - D_-\frac{\partial\mu_-}{\partial x}\right)\right] + \beta\frac{j}{F}
\end{aligned}$$

with an appropriate choice of α and β. In this instance, by taking $\alpha = t^+$ and $\beta = -(1-t^+)$, where the transference number t^+ is defined via

$$t^+ = \frac{D_+}{D_- + D_+}, \tag{A.11}$$

we obtain the desired expressions, namely,

$$\mathcal{F}_+ = -\frac{c}{RT}\frac{2D_+D_-}{D_+ + D_-}\frac{\partial\mu_e}{\partial x} + \frac{t^+ j}{F}, \tag{A.12a}$$

$$\mathcal{F}_- = -\frac{c}{RT}\frac{2D_+D_-}{D_+ + D_-}\frac{\partial\mu_e}{\partial x} - \frac{(1-t^+)j}{F}. \tag{A.12b}$$

Defining

$$\mathcal{D}^\dagger(c) = c\frac{2D_+D_-}{D_+ + D_-}\frac{\partial\mu_e}{\partial a_e}\frac{\partial a_e}{\partial c} = c\frac{2D_+D_-}{D_+ + D_-}\frac{RT}{a_e}\frac{\partial a_e}{\partial c},$$

where we used relation (A.6), we can rewrite the fluxes as

$$\mathcal{F}_+ = -\mathcal{D}^\dagger(c)\frac{\partial c}{\partial x} + \frac{t^+ j}{F}, \tag{A.13a}$$

$$\mathcal{F}_- = -\mathcal{D}^\dagger(c)\frac{\partial c}{\partial x} - \frac{(1-t^+)j}{F}. \tag{A.13b}$$

Similarly, defining $\mathcal{D}_o^\dagger(c_o) = c_o D_o \frac{\partial \mu_o}{\partial a_o}\frac{\partial a_o}{\partial c_o}$, we have

$$\mathcal{F}_o = -\mathcal{D}_o^\dagger(c_o)\frac{\partial c_o}{\partial x}. \tag{A.14}$$

Then, using the definition of the total lithium flux $\mathcal{F}_T$ found in (5.8) together with the relations (A.13a)–(A.13b) and (A.14), we obtain the following expression

$$\mathcal{F}_T = -\left(\mathcal{D}^\dagger(c)\frac{\partial c_T}{\partial x}\left(1 - \frac{df}{dc_T}\right) + \mathcal{D}_o^\dagger(c_o)\frac{df}{dc_T}\right)\frac{\partial c_T}{\partial x} - \frac{j}{2F}(1-2t^+), \tag{A.15}$$

where c_o and c are given by (A.9) and (A.10), respectively. It is straightforward to rewrite this expression in terms of an effective diffusivity, defined by

$$\widetilde{D}(c_T) = \mathcal{D}^\dagger(c) + \left(\mathcal{D}_o^\dagger(c_o) - \mathcal{D}^\dagger(c)\right)\frac{df(c_T)}{dc_T}, \tag{A.16}$$

so that it now reads

$$\mathcal{F}_T = -\widetilde{D}(c_T)\frac{\partial c_T}{\partial x} - \frac{j}{2F}(1-2t^+). \tag{A.17}$$

A2 Fluxes in the Reaction Layers

In this section we offer a systematic demonstration that the fluxes of the charged species do not vary appreciably across the narrow reaction layers in the vicinity of the interfaces using asymptotic methods. First, we cast the problem in non-dimensional form by scaling the dependent variables. Henceforth, quantities marked with a star are dimensionless. We write

$$c_i = \hat{c}\, c_i^*, \qquad Q = k\, \hat{c}\, Q^*, \qquad x = L\, x^*, \tag{A.18a}$$

$$\mathcal{F}_i = \frac{L\hat{c}}{\tau}\mathcal{F}_i^*, \qquad R_i = \frac{L\hat{c}}{\tau} R_i^*, \qquad t = \tau t^*, \tag{A.18b}$$

where $\hat{c}$ is a typical value of the ionic concentration, $\mathcal{F}_i$ is the flux of species $i = \{+, -, o\}$, τ is a characteristic timescale for the experiment, whereas k is a characteristic reaction rate. Typical values of some of these parameters are summarized in Table A1.1. On applying these scaling relations to equations (2.3) as well as (5.9) and its boundary conditions (5.10) we obtain

$$\frac{\partial c_+^*}{\partial t^*} + \frac{\partial \mathcal{F}_+^*}{\partial x^*} = -\frac{Q^*}{\delta}, \quad \frac{\partial c_-^*}{\partial t^*} + \frac{\partial \mathcal{F}_-^*}{\partial x^*} = -\frac{Q^*}{\delta}, \quad \frac{\partial c_o^*}{\partial t^*} + \frac{\partial \mathcal{F}_o^*}{\partial x^*} = \frac{Q^*}{\delta}, \tag{A.19a}$$

$$\frac{\partial c_T^*}{\partial t^*} + \frac{\partial \mathcal{F}_T^*}{\partial x^*} = 0, \quad \mathcal{F}_T^*|_{x=0} = \frac{J}{2}, \quad \mathcal{F}_T^*|_{x=1} = \frac{J}{2}, \tag{A.19b}$$

where

$$\delta = \frac{1}{\tau k} \ll 1, \qquad J = \frac{j}{F\mathcal{F}_i^*} = O(1). \tag{A.20}$$

Here δ is the ratio of the typical timescale of experiment to those for ion-pairing reactions while J is the ratio of the electronic current density supplied at the contact to the ionic current density in the solution.

The small value of δ (which can be estimated using the parameter values in Table A1.1) requires that the bulk of the electrolyte, where $x^* = O(1)$, be in quasi-equilibrium. Contrastingly, close to the edges of the domain near the electrodes, where either $x^* = O(\delta)$ or $1 - x^* = O(\delta)$, the reaction rate could be sufficiently large that it may appreciably alter the fluxes of some of the different species across these narrow layers. Examining (A.19a)–(A.19b) we see that the fluxes of anions, cations and neutral ion pairs are all altered, but, crucially, the flux of the total mount of Lithium is unaffected. To demonstrate this we make the following rescalings in order to form the governing equations in the narrow (of width $O(\delta)$) reaction layers

$$x^* = \delta w_l^*, \qquad 1 - x^* = \delta w_r^*, \tag{A.21}$$

so that w_l and w_r are the local coordinates within the left- and right-hand non-equilibrium layers, respectively. Under these rescalings the governing system for c_T^*, cf. relation (A.19b), becomes

$$\frac{\partial c_T^*}{\partial t^*} + \frac{1}{\delta}\frac{\partial \mathcal{F}_T^*}{\partial w_{l,r}^*} = 0 \tag{A.22}$$

which, on noting the smallness of δ, immediately asserts that

$$\mathcal{F}_T^* = \frac{j}{2F} + \mathcal{O}(\delta) \tag{A.23}$$

so one can thus write

$$\mathcal{F}_T^*\Big|_{x^*=0^+,1^-} = \frac{j}{2F} + \mathcal{O}(\delta) \tag{A.24}$$

throughout the reaction layers adjacent to the electrodes. This more rigorously justifies the application of the boundary conditions (5.10) to the governing system for the total Lithium flux in the bulk (5.9).

A3 Higher-Order Ion Clusters

Here we extend the analysis of Section 5.4 to demonstrate that in fact the same conclusions also hold when higher-order ion complexes are taken into account. Let us now consider third-order ion clusters with concentrations denoted as

c_{1+} — concentration of Li^+,

c_{1-} — concentration of N^-,

c_{20} — concentration of LiN,

c_{3+} — concentration of Li_2N^+,

c_{3-} — concentration of LiN_2^-.

Assuming that third-order ion clusters form from ion pairs, we can write the transformation reactions as follows

$$Q_1: \qquad Li^+ + N^- \rightleftharpoons LiN, \tag{A.25a}$$

$$Q_2: \qquad LiN + Li^+ \rightleftharpoons Li_2N^+, \tag{A.25b}$$

$$Q_3: \qquad LiN + N^- \rightleftharpoons LiN_2^-, \tag{A.25c}$$

where Q_1, Q_2 and Q_3 are the corresponding reaction rates. The conservation equations for the different species can then be written as

$$\frac{\partial c_{1+}}{\partial t} + \frac{\partial \mathcal{F}_{1+}}{\partial x} = -Q_1 - Q_2, \tag{A.26a}$$

$$\frac{\partial c_{1-}}{\partial t} + \frac{\partial \mathcal{F}_{1-}}{\partial x} = -Q_1 - Q_3, \tag{A.26b}$$

$$\frac{\partial c_{20}}{\partial t} + \frac{\partial \mathcal{F}_{20}}{\partial x} = Q_1 - Q_2 - Q_3, \tag{A.26c}$$

$$\frac{\partial c_{3+}}{\partial t} + \frac{\partial \mathcal{F}_{3+}}{\partial x} = Q_2, \tag{A.26d}$$

$$\frac{\partial c_{3-}}{\partial t} + \frac{\partial \mathcal{F}_{3-}}{\partial x} = Q_3, \tag{A.26e}$$

where $F_{(\cdot)}$ are the fluxes of the respective species. Reactions at the electrodes can now be written as

$$(I) \qquad Li \rightleftharpoons Li^+ + e^-, \tag{A.27a}$$

$$(II) \qquad Li + N^- \rightleftharpoons LiN + e^-, \tag{A.27b}$$

$$(III) \qquad Li + LiN \rightleftharpoons Li_2N^+ + e^-. \tag{A.27c}$$

At the anode the boundary conditions pertaining to the flux of each species can now be stated as, cf. (2.4a)–(5.3c),

$$\mathcal{F}_{1+}|_{x=0} = r_{(I)}, \tag{A.28a}$$

$$\mathcal{F}_{1-}|_{x=0} = -r_{(II)}, \tag{A.28b}$$

$$\mathcal{F}_{20}|_{x=0} = -r_{(III)} + r_{(II)}, \tag{A.28c}$$

$$\mathcal{F}_{3+}|_{x=0} = r_{(III)}, \tag{A.28d}$$

$$\mathcal{F}_{3-}|_{x=0} = r_{(I)}. \tag{A.28e}$$

$$\tag{A.28f}$$

Now let us define $\mathcal{F}_T$ as, cf. (5.8),

$$\mathcal{F}_T = \mathcal{F}_{1+} + \mathcal{F}_{1-} + 2\mathcal{F}_{20} + 3\mathcal{F}_{3+} + 3\mathcal{F}_{3-}, \tag{A.29}$$

which at the anode gives, cf. (5.10),

$$\mathcal{F}_T|_{x=0} = r_{(I)} + r_{(II)} + r_{(III)} = \frac{j}{F} \tag{A.30}$$

and similarly for the cathode we can write,

$$\mathcal{F}_T|_{x=L} = \frac{j}{F}. \tag{A.31}$$

If we also assume, cf. (5.8),

$$c_T = c_{1+} + c_{1-} + 2c_{20} + 3c_{3+} + 3c_{3-}, \tag{A.32}$$

then we can write, cf. (5.9),

$$\frac{\partial c_T}{\partial t} + \frac{\partial \mathcal{F}_T}{\partial x} = 0. \tag{A.33}$$

Thus, starting from equations (A.32) and (A.33) and following the approach laid down in Section 5.4, we can show that the transport equation for this extended system will again be formally equivalent to the Plank-Nernst equation (2.12). This analysis can be further extended in the same way to fourth- and higher-order ion clusters which will lead to the same conclusions.

Appendix B

Bayesian Inverse Modelling for Planck-Nernst Model with Dendrite Growth

B1 Values of Material Properties Reported in the Literature

- Y. Aihara et al., 2004 [1]

c $[mol/m^3]$	100	250	500	750
D $[m^2/s]$	3.5	3.1	2.5	2.1
t^+	0.33	0.35	0.34	0.34

- K. Hayamizy, 2012 [35]

D $[m^2/s]$	1.41

- M. Klett et al., 2013 [38]

D $[m^2/s]$	1.1
t^+	0.33

- K. Kondo et al., 2000 [39]

c $[mol/m^3]$	1	118	565	1100	1600	2070	2500	2910	3290
D $[m^2/s]$	4.9	4.2	2.7	1.4	0.74	0.37	0.17	0.090	0.061

- S. Krachkovskiy et al., 2013 [41]

c $[mol/m^3]$	200	800	1200	1800
D $[m^2/s]$	2.13	1.11	0.82	0.45
t^+	0.38	0.39	0.39	0.45

- A. Mehrotra et al., 2013 [49]

c $[mol/m^3]$	200	400	600	800
D $[m^2/s]$	7.11	6.54	3.21	2.14

t^+	0.41

- J. Newman et al., 2003 [56]

D $[mol/m^3]$	0.27
t^+	0.5

- M. Riley et al., 2002 [70]

c $[mol/m^3]$	100	250	500	750	1000	1500
t^+	0.3	0.22	0.18	0.12	0.10	0.01

- S. Stewart et al., 2008 [85]

D $[mol/m^3]$	0.77
t^+	0.4

- L. Valoen et al., 2005 [92]

c $[mol/m^3]$	0	1000	1750	2250
t $^+$	0.4	0.36	0.39	0.37

D $[m^2/s]$	0.87

- J. Zhao et al., 2008 [98]

c $[mol/m^3]$	250	500	750	1000	1500
D $[m^2/s]$	2.14	1.88	2.23	1.70	1.42
t^+	0.557	0.477	0.445	0.408	0.370

- S. Zugmann et al., 2011 [100]

D $[mol/m^3]$	3.37
t^+	0.24

B2 Determination of the Prior and Sampling the Likelihood Function

The prior $\mathbb{P}([D, t^+])$ in Figure 6.6 is constructed based on the literature data for the diffusivity and the transference numbers for the electrolyte considered in our study, which is summarized in Figures 6.2 and 6.3, and is also tabulated in Appendix B1. This is done using the function `kde2d` from the MASS package in R, where the bandwidth is suitably adjusted to obtain a prior with the desired "weakness". For problem P1 in our study the band widths used were $[1 \times 10^{-10}, 0.2]$ and $[4 \times 10^{-10}, 1]$ in increasing order of weakness. Whereas for P2, each discrete concentration value has a density function fitted with interpolated experimental data. The bandwidth used here was $[3 \times 10^{-10}, 0.8]$.

Sampling the likelihood function (4.6) is performed using the Metropolis-Hastings algorithm [16]. For brevity of notation, we will denote $m = [D, t^+]$. This algorithm is based on the Markov-Chain Monte-Carlo (MCMC) approach [32] employed to randomize m and at each step involves solution of the governing system (2.12) or (6.1) for modified (trial) material properties m^* followed by the evaluation of the error functional (4.3). At each step the algorithm moves in the probability space collecting samples from the probability distribution (4.5). A move in the probability space is accepted or rejected based on a sample acceptance ratio γ defined based on the posterior distribution (4.5). This approach is summarized as Algorithms 4 and 5, respectively, for problems involving constant and concentration-dependent material properties, and further technical details are provided in [78].

Algorithm 4 : Metropolis-Hastings algorithm to estimate the posterior probability distribution of constant material properties. The algorithm uses the function `normrnd(M,S)` which samples a normally distributed random variable with mean M and standard deviation S (a function with this name is available in MATLAB).

```
Input:
  literature data for $D$ and $t^+$, cf. Figure 6.2 and Appendix B1
  $\tilde{c}$ — experimental data,
  $M$ — numbers of samples generated
  $\bar{m}^{(0)}$ — initial guess sample
  $C$ — parameter controlling randomization
Output:
  an approximation of the posterior probability distribution $\mathbb{P}(m|\tilde{c})$

assimilate literature data to construct prior $\mathbb{P}(\bar{m})$.
construct initial sample $\bar{m}^{(0)}$
$k \leftarrow 1$
repeat
    create a new trial position $\bar{m}^* = \bar{m}^k +$ normrnd$(\bar{0}, C)$
    calculate acceptance ratio $\gamma = \frac{\mathbb{P}(\bar{m}^{(*)}|\tilde{c})}{\mathbb{P}(\bar{m}^{(k)}|\tilde{c})}$
    if $\gamma \geq$ rand(1):   $\bar{m}^{(k+1)} = \bar{m}^{(*)}$;   $k \leftarrow k + 1$,
    else:                      discard $m^{(*)}$
    $k = k + 1$
until $M + M/10$ samples are obtained for posterior distribution
discard the first $M/10$ samples
assimilate the remaining samples to obtain posterior probability distribution $\mathbb{P}(m|\tilde{c})$
```

Algorithm 5 : Metropolis-Hastings algorithm to estimate the posterior probability distribution of concentration-dependent material properties. The algorithm uses the function `normrnd(M,S)` which samples a normally distributed random variable with mean M and standard deviation S (a function with this name is available in MATLAB).

```
Input:
    literature data for $D(c)$ and $t^{+}(c)$, cf. Figure 6.3 and Appendix B1
    $\tilde{c}$ — experimental data,
    $M$ — numbers of samples generated
    $\bar{m}^{i}$ — initial sample in (chosen such that $\bar{m}^{i} \in \mathcal{X}$)
    $C$ — parameter controlling randomization
Output:
    an approximation of the posterior probability distribution $\mathbb{P}(m|\tilde{c})$
  assimilate literature data to construct prior $\mathbb{P}(\bar{m})$.
  $\bar{m}^{(0)} \leftarrow \bar{m}^{i}$
  transform $\bar{m}^{(0)}$ to $\bar{f}^{k}$ using cosine transformation
  $k \leftarrow 1$
  repeat
      create a new trial position $\bar{f}^{*} = \bar{f}^{k} \times$ normrnd$(\bar{0}, C)$
      using inverse cosine transform obtain $\bar{m}^{(*)}$
      calculate acceptance ratio $\gamma = \frac{\mathbb{P}(\bar{m}^{(*)}|\tilde{c})}{\mathbb{P}(\bar{m}^{(k)}|\tilde{c})}$
      if $\gamma \geq$ rand$(1)$:    $\bar{m}^{(k+1)}=\bar{m}^{(*)}$;    $k \leftarrow k+1$,
      else:                         discard $\bar{m}^{(*)}$
  until $20M + M/10$ samples are obtained for posterior distribution
  discard the first $M/10$ samples
  randomly select M samples from the remaining set and assimilate them to obtain posterior
  probability distribution $\mathbb{P}(m|\tilde{c})$
```

Bibliography

[1] Y. Aihara, T. Bando, H. Nakagawa, H. Yoshida, K. Hayamizu, E. Akiba, and W. S. Price. “Ion transport properties of six lithium salts dissolved in γ-butyrolactone studied by self-diffusion and ionic conductivity measurements”. In: *Journal of The Electrochemical Society* 151.1 (2004), A119–A122.

[2] R. Akolkar. “Mathematical model of the dendritic growth during lithium electrodeposition”. In: *Journal of Power Sources* 232 (2013), pp. 23–28.

[3] R. Akolkar. “Modeling dendrite growth during lithium electrodeposition at sub-ambient temperature”. In: *Journal of Power Sources* 246 (2014), pp. 84–89.

[4] D. Allard. *J.-P. Chilès, P. Delfiner: Geostatistics: Modeling Spatial Uncertainty*. 2013.

[5] D. Aurbach. “Review of selected electrodesolution interactions which determine the performance of Li and Li ion batteries”. In: *Journal of Power Sources* 89.2 (2000), pp. 206–218.

[6] D. Aurbach, M. D. Levi, E. Levi, H. Teller, B. Markovsky, G. Salitra, U. Heider, and L. Heider. “Common electroanalytical behavior of Li intercalation

processes into graphite and transition metal oxides". In: *Journal of The Electrochemical Society* 145.9 (1998), pp. 3024–3034.

[7] H. T. Banks, S. Hu, and W. C. Thompson. *Modeling and inverse problems in the presence of uncertainty.* Chapman and Hall/CRC, 2014.

[8] J. Barton and J. Bockris. "The electrolytic growth of dendrites from ionic solutions". In: *Proc. R. Soc. Lond. A* 268.1335 (1962), pp. 485–505.

[9] A. Beck and M. Teboulle. "Preliminary reference Earth modelA Fast Iterative Shrinkage-Thresholding Algorithm for Linear Inverse Problems". In: *SIAM Journal on Imaging Sciences* 2.1 (2009), pp. 183–202.

[10] P. Bergamaschi, R. Hein, M. Heimann, and P. J. Crutzen. "Inverse modeling of the global CO_2 cycle: 1. Inversion of CO mixing ratios". In: *Journal of Geophysical Research: Atmospheres* 105.D2 (2000), pp. 1909–1927.

[11] O. Borodin and G. D. Smith. "Quantum Chemistry and Molecular Dynamics Simulation Study of Dimethyl Carbonate: Ethylene Carbonate Electrolytes Doped with $LiPF_6$". In: *The Journal of Physical Chemistry B* 113.6 (2009), pp. 1763–1776.

[12] P Bousquet, P Peylin, P Ciais, M Ramonet, and P Monfray. "Inverse modeling of annual atmospheric CO_2 sources and sinks: 2. Sensitivity study". In: *Journal of Geophysical Research: Atmospheres* 104.D21 (1999), pp. 26179–26193.

[13] V. Bukshtynov and B. Protas. "Optimal Reconstruction of Material Properties in Complex Multiphysics Phenomena". In: *J. Comput. Phys.* 242 (2013), pp. 889–914.

[14] V. Bukshtynov, O. Volkov, and B. Protas. “On optimal reconstruction of constitutive relations”. In: *Physica D: Nonlinear Phenomena* 240.16 (2011), pp. 1228–1244.

[15] M. Chen and G. A. Rincon-Mora. “Accurate electrical battery model capable of predicting runtime and I-V performance”. In: *IEEE Transactions on Energy Conservation* 21.2 (2006), pp. 504–511.

[16] S. Chib and E. Greenberg. “Understanding the Metropolis-Hastings Algorithm”. In: *The American Statistician* 49.4 (1995), pp. 327–335.

[17] T. D. Claridge. *High-Resolution NMR Techniques in Organic Chemistry.* Vol. 27. Newnes, 2008.

[18] D. A. Cogswell. “Quantitative phase-field modeling of dendritic electrodeposition”. In: *Physical Review E* 92.1 (2015), p. 011301.

[19] H. Dai and T. A. Zawodzinski. “The Dependence of Lithium Transference Numbers on Temperature, Salt Concentration and Anion Type in Poly (Vinylidene Fluoride)-Hexafluoropropylene Copolymer-Based Gel Electrolytes”. In: *J. Electroanal. Chem.* 459.1 (1998), pp. 111–119.

[20] D. Deng, M. G. Kim, J. Y. Lee, and J. Cho. “Green energy storage materials: Nanostructured TiO_2 and Sn-based anodes for lithium-ion batteries”. In: *Energy and Environmental Science* 2 (2009), pp. 818–837.

[21] M. M. Doeff, P. Georèn, J. Qiao, J. Kerr, and L. De Jonghe. “Transport Properties of a High Molecular Weight Poly (propylene oxide)-$LiCF_3$ SO_3

System". In: *Journal of the Electrochemical Society* 146.6 (1999), pp. 2024–2028.

[22] R. Domingo and P. Marqui. "Review of Methods for Solving the EEG Inverse Problem". In: *International Journal of Bioelectromagnetism* 1.1 (1999), pp. 75–86.

[23] M. Doyle, T. F. Fuller, and J. Newman. "Modeling of Galvanostatic Charge and Discharge of the Lithium/Polymer/Insertion Cell". In: *The Journal of Electrochemical Society* 140.6 (1993), pp. 1526–1533.

[24] M. Doyle, T. F. Fuller, and J. Newman. "The importance of the lithium ion transference number in lithium/polymer cells". In: *Electrochimica Acta* 39.13 (1994), pp. 2073–2081.

[25] W. Dreyer, C. Guhlke, and R. Muller. "Overcoming the shortcomings of the Nernst–Planck model". In: *Physical Chemistry Chemical Physics* 15.19 (2013), pp. 7075–7086.

[26] A. Dukhin and S. Parlia. "Ion-Pair Conductivity Theory Fitting Measured Data for Various Alcohol-Toluene Mixtures across Entire Concentration Range". In: *J. Electrochem. Soc.* 162.4 (2015), H256–H263.

[27] A. M. Dziewonskia and D. L. Andersonb. "Preliminary reference Earth model". In: *Physics of the Earth and Planetary Interiors* 25.4 (1981), pp. 297–356.

[28] J. T. Edward. "Molecular volumes and the Stokes-Einstein equation". In: *Journal of Chemical Education* 47.4 (1970), pp. 261–268.

[29] D. R. Ely, A. Jana, and R. E. García. "Phase field kinetics of lithium electrodeposits". In: *Journal of Power Sources* 272 (2014), pp. 581–594.

[30] H. Engl, M. Hanke, and A. Neubauer. *Regularization of Inverse Problems.* Dordrecht: Kluver, 1996.

[31] M. Galiski, A. Lewandowski, and I. Stpniak. “Ionic liquids as electrolytes”. In: *Electrochimica Acta* 51.26 (2006), pp. 5567–5580.

[32] W. R. Gilks, S. Richardson, and D. Spiegelhalter. *Markov chain Monte Carlo in practice.* CRC press, 1995.

[33] M. Gouverneur, F. Schmidt, and M. Schonhoff. “Negative effective Li transference numbers in Li salt/ionic liquid mixtures: does Li drift in the ”Wrong” direction?” In: *Phys. Chem. Chem. Phys.* 20 (11 2018), pp. 7470–7478.

[34] H. Hafezi and J. Newman. “Verification and Analysis of Transference Number Measurements by the Galvanostatic Polarization Method”. In: *Journal of Electrochemical Society* 147.8 (2000), pp. 3036–3042.

[35] K. Hayamizu. “Temperature dependence of self-diffusion coefficients of ions and solvents in ethylene carbonate, propylene carbonate, and diethyl carbonate single solutions and ethylene carbonate+ diethyl carbonate binary solutions of $LiPF_6$ studied by NMR”. In: *Journal of Chemical & Engineering Data* 57.7 (2012), pp. 2012–2017.

[36] A. Jana and R. E. García. “Lithium dendrite growth mechanisms in liquid electrolytes”. In: *Nano Energy* 41 (2017), pp. 552–565.

[37] J. P. Kaipio, V. Kolehmainen, E. Somersalo, and M. Vauhkonen. “Statistical inversion and Monte Carlo sampling methods in electrical impedance tomography”. In: *Inverse Problems* 16.5 (2000), p. 1487.

[38] M. Klett, M. Giesecke, A. Nyman, F. Hallberg, R. W. Lindstrom, G. Lindbergh, and I. Furó. "Quantifying mass transport during polarization in a Li Ion battery electrolyte by in situ 7Li NMR imaging". In: *Journal of the American Chemical Society* 134.36 (2012), pp. 14654–14657.

[39] K. Kondo, M. Sano, A. Hiwara, T. Omi, M. Fujita, A. Kuwae, M. Iida, K. Mogi, and H. Yokoyama. "Conductivity and solvation of Li^+ ions of $LiPF_6$ in propylene carbonate solutions". In: *The Journal of Physical Chemistry B* 104.20 (2000), pp. 5040–5044.

[40] S. A. Krachkovskiy, J. D. Bazak, S. Fraser, I. C. Halalay, and G. R. Goward. "Determination of Mass Transfer Parameters and Ionic Association of $LiPF_6$: Organic Carbonates Solutions". In: *J. Electrochem. Soc.* 164.4 (2017), A912–A916.

[41] S. A. Krachkovskiy, A. D. Pauric, I. C. Halalay, and G. R. Goward. "Slice-selective NMR diffusion measurements: a robust and reliable tool for in situ characterization of ion-transport properties in lithium-ion battery electrolytes". In: *The Journal of Physical Chemistry Letters* 4.22 (2013), pp. 3940–3944.

[42] F. Lantelmea, H. Groulta, and N. Kumagaib. "Study of the concentration-dependent diffusion in lithium batteries". In: *Electrochimica Acta* 45.19 (2000), pp. 3171–3180.

[43] A. Lee, W. W. Cohen, and K. R. Koedinger. "A computational model of how learner errors arise from weak prior knowledge". In: *Proceedings of the Annual Conference of the Cognitive Science Society, Austin, TX*. 2009, pp. 1288–1293.

[44] B. Y. Liaw, G. Nagasubramanian, R. G. Jungst, and D. H. Doughty. “Modeling of lithium ion cellsA simple equivalent-circuit model approach”. In: *Solid state Ionics* 175.1-4 (2004), pp. 835–839.

[45] J. Liu and C. W. Monroe. “Solute-volume effects in electrolyte transport”. In: *Electrochimica Acta* 135 (2014), pp. 447–460.

[46] A. K. Louis. “Inverse Problems in Medicine”. In: *Proceedings of the Third German-Italian Symposium Applications of Mathematics in Industry and Technology*. 1989, pp. 227–287.

[47] D. Luenberger. *Optimization by Vector Space Methods*. John Wiley and Sons, 1969.

[48] Y. Marcus and G. Hefter. “Ion Pairing”. In: *Chemical Reviews* 106.11 (2006), pp. 4585–4621.

[49] A. Mehrotra and V. Srinivasan. “Transport Property measurements for $LiPF_6$ in EC: DEC (1: 1)”. In: *Meeting Abstracts*. 14. The Electrochemical Society. 2013, pp. 1152–1152.

[50] A. M. Michalak and P. K. Kitanidis. “A method for enforcing parameter nonnegativity in Bayesian inverse problems with an application to contaminant source identification”. In: *Water Resources Research* 39.2 (2003).

[51] C. Monroe and J. Newman. “Dendrite growth in lithium/polymer systems a propagation model for liquid electrolytes under galvanostatic conditions”. In: *Journal of The Electrochemical Society* 150.10 (2003), A1377–A1384.

[52] C. W. Monroe and C. Delacourt. “Continuum transport laws for locally non-neutral concentrated electrolytes”. In: *Electrochimica Acta* 114 (2013), pp. 649 –657.

[53] K. Mosegaard and M. Sambridge. “Monte Carlo analysis of inverse problems”. In: *Inverse problems* 18.3 (2002), R29.

[54] T. Nakamura and T. Chib. “Determining the equation of state of the expanding Universe: inverse problem in cosmology”. In: *Monthly Notices of the Royal Astronomical Society* 306.3 (1999), pp. 696–700.

[55] J. Newman and K. E Thomas-Alyea. *Electrochemical Systems*. John Wiley and Sons, 2004.

[56] J. Newman, K. E. Thomas, H. Hafezi, and D. R. Wheeler. “Modeling of lithium-ion batteries”. In: *Journal of Power Sources* 119 (2003), pp. 838–843.

[57] K. Nishikawa, T. Mori, T. Nishida, Y. Fukunaka, and M. Rosso. “Li dendrite growth and Li+ ionic mass transfer phenomenon”. In: *Journal of Electroanalytical Chemistry* 661.1 (2011), pp. 84–89.

[58] N. Nitta, F. Wu, J. T. Lee, and G. Yushin. “Li-ion battery materials: present and future”. In: *Materials today* 18.5 (2015), pp. 252–264.

[59] A. Nyman, M. Behm, and G. Lindbergh. “Electrochemical Characterisation and Modelling of the Mass Transport Phenomena in $\mathrm{LiPF_6EC{-}EMC}$ Electrolyte”. In: *Electrochim. Acta* 53.22 (2008), pp. 6356–6365.

[60] I. Olefir, S. Tzoumas, H. Yang, and V. Ntziachristos. “A Bayesian Approach to Eigenspectra Optoacoustic Tomography”. In: *IEEE Transactions on Medical Imaging* (2018).

[61] L. Onsager. “Initial Recombination of Ions”. In: *Phys. Rev.* 54 (8 1938), pp. 554–557.

[62] L. Onsager. “Deviations from Ohm’s Law in Weak Electrolytes”. In: *The Journal of Chemical Physics* 2.9 (1934), pp. 599–615.

[63] C. Ouyang, S. Shi, Z. Wang, X. Huang, and L. Chen. “First-principles study of Li ion diffusion in LiFePO 4”. In: *Physical Review B* 69.10 (2004), p. 104303.

[64] M. Park, X. Zhang, M. Chung, G. B. Less, and A. M. Sastry. “A review of conduction phenomena in Li-ion batteries”. In: *Journal of Power Sources* 195.24 (2010), pp. 7904–7929.

[65] A. D. Pasquier, I. Plitz, S. Menocal, and G. Amatucci. “A comparative study of Li-ion battery, supercapacitor and nonaqueous asymmetric hybrid devices for automotive applications”. In: *Journal of Power Sources* 115.1 (2003), pp. 171–178.

[66] W. S. Price. “Pulsed-field gradient nuclear magnetic resonance as a tool for studying translational diffusion: Part 1. Basic theory”. In: *Concepts in Magnetic Resonance* 9.5 (1997), pp. 229–336.

[67] B. Protas, T. R. Bewley, and G. Hagen. “A computational framework for the regularization of adjoint analysis in multiscale PDE systems”. In: *Journal of Computational Physics* 195.1 (2004), pp. 49–89.

[68] B. Protas, T. R. Bewley, and G. Hagen. “A Computational Framework for the Regularization of Adjoint Analysis in Multiscale PDE Systems”. In: *J. Comput. Phys.* 195.1 (2004), pp. 49–89.

[69] G. Richardson, J. M. Foster, A. K. Sethurajan, S. A. Krachkovskiy, I. C. Halalay, G. R. Goward, and B. Protas. “The effect of ionic aggregates on the transport of charged species in lithium electrolyte solutions”. In: *Journal of The Electrochemical Society* 165.9 (2018), H561–H567.

[70] M. Riley, P. S. Fedkiw, and S. A. Khan. “Transport properties of lithium hectorite-based composite electrolytes”. In: *Journal of the Electrochemical Society* 149.6 (2002), A667–A674.

[71] R. A. Robinson and R. H. Stokes. *Electrolyte solutions*. Courier Corporation, 2002.

[72] Y. Rubin, X. Chen, H. Murakami, and M. Hahn. “A Bayesian approach for inverse modeling, data assimilation, and conditional simulation of spatial random fields”. In: *Water Resources Research* 46.10 (2010).

[73] B. Saha, K. Goebel, S. Poll, and J. Christophersen. “Prognostics methods for battery health monitoring using a Bayesian framework”. In: *IEEE Transactions on instrumentation and measurement* 58.2 (2009), pp. 291–296.

[74] M. F. Samadi, S. M. Alavi, and M. Saif. “Online state and parameter estimation of the Li-ion battery in a Bayesian framework”. In: *American Control Conference (ACC), 2013*. IEEE. 2013, pp. 4693–4698.

[75] A. Seaman, T.-S. Dao, and J. McPhee. “A survey of mathematics-based equivalent-circuit and electrochemical battery models for hybrid and electric vehicle simulation”. In: *Journal of Power Sources* 256 (2014), pp. 410–423.

[76] A. K. Sethurajan. "Reconstruction of Concentration-Dependent Material Properties in Electrochemical Systems". MA thesis. McMaster University, 2014.

[77] A. K. Sethurajan, J. M. Foster, G. Richardson, D. Bazak, S. Krachkovskiy, G. Goward, and B. Protas. "Effect of Dendrite growth in the electrolyte mass transport: Insights from NMR measurements and Inverse Modelling". In: *Journal of Electrochemical Society - In Review* ().

[78] A. Sethurajan, S. Krachkovskiy, G. Goward, and B. Protas. "Bayesian Uncertainty Quantification in Inverse Modelling of Electrochemical Systems". In: *arXiv preprint arXiv:1806.00036* (2018).

[79] A. K. Sethurajan, S. A. Krachkovskiy, I. C. Halalay, G. R. Goward, and B. Protas. "Accurate characterization of ion transport properties in binary symmetric electrolytes using in situ NMR imaging and inverse modeling". In: *The Journal of Physical Chemistry B* 119.37 (2015), pp. 12238–12248.

[80] D. F. Shanno. "Conjugate gradient methods with inexact searches". In: *Mathematics of operations research* 3.3 (1978), pp. 244–256.

[81] R. Smith. *Uncertainty Quantification: Theory, Implementation, and Applications*. Computational Science and Engineering. SIAM, 2013. ISBN: 9781611973228. URL: `https://books.google.ca/books?id=Tc1GAgAAQBAJ`.

[82] M. Šorel and M. Bartoš. "Fast Bayesian JPEG decompression and denoising with tight frame priors". In: *IEEE Transactions on Image Processing* 26.1 (2017), pp. 490–501.

[83] V. Srinivasan and J. Newman. “Design and Optimization of a Natural Graphite/Iron Phosphate Lithium-Ion Cell”. In: *Journal of the Electrochemical Society* 151.10 (2004), A1530–A1538.

[84] J. Steiger, D. Kramer, and R. Mönig. “Microscopic observations of the formation, growth and shrinkage of lithium moss during electrodeposition and dissolution”. In: *Electrochimica Acta* 136 (2014), pp. 529–536.

[85] S. Stewart and J. Newman. “Measuring the salt activity coefficient in lithium-battery electrolytes”. In: *Journal of The Electrochemical Society* 155.6 (2008), A458–A463.

[86] A. M. Stuart. “Inverse problems: A Bayesian perspective”. In: *Acta Numerica* 19 (2010), pp. 451–559. DOI: `10.1017/S0962492910000061`.

[87] A. M. Stuart. “Inverse problems: a Bayesian perspective”. In: *Acta Numerica* 19 (2010), pp. 451–559.

[88] V. R. Subramanian, V. Boovaragavan, and V. D. Diwakar. “Toward Real-Time Simulation of Physics Based Lithium-Ion Battery Models”. In: *Electrochemical and Solid-State Letters* 10.11 (2007), pp. 225–260.

[89] A. Tarantola. *Inverse Problem Theory and Methods for Model Parameter Estimation.* SIAM, 2005.

[90] C. M. Tenney and R. T. Cygan. “Analysis of Molecular Clusters in Simulations of Lithium-Ion Battery Electrolytes”. In: *The Journal of Physical Chemistry C* 117.47 (2013), pp. 24673–24684.

[91] L. Tenorio. *An Introduction to Data Analysis and Uncertainty Quantification for Inverse Problems*. Philadelphia, PA: Society for Industrial and Applied Mathematics, 2017.

[92] L. O. Valoen and J. N. Reimers. "Transport properties of $LiPF_6$-based Li-ion battery electrolytes". In: *Journal of The Electrochemical Society* 152.5 (2005), A882–A891.

[93] J. Vatamanu, O. Borodin, and G. D. Smith. "Molecular Dynamics Simulation Studies of the Structure of a Mixed Carbonate $LiPF_6$ Electrolyte Near Graphite Surface as a Function of Electrode Potential". In: *The Journal of Physical Chemistry C* 116.1 (2011), pp. 1114–1121.

[94] C. Wang and V. Srinivasan. "Computational battery dynamics (CBD) electrochemical /thermal coupled modeling and multi-scale modeling". In: *Journal of Power Sources* 110.2 (2002), pp. 364–376.

[95] X. Wang, W. Zeng, L. Hong, W. Xu, H. Yang, F. Wang, H. Duan, M. Tang, and H. Jiang. "Stress-driven lithium dendrite growth mechanism and dendrite mitigation by electroplating on soft substrates". In: *Nature Energy* 3.3 (2018), pp. 227–235.

[96] C. J. Wen, B. A. Boukamp, R. A. Huggins, and W. Weppner. "Thermodynamic and Mass Transport Properties of LiAl". In: *Journal of The Electrochemical Society* 126.12 (1979), pp. 2258–2266.

[97] J. Zhang, W. Xu, and W. A. Henderson. *Lithium metal anodes and rechargeable lithium metal batteries*. Springer International Publishing Switzerland, 2017.

[98] J. Zhao, L. Wang, X. He, C. Wan, and C. Jiang. “Determination of lithium-ion transference numbers in $LiPF_6$–PC solutions based on electrochemical polarization and NMR measurements”. In: *Journal of The Electrochemical Society* 155.4 (2008), A292–A296.

[99] S. Zugmann, M. Fleischmann, M. Amereller, R. M. Gschwind, H. D. Wiemhfer, and H. J. Gores. “Measurement of Transference Numbers for Lithium Ion Electrolytes via Four Different Methods, a Comparative Study”. In: *Electrochim. Acta* 56.11 (2011), pp. 3926–3933.

[100] S. Zugmann, M. Fleischmann, M. Amereller, R. M. Gschwind, M. Winter, and H. J. Gores. “Salt diffusion coefficients, concentration dependence of cell potentials, and transference numbers of lithium difluoromono (oxalato) borate-based solutions”. In: *Journal of Chemical & Engineering Data* 56.12 (2011), pp. 4786–4789.